SEIRAS of Functionalised Graphene Nanomaterials

A thesis presented in partial fulfilment of the
requirements for the degree of

Master of Science

In

Nanoscience

MASSEY
UNIVERSITY
TE KUNENGA KI PŪREHUROA
UNIVERSITY OF NEW ZEALAND

At Massey University, Manawatū, New Zealand.

Ewan Fisher

2017

Abstract

Graphene exhibits many excellent properties, but many next-generation devices require post chemical treatment to introduce structural confirmations, defects or a particular impurity to obtain functionality. The understanding of these defects and the manifestation of desirable properties using chemical modification is a fundamental problem with low defect graphene as the small number of functional groups provides insufficient signal intensity for many characterisation techniques. Metallic nanoparticles are at the centre of plasmonics for enhancing optical signals. This work is a unique undertaking for the examination of novel Steglich esterification chemistry that is performable on graphene as well as providing insight into the native edge structure of as-produced graphene flakes using surface enhanced infrared reflection absorption spectroscopy (SEIRAS) to characterise covalently functionalised graphene materials.

Two methods of producing graphene flakes that are relatively low or high in defects have been developed to contrast the effect that inherent defects have on the macroscopic physical and spectroscopic properties. Ultraviolet-visible spectroscopy in conjunction with Raman, electron and atomic force microscopy was used to elucidate the origins and density of defects to draw conclusions on how graphene’s macroscopic properties manifest from atomic level defects.

Discussions of infrared vibrational spectroscopy are carried out before an extension to SEIRAS where the use of near-field plasmon and phonon modes are attributed to observed optical enhancements. The experimental preparation is focused towards understanding the role nanoparticles play in SEIRAS of graphene and is discussed such that other graphene researchers can recreate SEIRAS for their graphene research. TEM is used to characterise the variety of nanoparticle shapes and geometries as well as provide topological insights on nanoparticles adsorbed to flakes of graphene.

SEIRAS probes the defects native to graphene which confirms the presence of oxygen functionality. Steglich esterification reactions were utilised to successfully prepare a range of graphene materials with novel covalently bound functional groups as confirmed by SEIRAS. Covalent chemistry was extended to introduce a redox-active ferrocene derivative where SEIRAS was used to observe in real-time, the effect of interconversion of ferrocene to the ferrocenium cation.

The foundations for the development of graphene-based solid state solar cells was the final focus of this work. Development and production of a potential photo-active layer was explored with Cl-BODIPY as the basis chromophore. Production of a flexible, electrically conductive substrate from graphene flakes was carried out, and tunnelling electron microscopy (TEM) was used to characterise topological and morphological surface features. The focus here was on covalent and physical absorption to graphene flakes. SEIRAS was used to confirm nucleophilic substitution (covalent) modification while STEM was used to confirm the uniformity of BODIPY on the substrate and chlorine atomic mapping to confirm physisorption.

Acknowledgements

I would like to thank my supervisor Assoc. Prof. Mark Waterland. His mentorship during my masters studies at Massey University was paramount in both developing me as a nanoscientist and the incredible experience during these two years.

I would also like to thank members of our research group, especially Sam Brooke, Jason Carr, Ashley Way and Haidee Dykstra, with whom discussions surrounding many of the same challenges lead to innovative solutions to my puzzling problems.

The frequent discussions and assistance from Mr Graham Freeman kept me on the right foot where his chemistry experiences often provided me with new ways to solve problems; thank you.

Finally, the Manawatu Microscopy and Imaging centre for providing access to their facilities. In particular Jordan Taylor for obtaining TEM images and Niki Minards for STEM images.

Abbreviations and Symbols

AFM	Atomic force microscopy
ATR	Attenuated total reflectance
ATR-FTIR	Attenuated total reflectance Fourier transform infrared
CB	Conduction band
CVD	Chemical vapour deposition
DCC	N,N'-Dicyclohexylcarbodiimide
DOS	Density of states
E_D	Dirac point energy
ED	Ethylene diamine
EDC	1-Ethyl-3-(3-dimethylaminopropyl)carbodiimide
E_F	Fermi level energy
E_g	Band gap energy
E_{local}	Local electric field intensity
EM	Electromagnetic
EPC	Electron-phonon coupling
eV	Electron volts
GO	Graphene oxide
HOPG	Highly orientated pyrolytic graphite
LB	Langmuir-Blodgett
NIR	Near infrared
PV	Photovoltaic
RAIRS	Reflection absorption infrared spectroscopy

SEIRAS	Surface enhanced infrared reflection absorption spectroscopy
SEIRASEC	Surface enhanced infrared reflection absorption spectroelectrochemistry
SEM	Scanning electron microscopy
SERS	Surface enhanced Raman spectroscopy
SP	Surface plasmon
SPR	Surface plasmon resonance
SSSC	Solid-state solar cell
THF	Tetrahydrofuran
UV-vis spec.	Ultraviolet-visible spectroscopy
VB	Valance band

Glossary of Graphene Materials

GN-Flake	Graphene flakes produced by graphite nanotomy at micron increments
GN-Flake-BO	GN-Flakes functionalised with Cl-BODIPY
GN-Flake-ED	GN-Flakes functionalized with Ethylenediamine
GN-Flake-NA	GN-Flakes functionalised with 4-Nitroaniline
GN-Flake-NB	GN-Flakes functionalised with 4-Nitrobenzoic acid
GN-Flake-SA	GN-Flakes functionalized with Sulfanilic acid
xFlakes	Flakes of graphene produced by electrochemical exfoliation
xFlake-BO	xFlakes functionalised with Cl-BODIPY
xFlake-ED	xFlakes functionalised with Ethylenediamine
xFlake-ED-Fe	xFlakes functionalised with Ethylenediamine then ferrocene
xFlake-NA	xFlakes functionalised with 4-Nitroaniline
xFlake-$NaBH_4$	xFlakes reduced over $NaBH_4$
xFlake-NB	xFlakes functionalised with 4-Nitrobenzoic acid
xFlake-paper	Graphene substrate produced by compacting xFlakes
xFlake-SA	xFlakes functionalised with Sulfanilic acid
xFlakes-$LiAlH_4$	xFlakes reduced over $LiAlH_4$
xFlakes-$NaBH_4$	xFlakes reduced over $NaBH_4$

Table of Contents

Table of Contents

Chapter one – Graphene: Atoms to Material

Background

Graphene was identified as a potential material more than sixty years ago by early graphite chemists, but it was just over a decade ago that Manchester University scientists isolated a single sheet of graphene and provided the first experimental proof of its remarkable properties. Despite considerable interest in this 2D carbon monolayer, the evolution of graphene from the laboratory to applications is slow. The reason is the diminishment of the properties during scale-up and the requirement of chemical methods to induce functionality before incorporation into devices. Despite graphene's potential for strong, lightweight energy devices, the transition from laboratory to real world use remains a challenge. For example, photonic applications such as solar cells require electrically conductive graphene which in turn needs a low density of structural defects, or is in other words "pristine". This chapter first presents a brief background to renewable energy to highlight the important role that renewable energy materials play in the future of energy demand. Following the background is the development of the necessary physical, chemical and optical properties of graphene relevant to experimental results presented in chapters two to five. Atomic scale crystallinity is used to described graphene's properties before discussing the literature on how impurities, defects and structural confirmations cause deviations from crystallinity allowing long range effects to manifest a particular property. Deviating from a perfect crystal is the overall theme of this thesis – defects are necessary for introducing useful device functionality.

1.0 Challenges and Future Trends in Graphene Renewable Energy

The need for renewable energy sources is becoming increasingly apparent as non-renewable sources such as oil, natural gas, and coal are depleted, with estimates of lasting 35, 37 and 107 years respectively[1]. Global warming and other negative environmental impacts of non-renewable energy sources are putting nations under pressure to find and use renewable alternatives. Renewable sources of energy, consisting of geothermal, wind and solar[2] provided only 7% of the world's energy requirements in 2013. Renewable energy sources increased to 7.3% in 2014, a rate of growth which is too slow to avoid future environmental damage. To make a significant difference the average household needs to invest into renewable sources of energy. While most families cannot afford windmills or access geothermal vents, solar power is a viable alternative as it only requires small panels, easily hidden on rooftops. Photovoltaic (PV) materials are semiconductors which convert light into electricity using the photoelectric effect. This effect allows certain materials to absorb photons and release electrons, generating free electrons and producing an electrical current. We live in the age of silicon for its predominance in transistors, but more importantly, solar cells. Silicon is currently the most widely used semiconductor material in solar technology, comprising of over 80% of the market[3.] Silicon's popularity is due to its ease of processing, owing to advancements in the electronics industry, not necessarily because it is the best material to use. Silicon requires over 99.999% purity to be semiconducting, which is expensive to obtain, requiring massive energy input. Silicon solar cells need ten years of operation to offset the energy cost of production. The significant upfront investment of silicon solar cells is financially unviable for many people, hindering the growth of solar cell technology. Converting only 1% of the sunlight striking Earth's surface to electrical energy at an efficiency of 10%, we would get 105 TW of power[4]. The power generation is four times the Earth's predicted total energy needs in 2050. Making solar collectors financially accessible to the general population of both developed and third world countries is a key factor in driving the transition to renewable energy sources. Replacing silicon with a more efficient, cheaper to manufacture solar collector is thus essential.

Subsequent sections will discuss the theory behind this problem and the approach to resolving it. Graphene as a material distinct from graphite was defined in the 1960's.[105] Graphene is a hexagonal lattice of sp^2-hybridised carbon atoms, an extended two-dimensional lattice of 'benzenoids' void of all elements except carbon. These benzenoids are the four types of aromatic sextets described by clars rule for extended aromatics.[105] The sextets are classified as aromatic, empty, migrating or as having localised double bonds. These Clar structures are important for predicting chemical reactivity at graphene's edges. Graphene materials studied in this thesis are much larger laterally than the depiction in figure 1 which comprises only a few hundred aromatic rings. Typical flakes of graphene are on the order of a billion rings in each lateral dimension – that is hundreds of trillions of rings in total, but still only a single

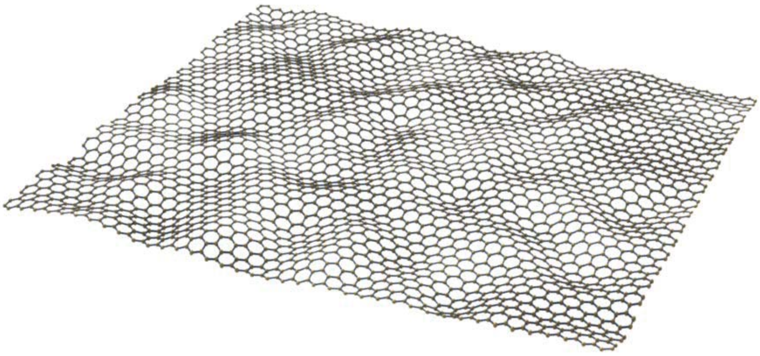

Figure 1: Cartoon picture of a wavey sheet of graphene. ©James Hedberg (2015)[5].

atom thick. Graphene absorbs 2.3% of all incident light in the UV-Mid-IR region (photon quanta 0.05 – 6.20 eV), and is, therefore, a universal absorber[6]. It has electrical conductivity ten times that of copper (≈ 200,000 $cm^2V^{-1}\ s^{-1}$) and a theoretical specific surface area that is fifteen times that of TiO_2 nanoparticles (≈ 2600 m^2g^{-1})[7,8]. These exceptional properties, however, are theoretical upper limits meaning in practice, are difficult to achieve and exclusive to pristine graphene. The precursor to graphene is graphite, which is naturally abundant, meaning production and processing of the raw materials are economical. With these excellent properties, it appears that graphene will be the key component in next generation photonic devices. It does, however, have problems that need resolving. The significant barriers to using graphene in photovoltaics are defect free sample preparation (required for high electrical conductivity) and that it is a zero band gap semiconductor which prevents charge separation, a key requirement for photovoltaic materials.

1.1 Mechanical Properties

This section on the physical properties of graphene forms the basis for understanding the optical and electronic properties described in the proceeding chapters. Distinctive properties of solids arise due to the collective behaviour of an extended array of chemical bonds. The new feature of chemical bonding, in the context of graphene (at least for a chemist), is the extended array of bonds in the solid state. To describe this array the concepts of local symmetry and repetitive, long-range order are required so that together, a unit cell and crystal lattice can be defined. Placing symmetry elements at the lattice points forms the idea of a "perfect crystal". The edges of a perfect graphene crystal is an infinitely repeating zig-zag or armchair conformation (figure 2 below). These edges are rarely in practice as homogeneous over extended lengths, but alternate between short segments of each.

These perfect crystals form the fundamental starting point for describing the properties of graphene. It is, however, the passivation with functional groups or introduction of a specific defect at these edges that ultimately determines or causes deviations from these properties.

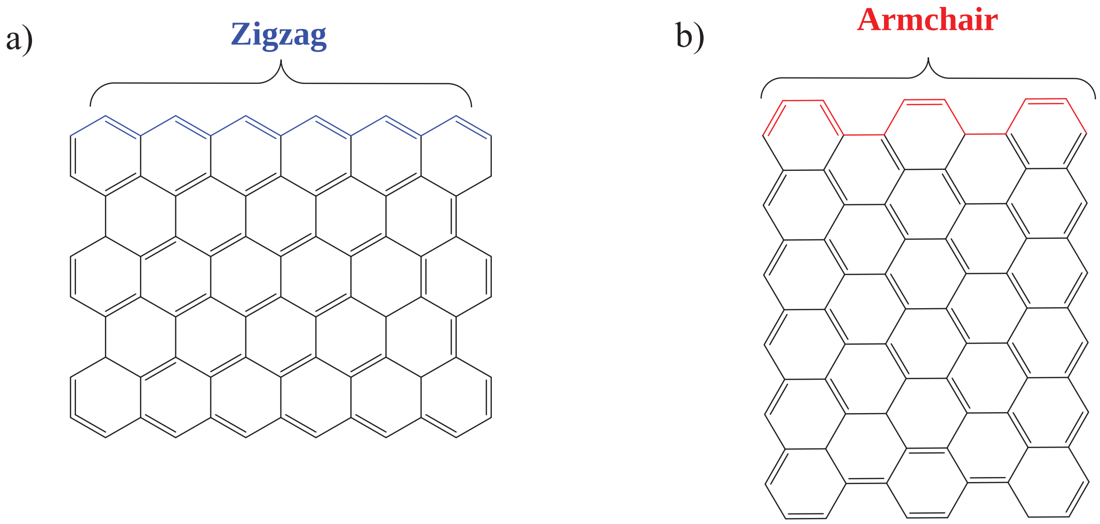

Figure 2: Definition of graphene with chirality a) Zigzag and (b) armchair.

Graphene is described here as “quasi-crystalline” in that as lateral dimensions approach microns in diameter, the sheet requires a substrate to maintain structural integrity. Graphene’s crystallinity and deviations from this crystallinity manifest as vastly different properties in the resulting materials. An understanding of these defects is included here, as these defects are essential to chemically modifying graphene and as a result, could manifest properties useful for applications. Common displacement defects in graphene are Stone-Wales and Frenkel defects. Displacements affect short-range crystallinity and may manifest as deviations from the bulk regarding reactivity by the creation of edges or grain boundaries (figure 2 above). Displacement defects, where atoms are removed or added from lattice sites, can result in long-range effects when present in sufficient density. Defected edge structures, where alternating edge type, as well as a ring structure, can occur, *e.g.* 7-5-7 rings, formed by rotating a C-C bond 90 degrees, are Stone-Thrower-Wales defects or if stabilised by dopants, are Thrower-Stone defects[9, 10]. The accumulation of Thrower-Stone defects in the short-range affects the long-range crystallinity and macroscopic properties e.g. mechanical twisting; curvature causes deviations in electrical conductivity[11]. Defects consequently change elasticity resulting in bending and weaving of graphene flakes like a piece of silk cloth under its gravity[103, 104]. The unsaturation of the P_z orbitals around defect sites and breaking of π conjugation at edges increases the edge electron’s energies. These defects increase chemical reactivity due to the lower resonance stability, and high strain of these structures. This discussion is of particular interest in chapter two of this work for describing grain boundaries, dislocations, flexing, waviness and bending of graphene, which is typical for a two-dimensional material but rarely observed in three-dimensional crystals. A detailed discussion of defects is provided in the relevant sections of chapter two but is mentioned here to highlight the interconnection between atomic scale elements and the macroscopic properties of graphene materials.

1.2 Dispersion Relation to Optical Properties

Semiconductors are materials with an energy difference between the conduction and valence bands, (CB and VB respectively) or 'band-gap energy' of less than 3 eV. The Dirac point is the point at which the conduction band (CB) and valence band (VB) touch in reciprocal space at a degenerate energy. Graphene's dispersion relation, colloquially known as a 'Dirac cone', originates from a linear energy dependence on crystal momentum (k) while having a parabolic dependence at energies well above the Dirac point.

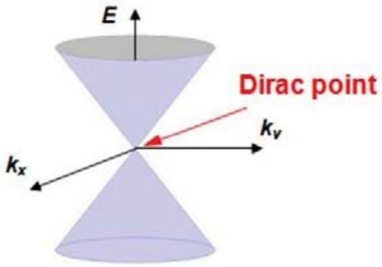

Figure 3: Sketch of the electronic structure of graphene, cone-shape linear electronic dispersion and density of states. ©Leibniz-Institut für innovative Mikroelektronik (2015)[12].

Figure 3 shows that the bands meet at the Dirac point, meaning graphene has no band gap. Zero band gap materials absorb photons at all frequencies. When an electron is excited into the conduction band by absorption of a photon, the charge carriers generated have very short lifetimes. The charge carriers will recombine, producing heat before they can be separated and removed as required for applications. The introduction of a band gap solves this problem by providing an electrostatic barrier to recombination allowing the use in many applications. The modification of graphene's band structure through covalent and non-covalent chemical procedures is the framework for chapter five.

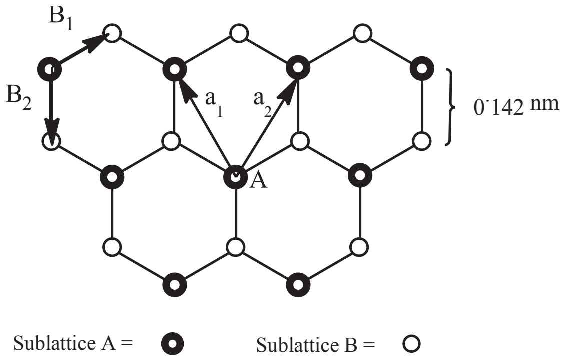

Figure 4: Honeycomb lattice. a_1 and a_2 are basis vectors that produce the A triangular sublattice. B_1 and B_2 connect the A and B sublattice carbon atoms separated by 0.142 nm[13].

An ordered array of identical repeating units is a crystal. In graphene, the repeating unit is the hexagonal benzene's A and B sublattice atoms (figure 4). The tight binding model describes graphene's electronic structure. Only a brief discussion is carried out below as a comprehensive description can be found in the literature[14]. The tight binding model and Huckel approximation used in molecular orbital theory are very similar. The real lattice unit cell has two atoms, A and B that are related by the vectors B1 and B2 as shown in figure 3. Therefore, the honeycomb lattice is two separate triangular sublattices, comprising of either atom A or B where the lattice points of each sublattice are related by basis vectors a_1 and a_2[14]. The nearest neighbour to atom A (black) is atom B (white), which is on the opposite sublattice. These points are related through inversion symmetry, resulting in the Dirac points in reciprocal space being degenerate. Perturbations in the lattice such as imbalanced electron density cause breaking of inversion symmetry meaning that graphene's band gap increases[15]. Typically, disturbances result from lattice defects such as vacancies, dislocations or edge modifications. Research groups have added defects by covalent functionalisation or doping[16-

[18], and while these materials have band gaps suitable for photonic applications, the production methods are harsh and ultimately lead to failure in applications. Opening graphene's bandgap via these methods would produce material unsuitable for photonic applications. Impurities and defects will diminish graphene's properties *e.g.* impurities interrupting the extended π system reduces electrical conductivity. Additionally, the material would not be photostable, which is essential for long device lifetimes. Opening graphene's bandgap by breaking inversion symmetry without degrading properties is crucial for use in applications *e.g.* photonics. Breaking symmetry is possible with many methods as shown in experimental and computational studies. For example, introducing an asymmetrical mechanical strain deforms graphene. The strain produces a potential difference in bilayer graphene, breaking the translational symmetry, and opening a tunable band gap of 0.4 eV[19-21]. Other non-destructive techniques are the application of parallel magnetic or electric fields[13, 22-24]. Charged particles respond to applied electric or magnetic fields therefore an applied field affects charge carrier drift velocity, and as a result, the Dirac cone is tilted, breaking degeneracy. These methods of opening band gaps have the potential to produce extremely robust materials but are currently not practical for producing bulk amounts of material for applications. Chapter four explores the covalent modification of defects native to two production methods.

1.3 Fano's Theory

Fano resonances are asymmetric features in absorption, scattering or transport spectra[30]. They result from an interaction between discrete and a continuum of states. This condition where Fano's theory applies is shown schematically in figure 5 below.

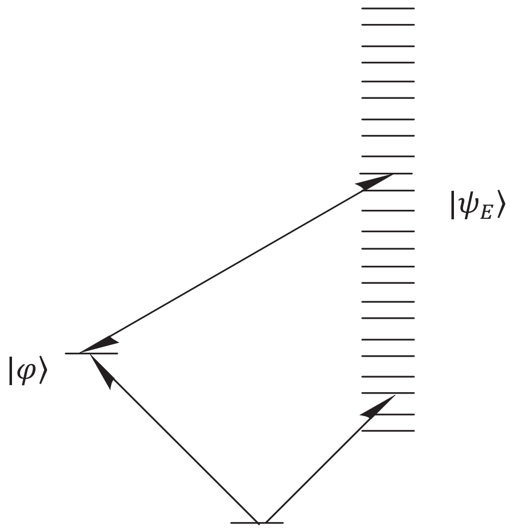

Figure 5: Energy diagram for interference effects between excitations from a ground state to a single discrete level $|\varphi\rangle$, coupled to a continuum of states $|\psi_E\rangle$.

As an example, we will consider coupling between a discrete state, $|\varphi\rangle$, and a continuum of states, $|\psi_E\rangle$. For this example, graphene is used where a correlated electron-hole (exciton) constitutes a discrete state while the electronic states of the band structure constitute the continuum of states. Another relevant case for graphene are infrared active optical-phonons coupled to these electronic states. In the first case, coupling is due to electron correlation while the phonon interaction is determined by electron-phonon coupling[29]. Coupling of discrete to continuum states generates mixed (hybrid) states, $|\psi_E\rangle$, that are linear combinations of $|\psi\rangle$ and $|\psi_E\rangle$. The transition to a single discrete state of transition probability amplitude ⟨φ | μ | i⟩, the lineshape is lorentzian, which is understood to arise from the exponential decay of the excited discrete state. Fano theory describes the effect that coupling of the discrete state to a continuum of states has on the lineshape. A better understanding of the effect of the continuum is obtained by considering the contributions of the discrete and continuum states to the transition probability from $|i\rangle$ to $|\psi_E\rangle$. Fano's theory introduces a modified discrete state, $|\varphi\rangle$, which takes into account the presence of the continuum states. Then, for a transition driven by electric dipole coupling with operator μ:

$$\langle\psi_E|\mu|i\rangle = \frac{1}{\pi V_E}\langle\varphi|\mu|i\rangle \sin\Delta - \langle\psi_E|\mu|i\rangle \cos\Delta \text{ where}$$

$$\Delta = -\tan^{-1}\frac{\pi|V_E|^2}{E - E_\varphi - F(E)}$$

Note that Δ varies sharply as E → E_φ + F(E) and that sin Δ is an even function of Δ, whereas cos Δ is an odd function of Δ. F(E), in turn, is an integral over the couplings between the discrete and continuum states:

$$\mathrm{F(E)} = P\int dE'\frac{V(E')}{E-E'}$$

The energy dependent transition dipole, V(E'), is used for optical transitions. If the absorption spectrum is assumed to be a continuous distribution of delta functions, then the absorption cross section at each energy, σ(E'), is used to determine V(E')[115]. The expression above shows that the contributions to the discrete state and continuum state to $\langle\varphi|\mu|i\rangle$ interfere with opposite phase on the two sides of the resonance. These contributions of the discrete state and continuum states to the total transition probability interfere with opposite phase on the two sides of the resonance meaning the transition probability will vanish on one side of the resonance. The results of Fano theory[30] is the unitless Fano parameter, q, which describes the relative dipole strength of the renormalized transition, by using the ratio of the transition probability from the ground state, $|i\rangle$, into the continuum states, and the transition probability into the discrete state modified by the presence of the continuum, $|\varphi\rangle$. For a transition driven by the electric dipole coupling (with operator μ),

$$q(E) = \frac{\langle\varphi|\mu|i\rangle}{\pi\, V_E\, \langle\psi_E|\mu|i\rangle}$$

The absorption line shape is then[114]

$$\sigma(E) \propto \left(1 + \frac{q^2-1}{1+s^2} + \frac{2qs}{1+s^2}\right) = \frac{(s+q)^2}{1+s^2}$$

$$where\ s = \frac{E-E_\psi}{\frac{\gamma}{2}}$$

and γ is a damping parameter that determines the width of the lorentzian lineshape that would occur in the absence of coupling.

A qualitative model of the absorption line shape is plotted in figure 6 below for some q values to highlight how Fano's theory could describe asymmetric band shapes as utilised in literature for describing a variety of graphene systems[25-29]. The graphene materials produced in this work exhibit asymmetric band shapes. For example, UV-vis absorption band asymmetries presented in chapter two are possibly a result of coupling between discrete electronic states and a continuum of longitudinal acoustic phonon modes. The purpose here is to briefly discuss the qualitative result from Fano's theory that is relevant to experimental data presented in later chapters.

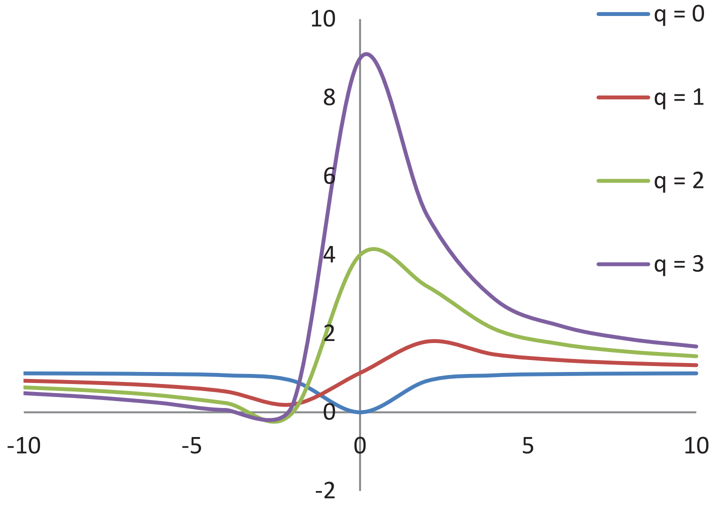

Figure 6: Fano line shapes for a range of q values.

Figure 6 plots the ratio of transition probabilities of a modified discrete state to an unperturbed band continuum over a range of q values. Such lineshapes are thus attributed to Fano interference. Depending on the value of q, the absorption can be a resonance where q

$>> 1$ *e.g.* continuum dominates, $q \approx 1$ (dispersive) where contributions from the continuum and discrete state are equal or $q << 1$ and discrete states dominate the lineshape. The sharp variations as q increases indicate how interference with an oppositely phased resonance, caused by the changed transition probability results in the disappearance of the phases on the positive component of the asymmetry.

1.4 Thesis Outline

The chapters are summarised.

Chapter one

Background and theoretical basis for this work. A brief background discussion on the energy crisis and theoretical discussions are used to highlight both the importance of graphene itself and why chemical modifications are required for real-world applications. Simple theoretical concepts are introduced such as in practice, even the highest quality crystals of graphene cannot have long range order, so defects will always be present. These atomic-scale defects, intrinsic to all graphene, manifest as long range effects *e.g.* optical, physical and chemical properties are affected in profound ways. Graphene's dispersion relation is introduced for the two-dimensional hexagonal lattice before the extension to include many-body effects with Fano's theory *e.g.* electron-hole pair interactions. This theory is utilised to explain the asymmetric band shapes observed in later chapters but is included here because it appears in multiple chapters. A comprehensive review and discussion of the graphene literature are beyond the scope of this thesis, so where appropriate, the interested reader is referred to references where detailed discussions of the topic are described by other authors.

Chapter two

Graphene production methodologies. Theoretical and experimental details of two methods of producing graphene flakes are described. Namely a high-quality, low-quantity graphite "nanotomy" production method and a low-quality, high-quantity liquid-phase electrochemical exfoliation are described. This first experimental chapter focuses on novel physical and spectroscopic characterisation of the flakes produced by these two methods. Fano's asymmetric band shape makes its first appearance in UV-vis absorption spectra and is accompanied by an interesting discussion on possible underlying mechanisms. The properties of graphene are, on the most fundamental level, different due to atomic scale defects which result in the manifestation of vastly different macroscopic optical and physical properties. The accumulation of experimental data on these materials is presented and organised to contrast and provide insight into how macroscopic properties manifest as a result of defects intrinsic to graphene produced by each method. Applications being the end goal of this work, contrasting the methods helps answer the question: "which graphene preparation method is best suited for applications?".

Chapter three

Development of surface enhanced infrared reflection absorption spectroscopy (SEIRAS). A powerful spectroscopic mid-IR enhancement tool for the characterisation of functionalised graphene materials is described. SEIRAS solves a common problem encountered in the mid-IR analysis of functionalised graphene; detection sensitivity. As functionalisation of graphene is an underlying theme of this thesis, SEIRAS is invaluable for characterising graphene materials produced in proceeding chapters. This chapter starts with a theoretical approach to provide an understanding of underlying mechanisms. One is possibility unique to graphene samples – plasmon-phonon hybridization. The experimental methods and procedures are then described to illustrate factors that affect reproducibility. The experimental component of this chapter is designed to be as easily reproducible by other research so the interested researcher can apply SEIRAS to their work.

Chapter Four

Characterisation of functionalised graphene by SEIRAS. The technique developed in the previous chapter is utilised to pinpoint the functionality of as-produced graphene before their use as chemical handles to introduce novel functionality. SEIRAS confirms the feasibility of graphene's functionalisation with novel organic moieties via Steglich esterification. The confirmation leads to the development of a spectroelectrochemical device that incorporates electrochemistry into SEIRAS. This device allows the probing, in real time, the interconversion of redox states in ferrocene-functionalized graphene.

Chapter five

Functionalisation of graphene with Cl-BODIPY. Covalent and physical functionalisation of graphene flakes and a graphene substrate respectively with the chromophoric dipyrrin compound Cl-BODIPY is carried out to lay the groundwork for the development of a graphene-based solid state solar cell. SEIRAS is used to indicate successful covalent functionalisation while elemental mapping with scanning tunnelling electron microscopy confirms homogeneous physisorption.

Chapter six

Conclusions. Summary of the works presented in this thesis and discussion of future complementary experiments.

Chapter Two – Micro and Spectroscopic Characterisation of Graphene Flakes

2.0 Introduction

The development of methods to prepare large quantities of graphene exhibiting the excellent properties it is known for is a fundamental problem, currently somewhat out of reach and beyond the scope of this study. This chapter describes two methods of producing graphene flakes. The first method utilises electrochemical tools to prepare a high quantity of lower-quality graphene while the second method uses mechanical fracturing or sometimes known as “graphite nanotomy” to produce high-quality graphene at the cost of volume. The chapter’s objective is to characterise the graphene flakes macroscopic physical and spectroscopic properties to provide insight into how defects may manifest properties. Characterisation of graphene's properties is by UV-vis absorption spectroscopy, transmission electron microscopy (TEM), atomic force microscopy (AFM), and Raman. Comparing data collected for each technique provides insight into inherent quality-quantity trade-offs accrued and significant limitations of the materials in potential applications. The aim is to explicitly show where deviations between flakes produced by the two approaches occur. Two relevant questions are: ‘Which is the better graphene preparation process for applications?’ and; ‘Should new methods for producing large quantities of pristine material be developed?’. As we will see, both approaches produce graphene that has the potential for applications, but it is important to note that the fabrication of devices is not within the scope of this research.

2.1 Graphene Flake Production Methods

The diminishment of graphene's physical properties increases with the density of lattice impurities, so it is essential to start with high-quality graphite. The most common graphite source used in the literature is graphite rods, produced by pressing graphite powder[107]. Very few groups attempt to solve this problem by simply starting with a high-quality graphite source *e.g. Highly orientated pyrolytic graphite (HOPG)* is the graphite source used here and is of ZYB grade with a mosaic spread of 0.8 ± 0.2°. Before considering the graphene production methods, it is useful to review the sources of graphite where information on the HOPG starting material provides insight into the graphene products produced in later sections. Figure 7 below shows a schematic representation of HOPG.

2.1.3 HOPG

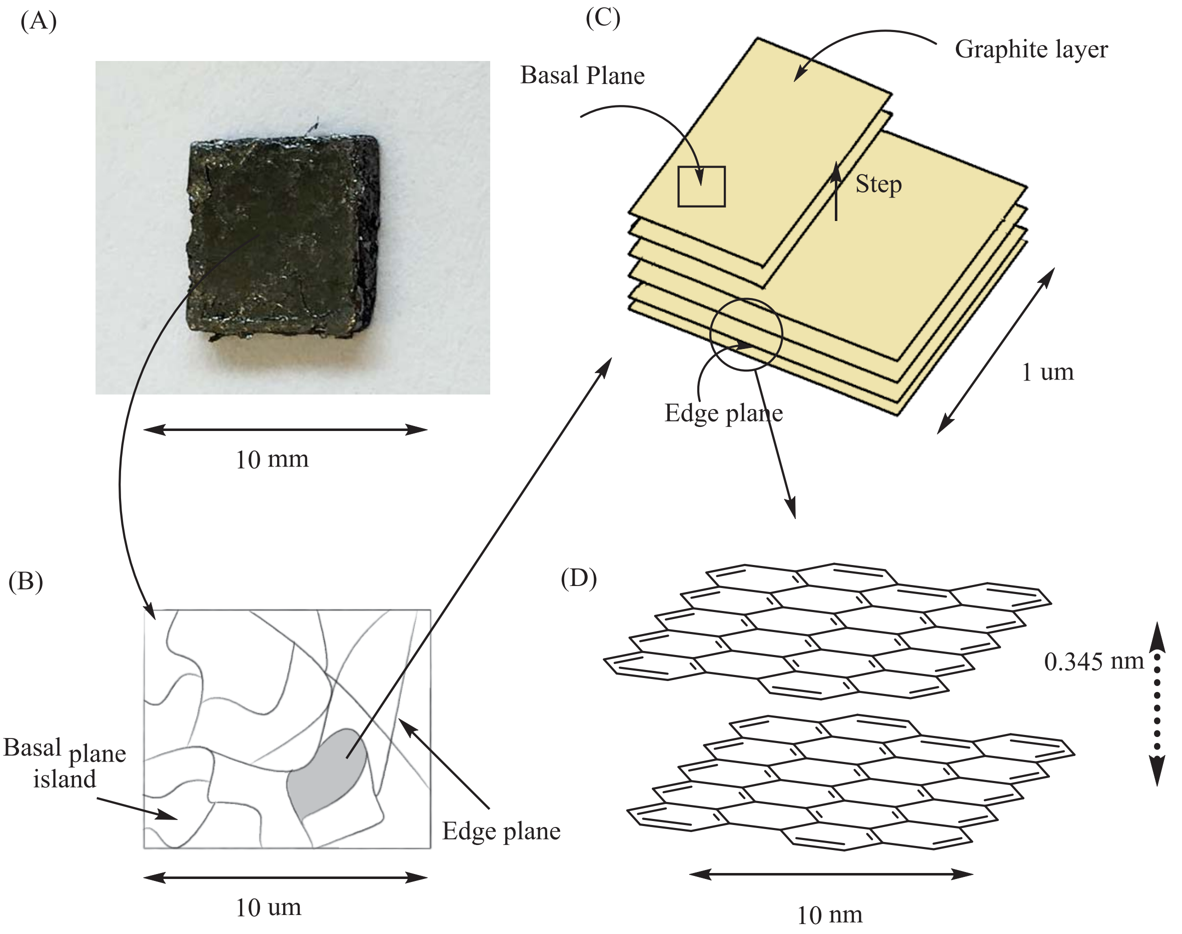

Figure 7: Top-down schematic of HOPG. (A) Bulk image of commercially available 7x7x0.8 mm ZYB grade HOPG. (B) Diagram of discrete basal and edge planes interweaved on HOPG's surface. (C) Graphite layers, steps, basal and edge planes - A microscopic representation. (D) Molecular level view of boundary planes and interlayer spacing or "van der Waals gap" of 0.345 nm.

Figure 7 above shows a schematic representation of HOPG, the graphite source used in graphene production. Figure 7 (A) shows a bulk-scale HOPG piece (7x7x0.8 mm). Zooming in on the piece of HOPG reveals distinct islands of graphite, separated by grain boundaries.

Grain boundaries size and shapes are determined by the *chemical vapour deposition (CVD)* conditions during production of the HOPG[31]. Figure 7 (C) zooms in on a graphite island and reveals the individual layers with edge and basal planes separated by steps. The graphene basal plane is visible, where the separation of edge planes is the van der Waals interatomic interaction distance of 0.345 nm.

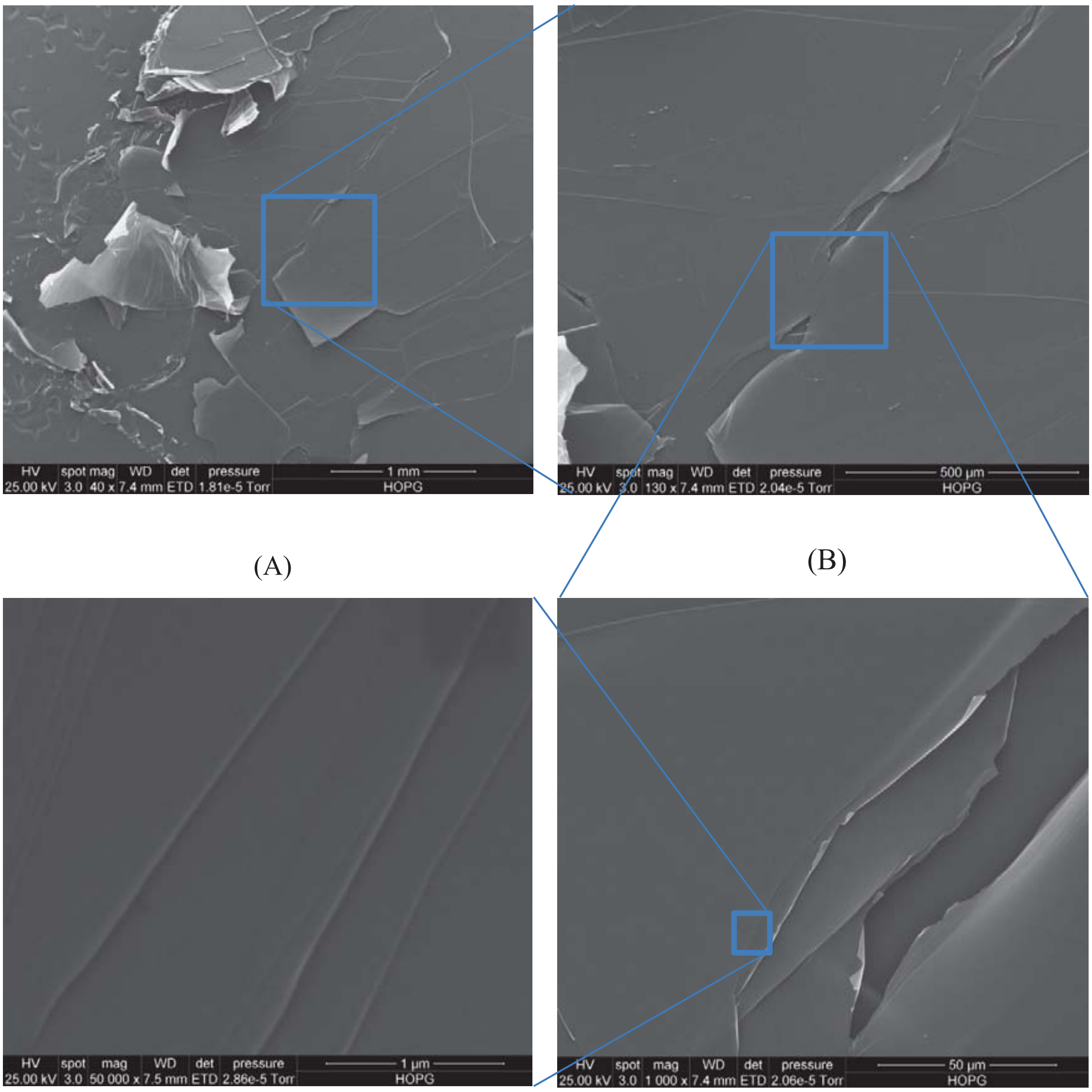

(A) (B)

(D) (C)

Figure 8: Scanning tunneling electron microscopy images of freshly cleaved HOPG. A) Discrete graphite islands consisting of basal and edge planes at 40x magnification. B) Grain boundaries viewed at 130x magnification C) Folding and curling of edges viewed at 1000x magnification D) Individual steps of island planes and wrinkles shown high magnification (50,000x).

Figure 8 shows STEM images of freshly cleaved HOPG obtained on a *FEI STEM, Quanta 200 environmental STEM,*. Images shown are at similar magnification scales to figure 7. These STEM images aid in interpreting graphene production methods in sections 2.1.1 and 2.1.2. Figure 8 (A) shows the discrete, anisotropic island-like planes of HOPG. Figure 8 (B) is at 130x and shows the disappearance of millimetre scale features and appearance of grain boundaries between islands. Zooming in on these cracks in figure 8 (C) (1000x magnification) shows clearly the folding of planes as layers in this graphite source have peeled back as a result of the cleaving of planes during SEM sample preparation. Figure 8 (D) reveals, through 50,000x magnification, individual steps between layers comprising graphite islands, while between these steps, wrinkling is apparent. It is useful to note the interaction energy between graphene sheet is 3.0 $\frac{kJ}{\mathrm{nm^2mol^{-1}}}$. as calculated in the literature[32]. The graphene fragment in figure 7 (D) has an area of 1.8 nm^2 which corresponds to an interaction energy of 5.5 $\frac{kJ}{mol}$. For comparison k_BT at room temperature is 2.5 $\frac{kJ}{mol}$ meaning that a graphene fragment as small as 10 nm^2 has a van der Waals interaction strong enough to overcome thermal fluctuations so the methods of producing graphene described in the follow sections are required.

2.1.2 Liquid Phase Chemical Exfoliation

Edge initiated exfoliation of bulk graphite is a valuable method for cheaply producing large quantities of graphene. The use of electrochemistry[35] for exfoliation is an attractive alternative to other procedures as it does not require complex equipment (only a potentiostat is needed) or methodologies, but is capable of producing large quantities of graphene while adhering to one of the principles of green chemistry by using aqueous solutions. These properties could make electrochemical exfoliation a desirable technique for large-scale industrial adoption. This production technique produces graphene in large quantities, however, are of an uncontrolled size, shape and edge structure making liquid-phase electrochemical exfoliation the higher defect graphene production technique. A description of the electrochemical cell utilised in this section can be found below.

2.1.1.1 Purpose-Built Electrochemical Cell

Establishment of an electrochemical exfoliation protocol for producing graphene of a consistent range of sizes and defects was the motivation behind using a purpose-built electrochemical cell. The design of the electrolytic cell is unique for holding HOPG blocks at their edges. Isolating the sides of the block from the electrolyte means that HOPG will not disintegrate through the removal of large pieces of graphite, but instead obtain layer by layer exfoliation. Figure 9 (A/B) below shows images of the disassembled and assembled cell respectively and highlights HOPG's location within the cell. The images also show the location on the HOPG crystal where it directly contacts the electrolyte solution through the use of an indirect circuit connection with copper foil.

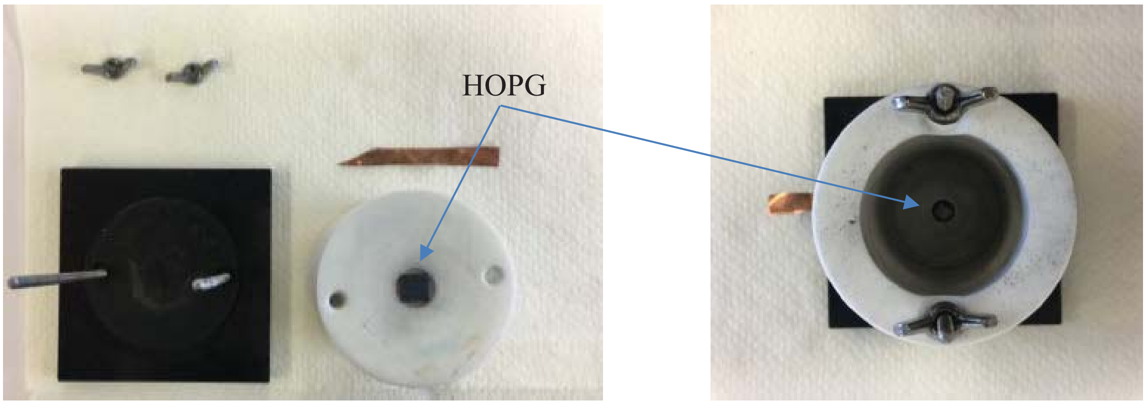

(A) (B)

Figure 9: Photograph of the electrochemical cell used in liquid phase exfoliation of HOPG. A) Disassembled and B) Assembled. Copper was placed over the HOPG block to provide contact, a rubber ring to provide sealing before placing the Teflon block onto the threaded rods and wing nuts to hold the cell in place and provide sufficient force to stop leakage of the electrolyte.

Preparation of the electrolyte was carried out by dissolving $[(NH_4)_2SO_4]_{(aq)}$ in 18 Ω Milli-Q water (0.1 M, pH ≈ 6.5). The exfoliation protocol creates an electrolytic cell by immersing a piece of graphite in $[(NH_4)_2SO_{4\ (aq)}]$. The operation of the potentiostat is in chrono-potentiometric mode at 25.0 mA and dynamic voltage. Applying a current reduces the sulphate ions, gently exfoliating layers of HOPG, producing graphene. Figure 12 below shows the potential-current recorded during exfoliation. Platinum wire is used as the chemically inert counter and reference electrodes. Electrochemical exfoliation has potential large scale application as it produces graphene economically, at the modest rate of 120 mg/hour. It may also introduce oxygen-containing functional groups onto the edges of exfoliated graphene, which could act as chemical handles to introduce further functionality via chemical modification if edges. Another electrochemical technique, cyclic voltammetry, can be used to characterise functionalisation. The material needs to be redox active in the scanning range and at detectable concentration, but previous work has found that edge-terminated carboxylic groups influence redox potentials, and have used these to characterise graphene's edge functionality[33, 34]. The original paper developing the electrochemical exfoliation procedure provides a mechanistic approach to how chemical handles are created exclusively at the edges as opposed to the basal plane. The locations of the defects at edges play a useful role as chemical handles in chapter four where functionalisation relies on these induced defects as chemical handles while not affecting properties which depend on a pristine basal plane *e.g.* electrical conductivity. The outlined chemical mechanism behind electrochemical exfoliation is in Figure 10 below.

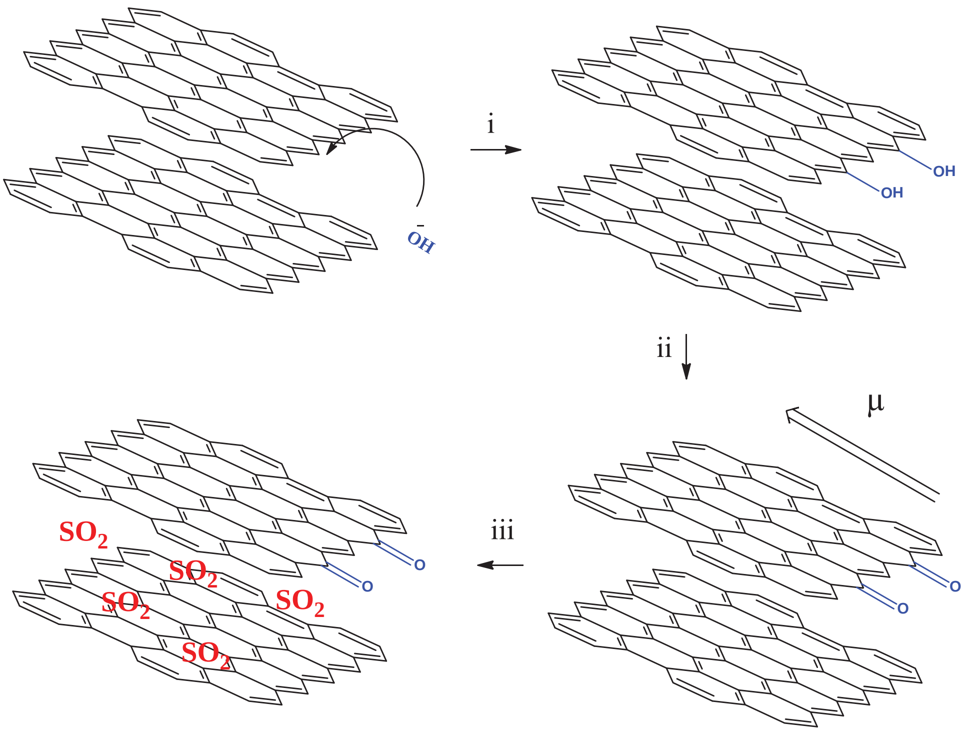

Figure 10: Schematic representation of electrochemical exfoliation as described mechanistically by Parvez et al. (2014)[35] i) Polarisation of electrode potentials. ii) Functional group reduction. iii) The delamination of graphene sheets from the formation of intercalated SO_4^{2-} anions and accumulation of solid deposits in the cell.

Applying a voltage reduces water to hydroxide ions. According to Parvez *et al*. (2014)[35], these ions are nucleophilic enough to attack edges and grain boundaries, but not the basal plane (i). The newly formed edge functional groups are further oxidised by the applied voltage (ii). Oxidation induces charge depolarisation (μ) extending from the edge into the basal plane, weakening the van der Waals interactions between layers and allowing the electrolyte to permeate layers (iii). Reduction of $SO_4^{2-}{}_{(aq)}$ anion to $SO_{2\ (g)}$ causes expansion. The production and expansion of the gas provide the force necessary to push apart layers, producing graphene. Introducing these oxygen functional groups on edges is required to modify graphene (chapter four). Figure 11 below balances the redox processes occurring during electrochemical exfoliation.

$$\begin{array}{ccc}
2H_2O \rightarrow O_2 + 4H^+ + 4e & \text{Anode} & [1] \\
\mathrm{H}SO_4^- + 3H^+ + 2e \rightarrow SO_2 + 2H_2O & \text{Cathode} & [2] \\
\hline
2\mathrm{H}SO_4^- + 2H^+ \rightarrow O_2 + 2SO_2 + 2H_2O & \text{Overall} & [3]
\end{array}$$

Figure 11: Scheme 1. Balanced redox equations of ammonium sulphate assisted liquid phase electrochemical exfoliation under acidic conditions. [1] Oxidation. [2] Reduction. [3] Overall.

Figure 11 shows the redox chemical processes that occur at the platinum anode ([1]) and the working electrode ([2]) under acidic operating conditions to highlight the consumption of the inorganic salt. It is worth noting that at this potential, it is possible for other species such as free radicals to form, which may introduce basal plane defects. Figure 12 below provides a typical current-voltage curve.

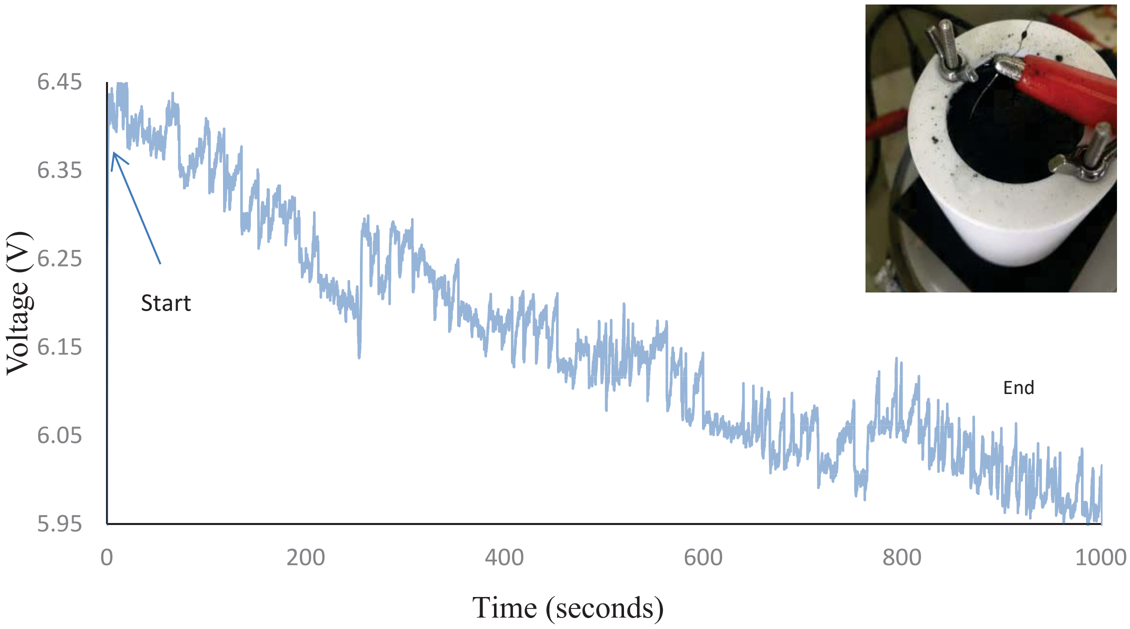

Figure 12: Voltage time curve of electrochemically exfoliating HOPG at 25.0 mA. Inset of electrochemical cell in operation.

Figure 12 above shows the voltage fluctuation over electrochemical exfoliation time scales. The downward trendline is attributed to the decreasing HOPG block thickness as exfoliation occurs, decreasing circuit resistance. As a general guideline, 30 mg is produced in 1000 seconds. The exfoliated material that accumulates at the top of the electrochemical cell (inset) was collected and washed with copious Milli-Q water to remove remaining electrolyte. The resulting black colloidal material is termed *xFlakes*. After electrochemical exfoliation, any remaining carbonaceous material was removed via disassembly, extensive washing and drying before resembling. The following section focuses on describing the pristine graphene production method, graphite nanotomy.

2.1.3 Graphite Nanotomy

Many production methods exist for producing pristine flakes for applications but are challenging to scale-up while maintaining quality[36]. Scaling of production volume results in loss of control over graphenes shape, size and edge structure. This problem needs to be solved before realising large-scale applications with pristine graphene. *Graphite nanotomy (GN)* is a technique that attempts to bridge the gap between low-volume high-quality and high-volume poor-quality production techniques. Mohanty *et al*. research group pioneered graphite nanotomy[40]. In practice, a block of HOPG is partially encased in glue for support and mounted onto the chuck of a microtome's arm (Leica EM UC7 ultramicrotome). GN is a top-down strategy whereby graphene planes are aligned perpendicular to the edge of a diamond knife to fracture graphitic planes via C-C bond strain and consequently breaking in the direction of cleavage.

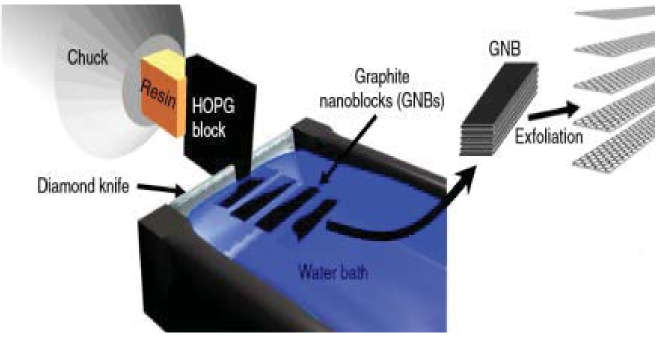

Figure 13: Schematic diagram for the GN production process. Recreated from reference 40 with permission. © Springer Nature (2017).

Members of our research group have produced graphene nanoribbons (width < 100 nm) via diamond-edge-induced nanotomy using step-wise forward cutting increments at 100 nm. Figure 13 is a schematic representation obtained from reference 40 to illustrate graphite-nanotomy. Producing graphene flakes by GN requires nano blocks of HOPG be cut at micron increments to obtain micron scale length and widths. Sonication of cut material organic solvents delaminates graphite blocks, generating micron-sized graphene flakes. The flakes produced via graphite nanotomy by cutting at 1000 nm increments are henceforth called GN-flakes. The largest step-size of the microtome is 5 µm; the GNB dimensions can be controlled down to 20 nm. The quality of the graphene flakes produced are determined by the quality of the graphite source. Since HOPG has a high purity, the flake's basal plane is expected to be of similar quality. During production, C-C bonds are broken, so it is anticipated that GN-flakes has production-induced defects such as dangling bonds at edges. These unsaturated, dangling bonds protruding from edge C atoms are reactive so may react to form chemical bonds with molecules from the ambient air including CO_2, water and nitrogen as supported by computational studies[37, 38]. Ab initio calculations have also shown that passivation by hydroxyls is particularly stable[39]. These computational studies provide evidence of GN's production scope, where there is potential for functionalisation of edges by cutting in a specific atmosphere (although this would require the construction of an atmospheric chamber for the microtome).

2.2 Characterisation of Graphene Flakes

This section will characterise the graphene flakes produced by the electrochemical exfoliation and graphite nanotomy. Novel techniques are used to describe and understand the properties of these materials. Atomic force, electron, and Raman microscopies (AFM, TEM and RM respectively) are utilised below to characterise GN-flakes and xFlakes. UV-vis spectroscopy provides a measure of graphene's electronic energy level and highlights deviations from universal optical absorption.

2.2.1 Atomic Force Microscopy

Atomic force microscopy (AFM) is a scanning probe microscopy technique with resolution on the order of a nanometer, three orders of magnitude better than the diffraction limit of light. The tip of an atomically sharp cantilever is raster scanned over an area of sample spanning tens of microns, measuring local topological properties such as height through monitoring of the interactions between the probing cantilever tip and surface. Above the surface, the van der Waals forces act to decrease the resonance frequency of an oscillating cantilever. From this deviation, measuring the tip-to-sample distance at each point of the scanning area builds a topography map of the sample surface. Topography images are obtained in ambient air through operation in tapping mode with a silicon Tap 190Al-G probe of resonant frequency ≈ 190 kHz. Distinguishing between graphene oxide (GO), and graphene is difficult from topological features alone. Separating these materials can, however, be carried out using phase-contrast imaging in tapping mode. An AFM probe experiences different forces with pristine graphene than the oxidised counterpart due to added oxygen functionalities. AFM is also particularly useful in determining the thickness of graphene flakes. Pristine graphene is ≈ 0.34 nm in thickness while GO is 1.0 nm. Various degrees of oxidation produces a range of thicknesses between these values. Variation in per-layer thickness is due to the hydrophilicity of GO where oxygen functional groups in GO's basal plane interact strongly with ambient water molecules.

2.2.1.1 AFM Sample Preparation

Dispersions of micron-sized graphene are obtained by sonication (*Bandelin SONOREX*) in polar organic solvents. Graphene (0.2 mg) was dispersed in THF (dry, 1.0 ml) with sonicated at 1200 W over 24 hours. Dispersion by bath sonication is via mechanical disruption. The graphene flakes are then stabilised by interactions with the organic solvent. 5 µL of the graphene solution was pipetted onto freshly cleaved Mica, preheated to 45 °C. The residual solvent was allowed to evaporate on a hotplate at 60 ˚C for sixty minutes before being subjected to AFM analysis. Figures 14 and 15 below show AFM images of xFlakes and GN-flakes respectively.

2.2.1.2 xFlakes

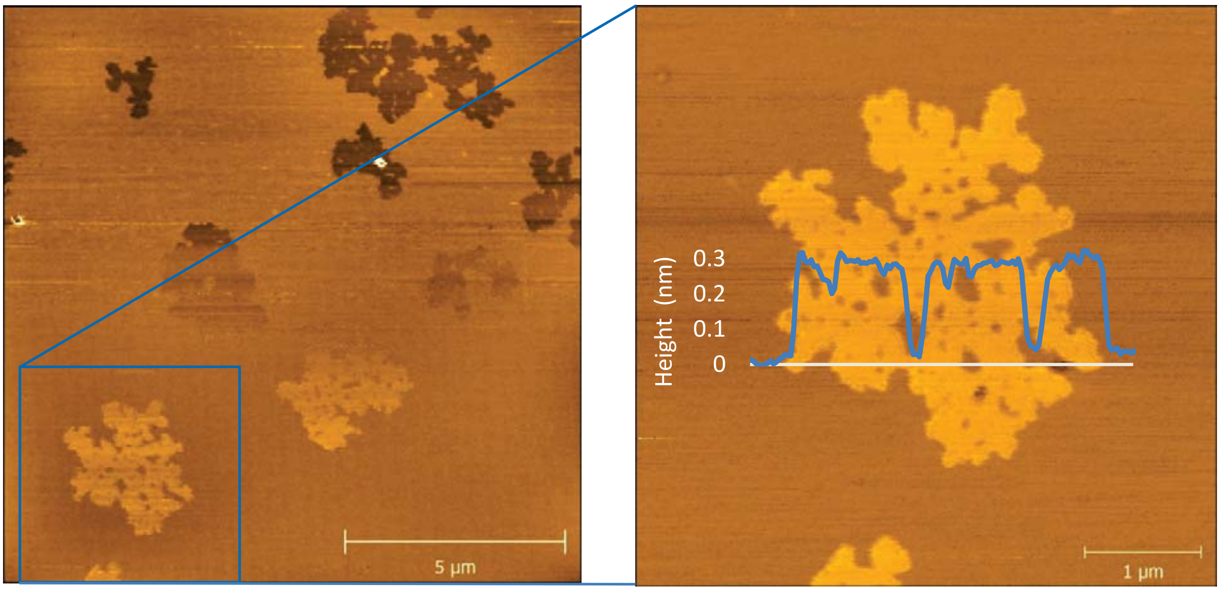

(A) (B)

Figure 14: Representative AFM images of xFlakes dispersed by ultrasonication supported on a Mica substrate. A) 12x12 µm height topography image of atomically thin graphene sheets. B) Phase contrast image of a single 2.5 µm flake and superimposed line cross-sectional height profile. Images recorded in non-contact mode. Note different scale bars.

Figure 14 (A) confirms the successful production of single-layer graphene sheets using liquid-phase electrochemical exfoliation of HOPG. The contrast change down figure 14 (A) is a result of an offset baseline. Contrast changes are a commonly observed artefact that results from subtle changes in apparent substrate height over a large scanning area *e.g.* few degree off-set results in a significant height difference on the other side of the scanning window. The superimposed cross-sectional height profile in figure 14 (B) shows the uniform thickness of xFlakes (0.33 nm) which is consistent with the inter-planar spacing or van der Waals radius of graphene. The thickness proves the graphene-like nature of the sample, as opposed to being graphitic. The experimentally obtainable thickness also demonstrates the excellent dispersibility of this material in organic solvents which is particularly important for solvent-stabilisation over prolonged time periods. The decoration of the basal plane of the flake in figure 14 (B) with 50 - 250 nm holes is immediately apparent. These AFM images are a subsample and may not represent the sample as a whole. Even though smaller holes are possibly present, sample resolution limits prevent them from being resolved. The literature has suggested the holes form via nucleophilic attack of epoxides with the basal plane hydroxide anions[34]. The bond cleavage then results in the formation of tertiary alcohols as adjacent epoxides are 'unzipped'. Another possibility is ultrasonication induces defects where extended sonication time induces defects in the basal plane via shear forces[35].

2.2.1.3 GN-Flakes

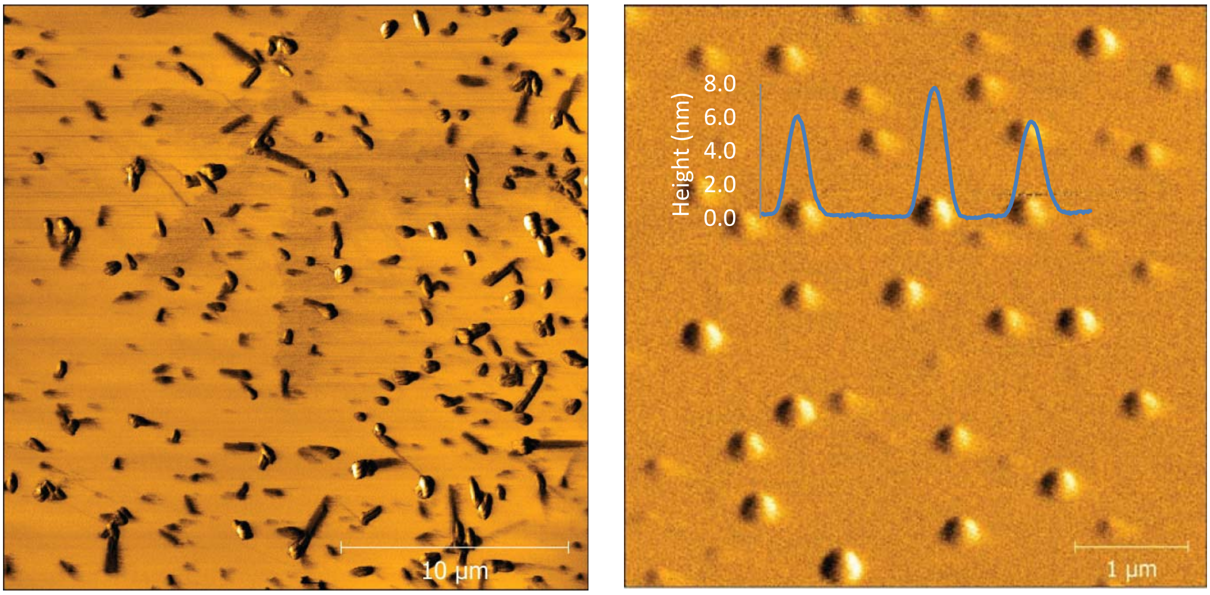

(A) (B)

Figure 15: Representative AFM images of Flakes produced by graphite nanotomy (GN-Flakes). A) 25x25 μm phase contrast image of few-layer graphene on a Mica substrate. B) 5x5 μm height topography image and superimposed line cross-sectional height profile. Images recorded in tapping mode. Note different scale bars.

Figure 15 (A) above shows the AFM phase contrast image scan of GN-flakes on Mica. This typical surface shows a lateral size distribution of 0.5 to 1.5 µm and an inhomogeneous surface topography due to graphene lamination during solvent evaporation. An average thickness of graphene aggregates is 8 - 12 nm as shown by the height profile superimposed onto figure 15 (B) above. The material shown in this image appears smooth and rounded which may result from stacking into controlled dimensions similar to those of the laminated graphite nanoblock counterpart of GN-flakes. Surface modification with oxygenated functionalities is known to induce a degree of hydrophilicity. Graphite nanotomy is thought to be a high-quality production method, so lamination of graphene as the solvent evaporates is favoured more energetically than its oxygen-containing counterpart, xFlakes.

2.2.2 Transmission Electron Microscopy

The small mass of an electron means it is deflected easily by atomic nuclei. Deflection and scattering are due to electrostatic Coulomb interactions between an electron beam and sample. TEM samples are often required to be tens, if not hundreds, of nanometers thick to generate sufficient scatter to be opaque to electron beams. The electron density of graphene allows the acquisition of topography images of even few layer graphene.

Transmission electron microscopes (TEMs) were first built in 1931 and have been an invaluable tool in material sciences ever since. Their development was brought about since the image resolution of optical microscopes is limited by the wavelength of the light source. With TEM's ‘light source' being electrons and the resolution being wavelength dependent, the resolution is obtained by relating the electron wavelength (λ) in nm to energy (E) in electron volts (eV):

$$\lambda = \frac{1.22[nm \cdot eV^{\frac{1}{2}}]}{E^{\frac{1}{2}}[eV^{\frac{1}{2}}]}.$$

As an example, the standard electron beam acceleration is 200 keV electron and results in $\lambda = 0.00251$ nm. This is much smaller than the size of an atom.

2.2.2.1 TEM Sample Preparation

Sample preparation is necessary when TEM characterisation is carried out. Since a tiny proportion of the sample is used to represent the whole, homogeneity is necessary. TEM graphene samples are made by placing a copper coated TEM substrate at the air-liquid interface of graphene in ethanol (0.1 mg/ml) droplet for four minutes, wicking away excess solvent, then allowing to air dry. An FEI Tecnai G2 Biotwin transmission electron microscope was used to obtain TEM micrograph images shown in figure 16 below. The operational resolution is 3.0 nm, so a real lattice image is not obtainable, although a diffraction pattern could be obtained.

2.2.2.2 xFlakes

structure

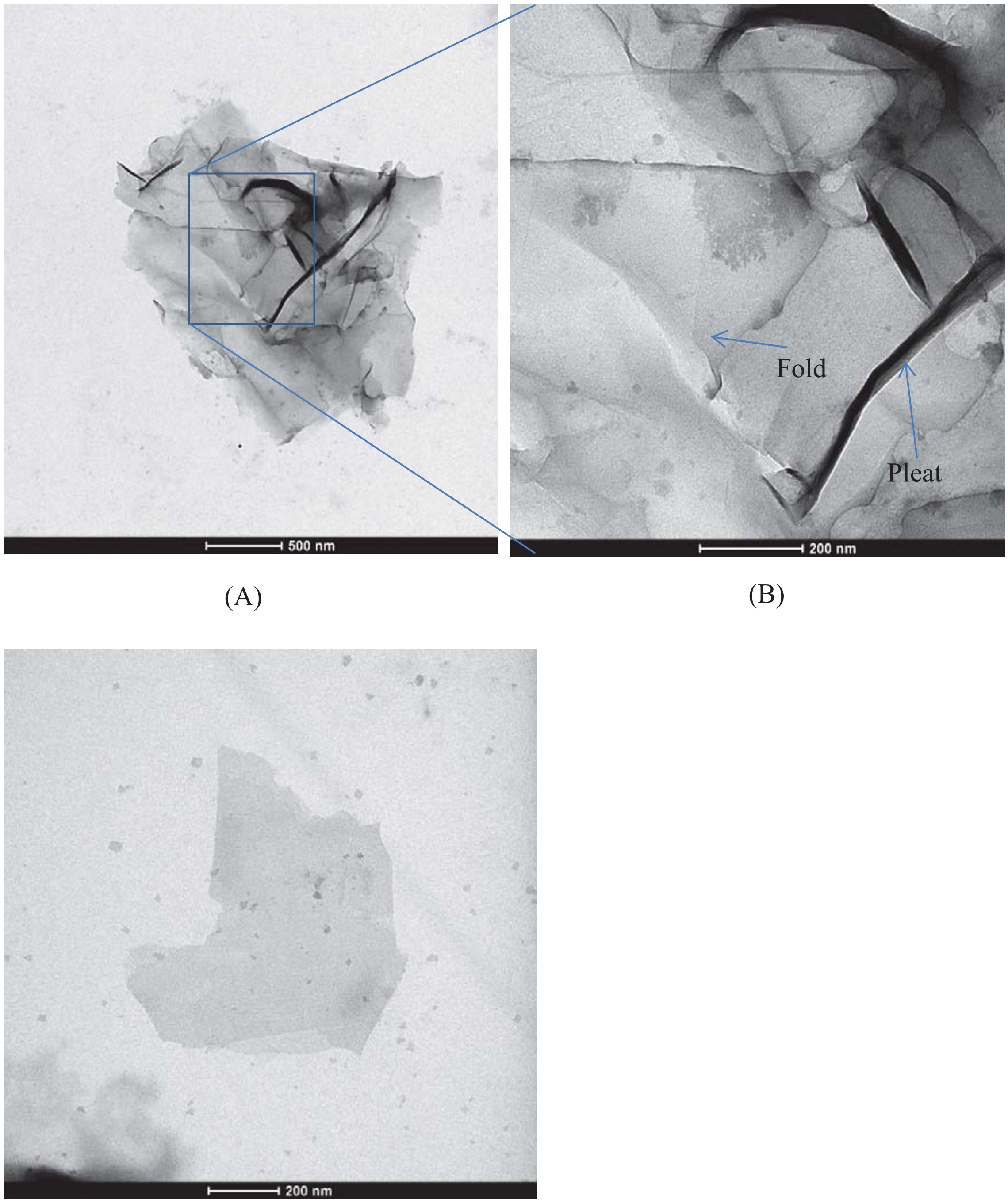

(A) (B)

Figure 16: TEM micrographs of micrometer-scale xFlakes draped onto a substrate. A) 1.5 µm flake ‘draped’ over the TEM grid B) Close-up view of flake noting a pleat and fold C) 0.6 µm flake exhibiting folding at edges. Note different scale bars.

TEM micrograph images in figure 16 above show graphene sheets are continuous but have little resistance to bending and folding. xFlakes vary in aspect ratios with diameters distributed around 0.5 - 2 µm. At this magnification, the atomically thick layers ripple and exhibit folds, pleats and corners at their terminations as the material conforms to the TEM substrate. The appearance of xFlakes also varies among images in that some appear crumpled and others flat or having folded edges. Few-layer graphene resists compressional strain well, but it is prone to fold up if even a small transverse force is applied[103]. Graphene sheets behave analogously to pieces of silk fabric draped over a surface: wrinkles, folds and crumpling upon itself in complex ways appear common[103, 104]. The literature shows this behaviour is typical of larger (> 500 nm) pieces of graphene[43]. The size range being a tipping point for competition between elastic and torsional restoring forces[103].The result of transverse forces can be seen experimentally in TEM micrograph images of xFlakes above in figure 16 (A/B). The crumpling is of particular relevance to this work as liquid phase processing is illustrated in later chapters. Chemical modifications may not go to completion if crumpling in solution is spontaneous *e.g.* a large proportion of the surface area may not be exposed to the solvent. Therefore, complete dispersion to single layers is necessary to utilise the entire 2600 $m^2 g^{-1}$ of available surface area. Figure 16 (C) shows a sheet of graphene absent of crumpling but features a folded edge. The folding may be an experimentally induced artefact where thermal contraction of TEM grid relieves stress as a vacuum develops. Molecular dynamics simulations have revealed that thermally induced strain results in the expansion in the c principle axes with contraction of basal plane dimensions as a result of defects within the basal plane[44]. Folding of graphene flakes is a very complicated process and is not fully understood however from a theoretical standpoint, literature has provided insights into the underlying process. From a fundamental point of view, solitons[43] and wrinklons[46] appeared to be intrinsic to graphene materials and produced the corrugations, folds and ripples. A soliton is a quasiparticle propagating as a travelling non-dissipative wave (elastic, compressional wave) and a wrinklon is a localised transition region where two wrinkles (solitons) merge. Their appearance in TEM micrographs is a result of ‘freezing out’ during the solvent evaporation process. *Ab initio* simulations suggest molecules physisorb onto corrugated graphene with large molecules adsorbing onto the tips of a ripple and small molecules in valleys. Adsorption occurs at peaks as ripples have lower electron density while the electron density in valleys is increased[45]. A review article describing this process in depth can be found in Deng *et al.* (2014)[47].

2.2.2.3 GN-Flakes

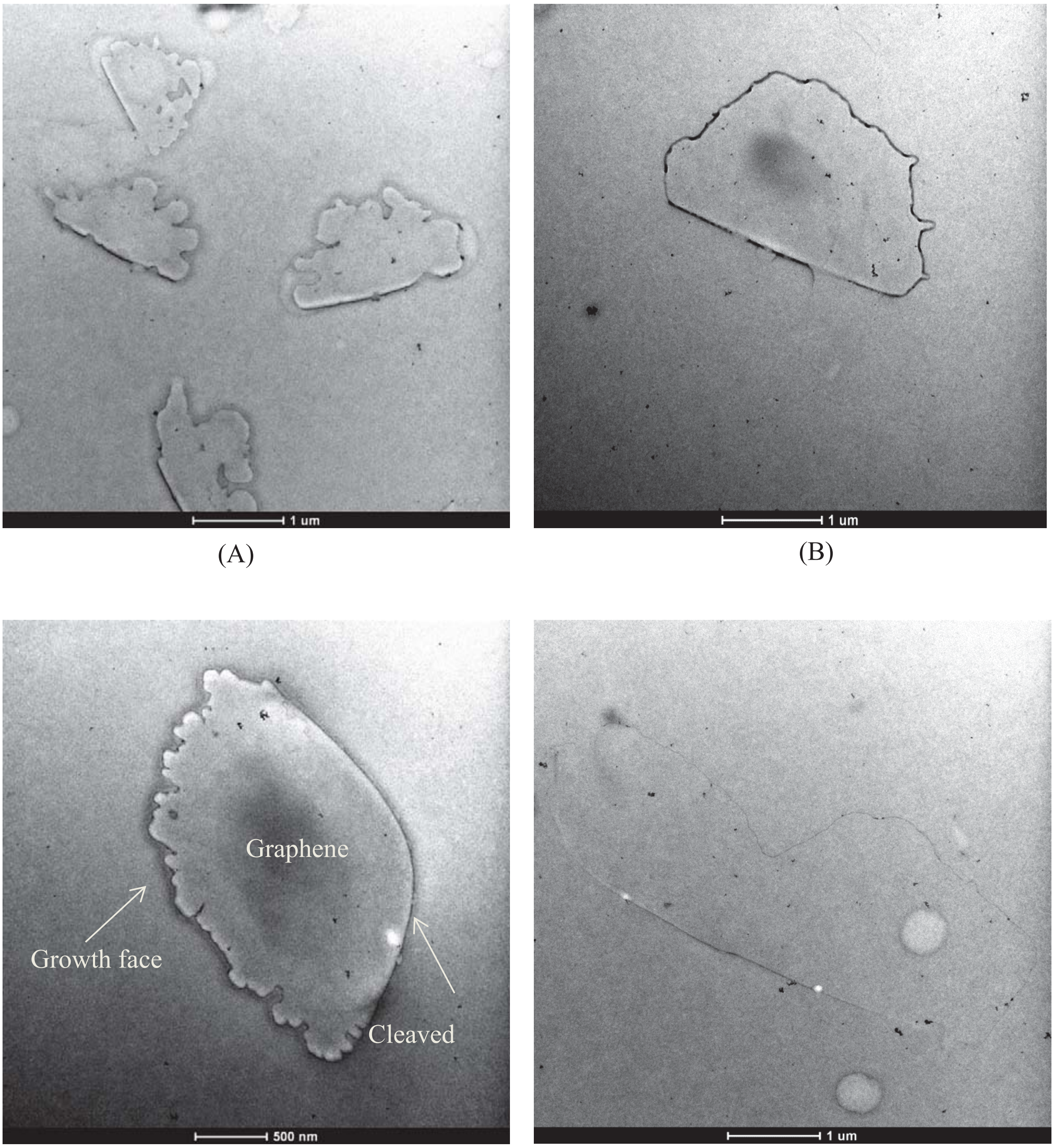

(A) (B)

(C) (D)

Figure 17: TEM micrographs of GN-Flakes. A) 5x5 µm image of four flakes of ≈ 1x1 µm each. B) ≈ 2x2 µm GN-flake. C) Magnified image of a 1x1 µm GN-flake showing clearly the cleaved and growth faces. D) An atypical flake shaped flake.

Figure 17 shows TEM micrograph images of GN-flakes. These flakes vary in aspect ratios with diameters distributed around 1 - 2 µm. In contrast to xFlakes, GN-Flakes exhibits less folding or wrinkling of edges and the basal plane respectively. GN-Flakes have a smooth, flat side, denoted 'cleaved face' in figure 17 (C). This face may be the one cut directly during production. The side denoted 'growth face' is suspected to arise from the growth of HOPG due to similarities with CVD graphene edges[31]. It is important to note this could also result from tearing as the knife cleaves carbon planes. Figure 17 (D) shows a flake with atypical aspect ratios but still exhibits smooth and rough faces.

2.3 Raman Microscopy

Raman spectroscopy is widely used to characterise graphene and is complementary to infrared spectroscopy. Briefly, Raman active bands arise from a change in polarizability while infrared bands are most intense when polarity changes along the direction of vibration (along a normal mode). Graphene, having easily polarised delocalized (and mobile) electrons means Raman-microscopy is a powerful characterisation tool for graphene (and other carbon nanomaterials). Raman provides a wealth of information on a broad range of physical properties such as density of defects, sample topology or degree of oxidation[48]. The major bands in graphene are the D, G and 2D peaks. The G band is due to the longitudinal optical mode of graphene's lattice. The D-band arises from an in-phase combination of benzene ring deformations and is forbidden by translational symmetry in a perfect graphene lattice. The 2D band is the overtone of the D band (as the name suggests). The intensity of the D band increases with the introduction of defects, or reduction in local symmetry. Correlation of the distribution of defects is possible using the width of the D band[48]. These defects can be structural in nature, for example, graphene's edges are 'defects'. When the excitation focus includes edges, even pristine graphene has a large D peak. They may also be from the disorder within the carbon lattice, for example, Stone-Wales defects, vacancies or dopants. Raman literature has discerned fundamental properties of graphene, such as the effects of layer stacking (crystallinity perpendicular to the graphene plane) and the effect it has on the optical properties of graphene[49].

2.3.1 Raman Sample Preparation and Collection Conditions

The Raman spectra shown in figure 18 below were obtained on graphene aggregates prepared by drop casting 50 µL of a 0.1 mg/ml sample of graphene dispersed in THF onto a glass cover slip and air drying. A home-built Raman microscope based on an Olympus IX70 inverted fluorescence microscope with 532 nm (2.33 eV) laser excitation in a confocal microscopy arrangement is utilised to obtained data. The sample was irradiated at 1.0 ± 0.5 mW to avoid sample damage and directed by an OptiGrate Volume Bragg bandpass filter or Iridian Spectral Technologies Raman edge filter using an objective lens of numerical aperture 0.65 to a spot size of 2 µm. Raman scattering was collimated with the same objective so, through a backscattering mode, Raman scattering is collimated, and Raleigh removed with a series of OptiGrate Volume Bragg Notch filters before focusing into a 50 µm diameter optical fibre aligned on the entrance of an Acton 2500i spectrograph or Princeton LS785 lens spectrograph. In both cases, detection was by a CCD camera.

2.3.2 Raman Microscopy of Graphene Flakes

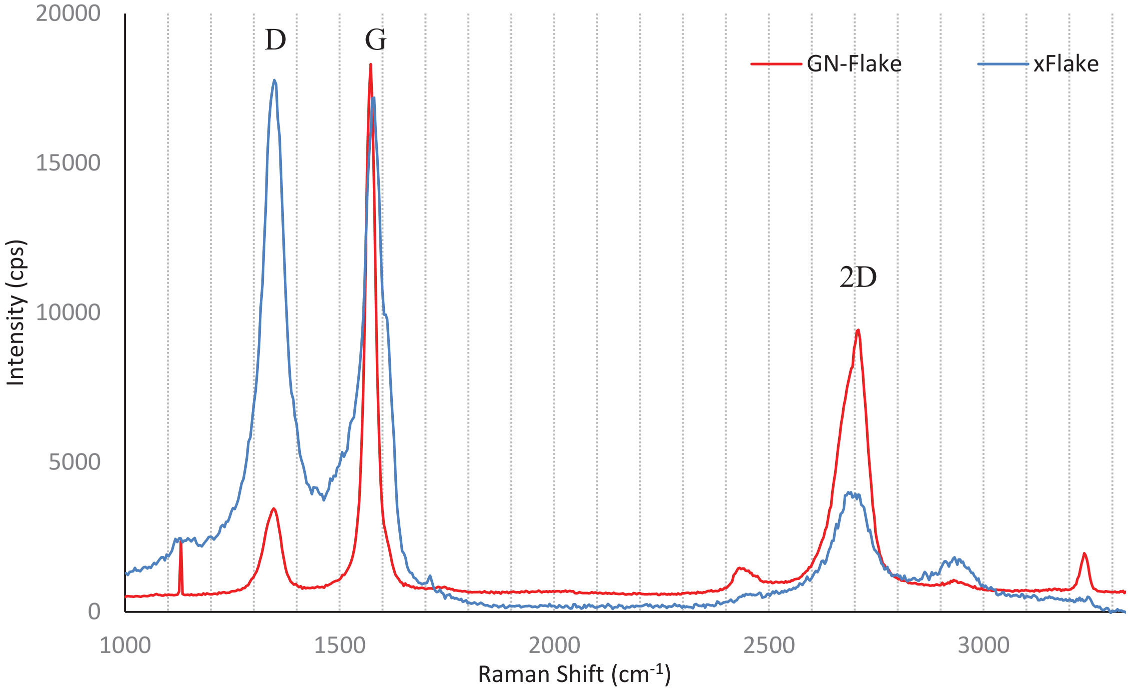

Figure 18: Raman spectra of xFlakes and GN-Flakes over the 1000-3350 cm^{-1} spectral range. Spectra offset for clarity.

Figure 18 above shows the Raman spectra of xFlakes and GN-Flakes over the 1000-3350 cm^{-1} spectral range and are offset for clarity. The D band is caused by out-of-plane vibration and attributed to structural defects. The D band appears at 1342 and 1344 cm^{-1} in GN-flakes and xFlakes respectively. The G band is a result of in-plane vibrations of sp^2 hybridised carbon atoms and appears at 1572 and 1580 in GN flakes and xFlakes respectively. The 2D band appears at 2705 and 2681 cm^{-1} in GN-flakes and xFlakes respectively. The band changes in shape, width and position as the number of layers increase towards bulk graphite. The most important insight obtained from figure 18 is the ratio of intensities of the D and G bands. $\frac{I_D}{I_G}$ is a measure of the defects present in graphene's lattice. This ratio can be used to directly compare the relative number of defects between xFlakes and GN-Flakes. The $\frac{I_D}{I_G}$ of xFlakes is 1.02 and 0.19 for GN-flakes. This indicates that xFlakes have a significantly higher number of edges and basal planes defects compared to GN-flakes. These ratios thus confirm that electrochemical exfoliation and graphite nanotomy are high and low (relative) defect production methods for graphene flakes.

2.4 Ultraviolet-Visible Spectroscopy

Transitions of π systems of aromatic rings occur in the ultraviolet and visible region and show characteristic features for defects. The UV-vis absorption spectra of xFlakes and GN-Flakes described below exhibit unusual band shapes and are thought to be Fano-type. The attribution is to excitonic states and discussed in section 2.4.3.

2.4.1 Preparation of UV-vis Absorption Spectroscopy Samples

Dispersions of Graphene materials in organic solvents are unstable without sonication making liquid-phase UV-vis characterisation a challenge. This problem was solved by the characterisation of the materials as solids. Spectra are obtained by deposition of 100 μL of a 1 mg/ml graphene sample dispersed in THF onto a quartz cuvette, tilting to the side and allowing slow evaporation overnight to form a thin film. A clean, empty quartz cuvette is used as a reference. Spectra were recorded on a Shimadzu UV-1800 spectrometer. Graphene exhibits a universal absorbance of $\frac{\pi e^2}{\hbar c} = 0.023 = 2.3\ \%$ per layer over the ultraviolet-near infrared spectral region where c, e and ħ are respectively the speed of light in vacuum, the electronic charge and reduced Planck constant. The universal absorbance is laid over the UV-vis absorption spectra of xFlakes and GN-Flakes below.

Recalling from chapter one, Fano line shapes take the form[114]:

$$C\,\frac{(s+q)^2}{1+s^2} \text{ where } s = \frac{E-E_{\psi}}{\frac{\gamma}{2}} \text{ and coupling strength, q.}$$

The lineshapes are fit to UV-vis data in figure 19/20 (B) below with parameter values summarised in Table 1 below.

Parameter	**xFlake**	**GN-flake**
Maximum wavelength, E (eV)	4.2	1.2
Lineshape Width, γ (eV)	3	0.2
Coupling Strength, q	2.8	0.4

Table 1: List of parameters for Fano line shapes used to fit SEIRAS spectra of xFlakes and GN-flakes.

2.4.2 xFlakes

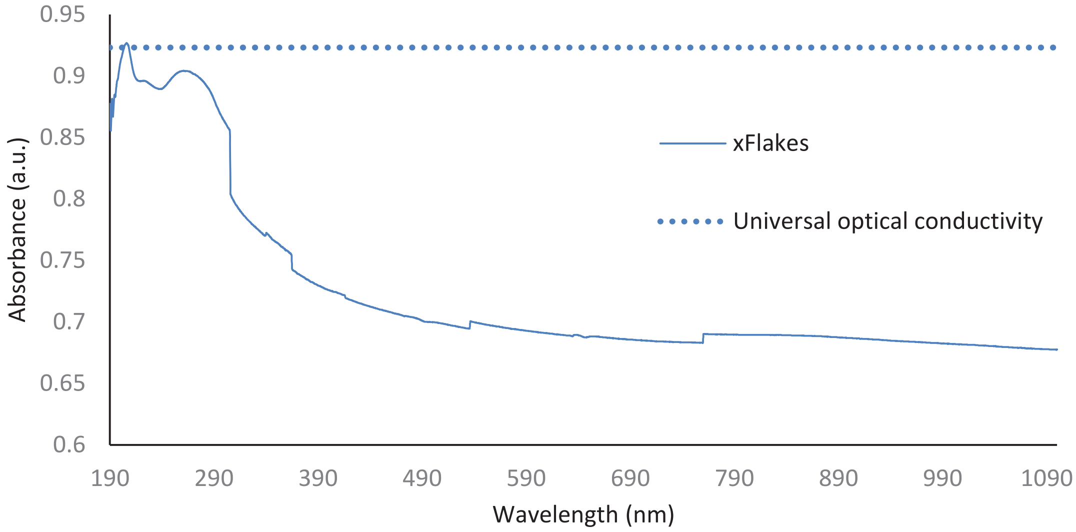

(A)

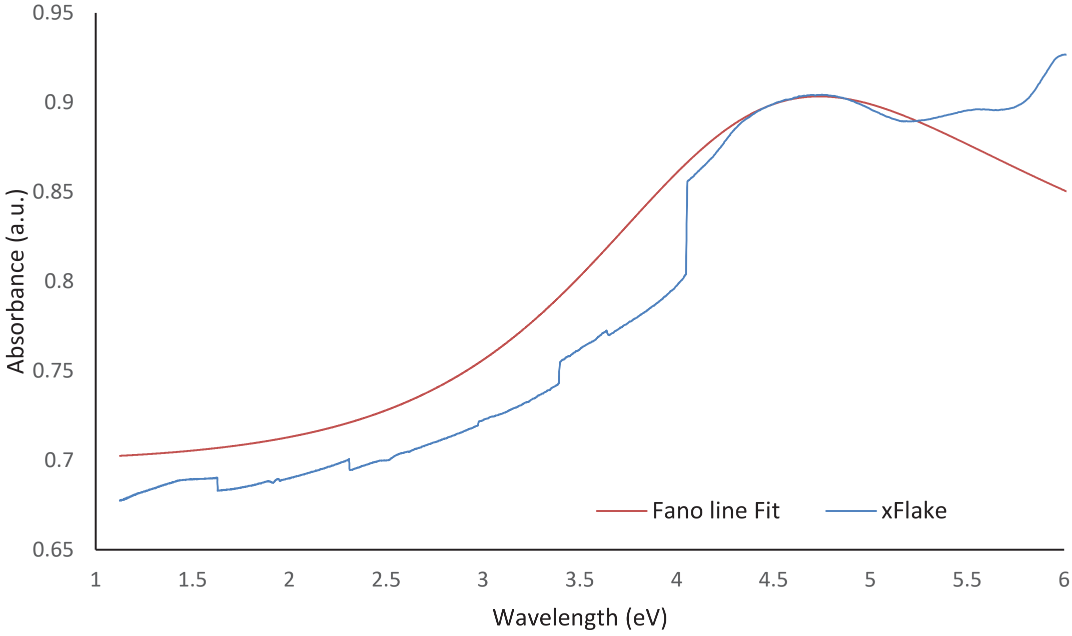

(B)

Figure 19: A) UV-visible spectra of xFlakes as a thin solid film on Quartz over the 190-1100 nm wavelength range. The dashed line is the universal optical conductivity and B) Fano line shape fit to UV-vis absorption spectrum of xFlakes. Note different units.

Figure 19 (A) above shows the UV-vis absorption of xFlakes. Assignments of the absorption band at 206 nm ($\pi \rightarrow \pi^*$) is to carbon bonding in aromatic sp^2 clusters while 270 nm is assigned to C-O ($n \rightarrow \pi^*$)[50]. The spectrum has been fit with a Fano type line shape to account for the deviation from universal absorption. The coupling constant, q for this Fano line shape was 2.8, meaning the interference is negative below the resonance and positive above it. From the lower energy side, the absorption increases slowly towards the resonance maxima at 4.5 eV and decreases at higher energies. The line width is 3 eV meaning the band shape is very wide. The line shape appears to fit the spectrum reasonably well at longer wavelengths, but begins to fail towards the ultraviolet region. Details on the underlying mechanism are discussed in section 2.5.4.

2.4.3 GN-Flakes

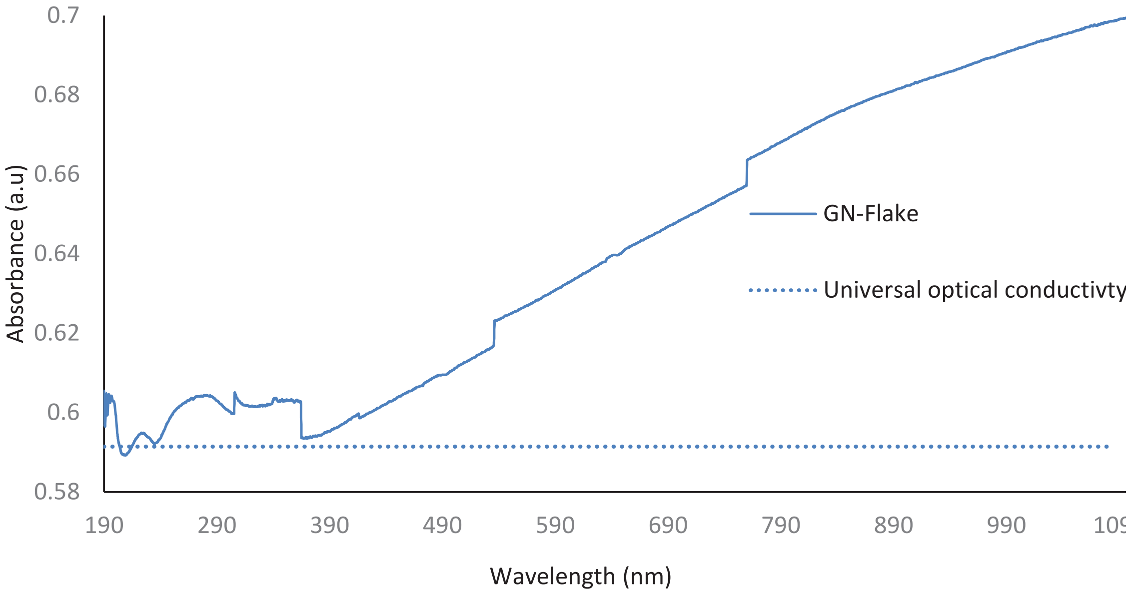

(A)

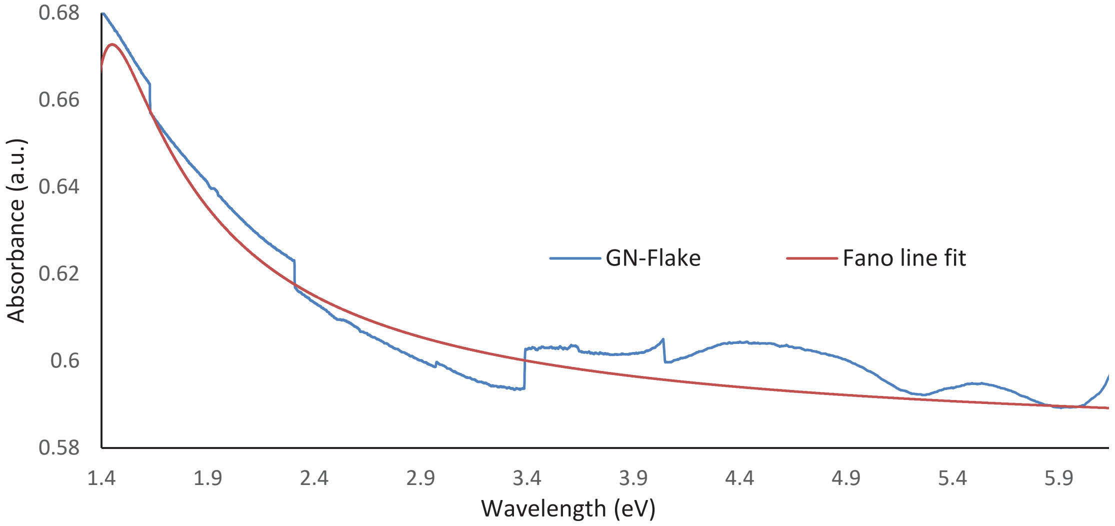

(B)

Figure 20: A) UV-visible absorption spectra of GN-Flakes from 190-1100 nm run on a quartz substrate and B) Fano lineshape fit to UV-Vis spectrum of GN-Flakes over the 1.4 – 6.0 eV spectral range. Note different units.

Figure 20 (A) above shows the UV-vis absorption of GN-Flakes. Characteristic absorptions are at 228 nm ($\pi \rightarrow \pi^*$) and 290 nm C-O ($n \rightarrow \pi^*$). The optical absorbance of GN-Flakes shows a rather significant deviation from the universal absorbance. It is interesting to note that xFlakes in figure 19 above also deviates from universal absorbance, but in the opposite direction. Deviations from universal optical absorption may be a result of many-body charge carrier interactions within or between layers of graphene[25]. To account for this, the literature models the line shape as a Fano resonance[114]. Figure 20 (B) overlays a Fano line shape to the spectra above which describes the data well from the ultraviolet to the NIR.

The coupling constant, q for figure 20 (B)'s Fano line shape was 0.4 meaning the interaction strength was much weaker than in xFlakes above. The interference is positive below the resonance, and negative above it and the absorption decreases slowly towards the ultraviolet region. The line width was 0.2 eV which is very narrow but due to the small coupling value towards higher energies; the lineshape has a large width. Overall, the line shape appears to fit the spectrum reasonably well at longer wavelengths but begins to fail towards the ultraviolet region. A discussion on the underlying mechanisms is in section 2.4.4.

2.4.4 Excitonic States

The UV-vis absorption spectra of the graphene materials in Figures 19 and 20 exhibit unusual steps and drop-offs in absorbance. It is unknown if these asymmetric bands are a result of a substrate interaction or a property intrinsic to graphene itself but a brief discussion of their origins follows. Fano's theory is used here as described in chapter one to explain the distinctly asymmetric line shape as an interference effects. The excitonic resonance is explained within a phenomenological model of Fano as an interference between an excited electronic state (electron-hole pair) that is strongly coupled to a band continuum (phonon). In practice, the bands in Figures 19 and 20 could be from electron-phonon coupling originating from electronic transitions and defects. A saddle point in the electronic band structure of graphene (and other two-dimensional materials) leads to a divergence in the density of states (DOS). These jumps in the derivative of the DOS are known as van Hove singularities[109] and have been observed in graphene as asymmetric bands around 300 nm[108]. In the case of graphene, the energy dispersion near the M-point of graphene is a locally flat saddle point meaning the derivative at this energy is zero. Since the density of states is zero at this point, electronic transitions can only be to states above or below resulting in a substantial increase or decrease in energy around the vHs. The result is an asymmetric band shape[51].

Related to the UV-vis band asymmetry is the phenomena of spin polarisation. In carbon, shared peaks in the DOS leads to electron localisation on zigzag edges which has been known to causes local lattice distortions as a result of electron-phonon interactions[52]. Observing these interactions in this system may provide insights into the chemical (edge) nature of graphene where this type of phenomena is observed through electron localisation at zigzag edges or free-radical like zigzag edges with dangling bonds.

2.5 Summary

At the beginning of this chapter, two questions were asked: ‘Which is the better graphene preparation process for applications?’ and ‘Should new methods be developed for producing large quantities of pristine material?’. The aim was to explicitly show where deviations between flakes produced by the two approaches occur.

Throughout this chapter, experimental data concerning the production of graphene by two methods and the materials characterisation by numerous spectroscopic and microscopic techniques to contrast the properties of these materials, is summarised. I have highlighted key literature to explain where the materials deviate and where appropriate, described novel properties using pioneering works to highlight underlying mechanisms. The graphene production methods were laid out such that researchers may recreate and improve upon what was done here without having to develop production methods tediously. Raman microscopy proved that graphite nanotomy is a high-quality, low-quantity production technique while liquid-phase electrochemical exfoliation is a lower quantity but high-quantity method based on $\frac{I_D}{I_G}$ ratios of 0.19 and 1.02 respectivly. These ratios make it empirically clear that xFlakes are in the middle of the defect continuum with graphene oxide being at one extreme, and CVD graphene the other. GN-Flakes of $\frac{I_D}{I_G}$ 0.19 is higher than CVD, where the ratio for CVD is very close to zero. AFM showed xFlakes riddled with holes in the tens of nanometer size range while GN-Flakes appeared smooth and rounded due to the low number of defects causing lamination. Literature accepts that graphene produced via electrochemical exfoliation methods produces oxygen defects, making lamination energetically less favoured. TEM images showed the tendancy of xFlakes to fold and crumple via Brownian motion, while GN-flakes were structurally more ridged, appearing flat.

In the context of applications for these materials in devices, both exhibit enormous potential. Both approaches produce material that has potential as a carbon-based material for applications, and no clear answer is drawn. If one thing is clear in the graphene literature, the vast majority of devices relies on inherent defects. There are many outstanding properties exhibited by GN-flakes, but many devices often require post treatment to introduce structural confirmations, defects or a particular impurity or functionality that provide the desired physical, spectral or electronic property. A similar argument can be made for xFlakes where it may exhibit too many defects. It is left up to the researcher to decide what density of defects suits the desired application. The physical properties of these materials were studied in this chapter, while chapter three describes the development of a technique used to probe the chemical structure.

Chapter Three – Theory of Molecular Vibrations and Development of SEIRAS

Background

The compatibility of graphene with metals, biomolecules, polymers and other materials is essential to its transition to real-world applications. Understanding the chemistry of graphene is the key to this realisation. Advances in the understanding of the edge morphology of graphene flakes produced in chapter two will improve the ability to add functionality through chemical modification. For example, it would enable the use of reactions that target specific functionality. Edges are the preferred sites to attach functional groups, due to their unique electronic and chemical properties which differ from the bulk due to the relative inertness of the basal plane. Development of graphene functionalisation is limited by the sensitivity of characterisation techniques. Spectroscopic mid-infrared characterisation is possibly one of the most convenient and fastest methods to characterise graphene oxide, as spectral libraries relate vibrational bands to the presence of a functional group. However, the number of modifiable defects in pristine graphene is exceedingly small when compared to the sea of chemically inert sp^2 hybridised carbon atoms in the basal plane. The number of modifiable defects is calculated in section 3.1. The objective of this chapter is the development of *surface enhanced infrared reflection absorption spectroscopy (SEIRAS)* for the routine characterisation of low-defect graphene materials in the mid-IR spectral region. SEIRAS is of particular use for characterising graphene materials produced in chapters four and five. Background to SEIRAS is discussed briefly before a theoretical discussion on the underlying enhancement mechanisms unique to graphene is laid out. The final section describes experimental details of preparing and characterising SEIRAS substrates.

3.0 Introduction

SEIRAS of graphene utilises plasmon, and possibly phonon modes[78] to confine electromagnetic fields to an interface of a dielectric, and an insulating surface to length scales much smaller than the wavelength to light. ‘Surface enhancement’ is defined, in the context of SEIRAS, as the enhancement of the intensity of the optical signal in the mid-IR spectral region. The SEIRA effect is a well-known phenomenon characterised by the enhancement of mid-IR absorption bands of thin layers of analytes in the presence of discontinuous (island-like) discrete particles of noble coinage metals *e.g.* silver or gold[60]. The application of plasmonics based on nanostructured coinage metals utilises highly confined, localised fields to provide extraordinary sensitivity to a structure’s surface features. Surface enhanced spectroscopy is a complex field that includes different surfaces, enhancement mechanisms and sampling conditions. SEIRAS has, for example, been utilised in many different optical configurations since the initial experiments were carried out *e.g.* attenuated total reflectance (ATR), transmission or microscopy. Researchers have exploited this in a versatile range of applications *e.g.* studying the molecular adsorption of gases to noble metals[53], the orientation of self-assembled monolayers (SAMs)[54], protein binding to cellular membranes[55] and gas sensing[56]. FTIR microscope accessories in conjunction with lithographically produced plasmonic devices have also been used for gas molecule sensing[57]. Essentially, wherever a high level of mid-IR sensitivity is required, SEIRAS is exploited.

3.1 Infrared Spectroscopy

Infrared spectroscopy, in particular, the fingerprint region (650 to 1500 cm^{-1}) is a powerful characterisation method for graphene and other materials containing organic functionalities. Organic materials have characteristic frequencies extending to 4000 cm^{-1} and through the use spectral libraries where the vibrational characteristics of many functional groups are known, IR spectroscopy provides insight into chemical functionalisation of graphene material functionalities. The intensity of infrared absorption is dependent on the derivative of the dipole moment (relative to the vibrational mode's normal coordinate). Due to a weak light-matter interaction between infrared light and nanoscale materials such as graphene, obtaining absorption data within this region has been a major challenge due to sensitivity issues. The calculation below shows that mid-IR measurements of low-defect graphene require surface enhancement to obtain a sufficient signal-to-noise (SNR) ratio. Graphene flakes microscale lateral dimensions, so the relative number of atoms at edges is exceedingly small. The calculation begins with the repeat distance along the armchair and zigzag edges.

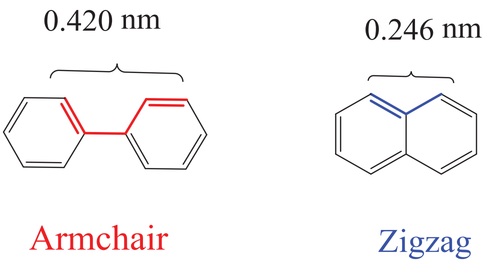

Figure 21: Schematic definition of graphene edge faces and distance of repeating units

An armchair edge has four carbon atoms in a 0.42 nm distance of which two are reactive so 0.21 nm per reactive carbon. For a zigzag edge, there is one reactive carbon atom per ring or:

$$\frac{0.246\ \mathrm{nm}}{\mathrm{per\ reactive\ C}}$$

A 50:50 mixture of zigzag and armchair edges gives an average distance between reactive carbons as

$$0.21\ \mathrm{nm} + \frac{0.246\ \mathrm{nm}}{2} = 0.228\ \mathrm{nm}$$

Assuming graphene flakes are 1 μm × 1 μm then the number of reactive carbon atoms per flake is

$$4\ \mu\mathrm{m} \times \frac{1000\ \mathrm{nm}}{1\ \mu\mathrm{m}} \times \frac{\mathrm{reactive\ C}}{0.228\ \mathrm{nm}} = 17,500\ \mathrm{reactive\ C}$$

With approximately 19,000,000 carbon atoms per flake or molar mass of 233,000,000 $\frac{\mathrm{g}}{\mathrm{mol}}$ then the amount of reactive carbons in 5.0 mg of graphene is:

$$\frac{5\ \mathrm{mg}}{1000\ \mathrm{mg/g}} \times \frac{1}{2.33 \times 10^{8}\ \mathrm{g\ mol^{-1}}} \times \frac{1.75 \times 10^{4}}{1.9 \times 10^{7}} = 1.94 \times 10^{-14}\ \mathrm{mol}$$

It is clear that highly sensitive techniques are required to probe these femtomolar functionalisation concentrations. The prominent problem with spectroscopic methods such as mid-IR for characterising pristine graphene in the mid-IR is signal intensity. Synchrotron sources are necessary to produce the needed far-field intensity but SEIRAS, as described in section 3.1 below, via near-field optical coupling provides the intensity required to detect edges and functional groups utilising the near-field.

3.2 SEIRAS Enhancement

The SEIRA effect, as one of the *surface plasmon resonance (SPR)* phenomena, was originally discovered in 1980[58]. It was appealing because of its practical application in detection of trace amounts of a substance applied to metal films showing mid-IR signal enhancement factors on the order of 10^3. The literature has not studied the origins of SEIRAS enhancement factors exhaustively but by analogy with the accepted mechanisms of *surface-enhanced Raman spectroscopy (SERS)* has origins attributed to plasmonic and molecular enhancement factors. It is important to note that SERS also has contributions from effects such as resonance Raman scattering which is not present in SEIRAS. These effects, along with others, contribute to a theoretical enhancement factors observed in SEIRAS of 10^3 and over 10^{10} in SERS. SEIRA enhancement factors may seem insignificant compared to those obtain in SERS. However, the average cross-section of infrared absorptions is nine orders of magnitude higher than an equivalent Raman cross-section. Agreement between theoretical models and experimental enhancements Support the proposed mechanisms of SEIRAS. At least two mechanisms are prevalent, plasmonic and molecular enhancement factors that contribute to the enhanced optical fields around metallic nanostructures required for enhancement[59, 60].

Metallic nanostructures have an absorption described by [1]:

$$A \propto \left|\frac{\partial \mu}{\partial Q} \cdot E\right|^2 = \left|\frac{\partial \mu}{\partial Q}\right|^2 |E|^2 \cos^2 \Theta \qquad [1]$$

where $\frac{\partial \mu}{\partial Q}$ is the derivative of the dipole moment with respect to the normal axis, E is the electric field of the exciting radiation and Θ is the angle between $\frac{\partial \mu}{\partial Q}$ and E. The seminal review of Osawa is followed closely in the following section[61]. The review provides the general trends in optical properties observed for analytes adsorbed on metallic nanoparticles or 'islands' made from coinage metals. The SEIRA enhancement effect is complex with enhancement being dependent on many factors. Research has been carried out over the last two decades to explain how the SEIRA effect enhances infrared absorption but the bulk of SEIRAS literature is recent, little of which is graphene-related. Since the SEIRA effect is not well understood, it is of value in explaining the effect itself. Both molecular and plasmonic mechanism can increase the analytes absorption intensity by affecting the dynamic dipole moment; $\frac{\partial \mu}{\partial Q}$ or the electric field along the dipole moment, E.

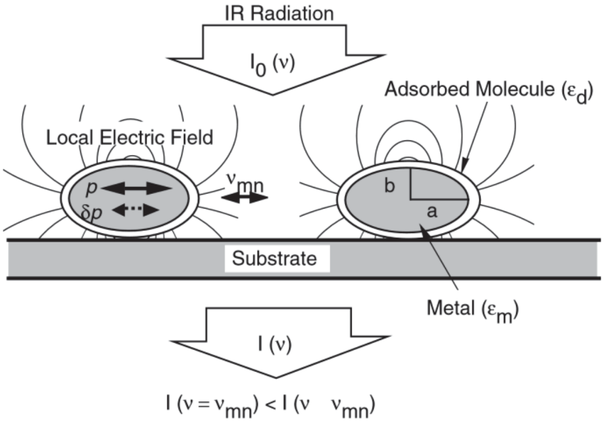

Figure 22: Schematic representation of a metal island films plasmonic contribution to SEIRAS enhancement factors. ε_m is the relative permittivity of the metal and is simulated for bulk silver in section 3.1.1.1. v_{mn} is the radius of the distance between the fields generated by two metal particles. a/b define the axis of aspect ratios. Figure recreated from reference 61.

The nanoparticles or 'islands' used in SEIRAS have a size, shape and proximity dependence to enhancement factors[71-76] *e.g.* significantly smaller than the wavelength of the probing light. Upon radiation of a surface decorated with metallic nanoparticles (figure 22), the intensity of the electric field $|E|^2$ at the surface is not the same as that of the incident photon field: a coupling of the incident photon field to the metal enhances the local field. Close but not touching nanoparticles are also observed to provide the highest enhancement as indicated in figure 22:

$$I\ (v = v_{mn})\ >\ I\ (v\ <\ v_{mn})$$

Maximum analyte absorption intensity requires nanoparticle to be separated, as interactions between particles dampen the local field meaning highly packed nanoparticle films exhibit lower enhancement factors[116-121]. Until now, the polarisation direction of the incoming light,

$I_0(\nu)$, has not be discussed. The oscillations in charge density denoted ‘p’ in figure 22 above, needs to be excited by the incoming light to generate a local electromagnetic field stronger than the incident light around the nanoparticle[62-65]. However, only an electric field with a dipole component perpendicular to the interface can induce a surface charge density fluctuation, δp. The random orientation of nanoparticle dipoles (relative to the analyte) means only p-polarised light has a perpendicular electric field component, so orientations of the nanoparticles local fields are also random (across a scanning window). The roughness of the SEIRAS substrate indicates depolarisation of infrared radiation will occur[111]. In addition to the intensity enhancement, the metal nanostructures strongly confine light to below the diffraction limit, to volumes on the order of 30 cubic nanometers. A recent report (investigating SERS) shows electromagnetic localisation in metal nanostructures is possible even down to the single atom level, generating so-called “picocavities” [66]. Atomic features of a nanostructure are unstable and in an equilibrium between formation and annihilation. These single atomic cavities are capable of enhancements, unlike traditional plasmonics where optomechanical resonators confine light to volumes three orders of magnitude higher using the entire nanostructure. The SEIRAS substrates produced and described in section 3.2 could be probing individual molecular bonds through picocavity fields coupling to the optomechanical resonator (plasmon or phonon). Unlike typical mid-IR spectroscopy, SEIRAS rely on the total local field at the nanostructure dielectric interface rather than the incident field to provide excitation. The intensity of a nanoparticles local EM field decays to zero within tens of nanometers[67]. The sharp decay, and resulting short distance enhancements indicates that the EM fields exhibits near-field coupling.

The local field enhancement can be described by:

$$|E_{local}|^2 \propto \left(\frac{a}{a+b}\right) \qquad [2]$$

where a and b are the radial axis that defines the local radius of curvature of the nanoparticle and E_{local} is the local electric field intensity. The local EM field is polarised along the surface normal to every nanoparticle (figure 22). This model is convenient for explaining the relatively short range enhancement, the role of surface selection rules and explains why particles with a small curvature, *e.g.* needles and rods[68] have been shown to provide the maximum enhancement. The concept here is that metal nanoparticles create a local field much stronger than the incident field, causing a significant enhancement. Close, but not touching, nanoparticles are also observed to provide the highest enhancement as interactions between particles dampen EM fields. In addition to coinage metals, a range of other materials provide plasmonic and phonon enhancement in the mid-IR spectral region[69]. The experimental SEIRAS section in 3.2 below utilises silver nanoparticles produced via the Lee and Meisel method of citrate reduction of silver nitrate[70]. The strong interaction of these silver nanoparticles with light facilitates their use in surface enhancement techniques such as SEIRAS in ambient conditions. Graphene's plasmons have resonance frequencies in the infrared[101]. Figure 23 below shows typical TEM images of the silver nanostructures utilised for enhancement in chapters four and five of this work.

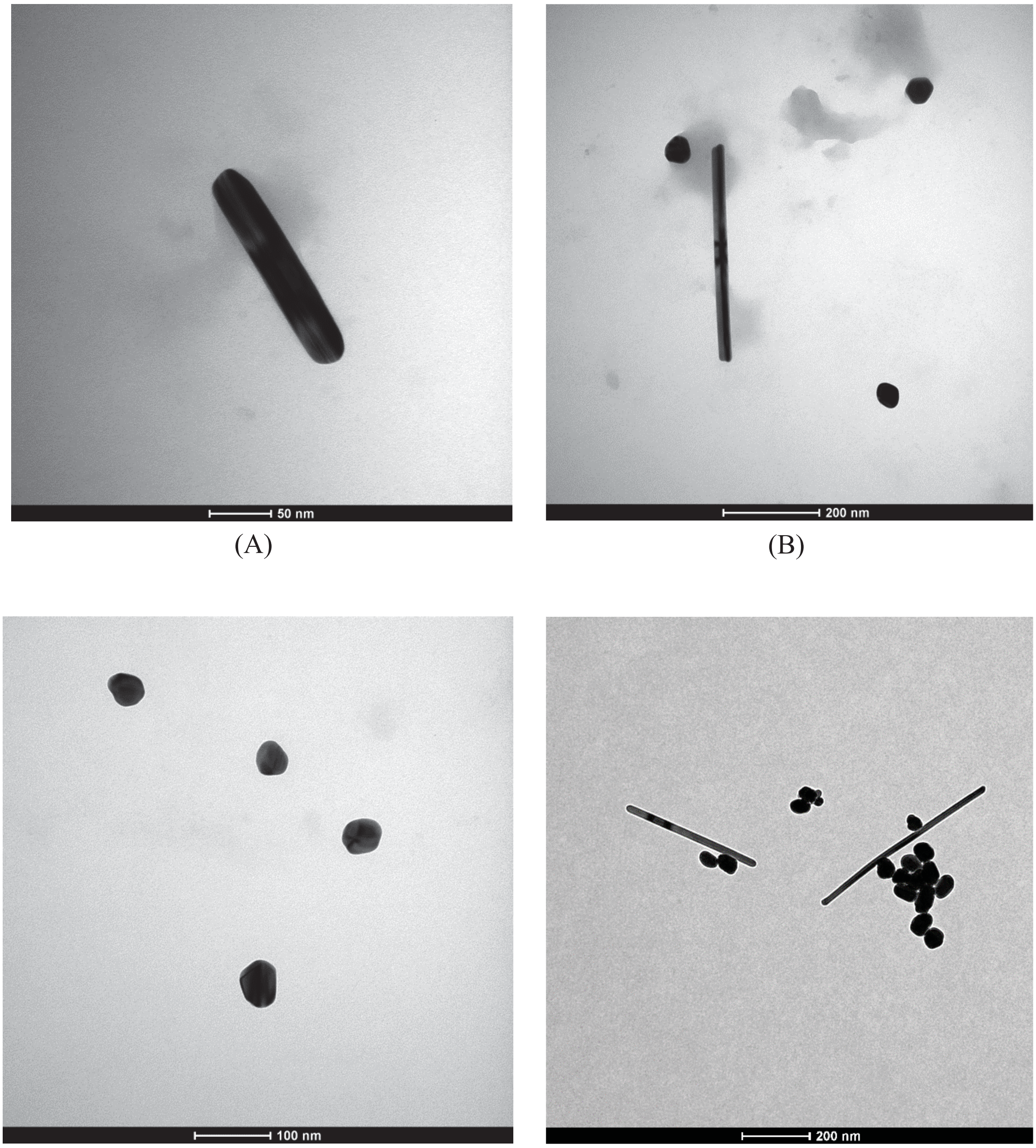

(A) (B)

(C) (D)

Figure 23: Typical TEM images of silver nanoparticles produce by the Lee and Meisel method. Note the different scale bars. (A/B) Short (60 nm) and long (> 300 nm) rods respectively. C/D elliptical nanoparticles of radii 25 - 45 nm and rods of length 400 - 600 nm.

Figure 23 shows typical TEM images of the silver nanoparticles prepared by the Lee and Meisel method. They show a distribution of sizes and geometries, including spheres and ellipses with diameters ranging from 25 - 200 nm and 400 – 600 nm long rods. Preparation of sample for TEM analysis is from sample concentrations and deposition techniques identical to that of SEIRAS substrate preparation. The identical preparation conditions are carried out to provide insight into relative packing and density on a surface. The underlying enhancement mechanisms that may provide the observed enhancement from silver nanoparticles is described in sections 3.1.1 and 3.1.2 below on the plasmonic and molecular mechanisms respectively.

3.2.1 Plasmons

The aim of this section is to give an overview of plasmons and their application to SEIRAS. The emphasis here is on understanding what plasmons are, how they work and why plasmons are a component of what make SEIRAS possible. The field of nanophotonics focuses on light confinement to nanoscale scale dimensions whereby light is confined to dimensions much, much smaller than the wavelength of light through plasmonic mechanisms. The optical response of metals such as silver is a result of free conduction electrons. When incident electromagnetic radiation strikes the surface of a metal, conduction electrons begin to oscillate. These electrons move in a background of fixed positive ions *e.g.* overall neutral. This plasma forms the definition for the term plasmon where the optical response of this plasma determines the optical properties of the metal. The text of Ru(2009)[125] is used to provide definitions where no formal, agreed upon definition is available *e.g.* plasmon.

3.2.1.1 Dielectric Properties of Silver

To model the optical response of a solid-state plasma to electromagnetic radiation, we will use the simplified model, the Drude model. There are two important types of plasmons, which will be discussed based on this model in the remainder of this section: localised plasmons and surface plasmons. The only thing needed to study plasmonic effects in SEIRAS with silver is a knowledge of its optical response described by a dielectric function, ε_m. If these are known, then simply ignoring that the optical response is the result of moving free valence electrons (*e.g.* collective charge oscillations), is possible. When simulated the relative dielectric function, ε_m, plasmons are viewed as electromagnetic modes. The Drude model is used here to provide an understanding of the dielectric function of silver which use the the Lorentz model to describe atomic polarizability. The Lorentz model describes the optical response of an electron in an atom or molecule, bound with a restoring force with a resonant frequency ω_0. The displacement of electrons from equilibrium is such that it undergoes a motion that is governed by the applied electric field (incident light). The resulting forces are modelled as harmonic forces. The system of harmonic oscillators is driven by an applied force due to electromagnetic radiation at a given frequency. The conduction electrons in silver are not bound, meaning they don't have a restoring force so the Lorentz model can be applied (*e.g.* $\omega_0 \approx 0$). The Drude relative dielectric function of a metal can then be obtained by taking $\omega_0 = 0$ in the Lorentz model:

$$\varepsilon_m = 1 - \frac{ne^2}{m\varepsilon_0}\frac{1}{\omega^2 + i\gamma_0\omega} \qquad [1]$$

where n is the number of free electrons per m^3, m is the mass in kg and γ_0 is the damping term in $rad\ s^{-1}$.

[1] is then incorporated into the Drude model which leads to:

$$\varepsilon_m = \varepsilon_\infty \left(1 - \frac{\omega_p^2}{\omega^2 + i\gamma_0\omega}\right) \qquad [2]$$

where $$\omega_\mathrm{p} \left[\frac{\mathrm{rad}}{\mathrm{s}}\right] = \sqrt{\frac{ne^2}{m\varepsilon_0\varepsilon_\infty}}$$

In the absence of an external perturbation, the charge density is uniform and zero, meaning ω_p is the natural oscillation frequency of the free electron plasma (plasmon). Defining the oscillation wavelength as $\lambda_\mathrm{p} = \frac{2\pi c}{\omega_\mathrm{p}}$ and taking the real and imaginary parts of [2] gives:

$$Re\big((\varepsilon_m(\omega)\big) = \varepsilon_\infty \left(1 - \frac{\omega_p^2}{\omega^2 + \gamma_0^2}\right) \text{ and}$$

$$Im\big((\varepsilon_m(\omega)\big) = \frac{\varepsilon_\infty \omega_p^2 \gamma_0}{\omega(\omega^2 + \gamma_0^2}$$

Since the damping factor, γ_0, is small compared to ω, a plasma described by the Drude model has a frequency obtained from the condition $Re(\varepsilon_m\big(\omega_p\big)$ is ≈ 0.

This description, although simplified, is successful in explaining the optical response of real metals as a consequence of the free (conduction) electrons at wavelengths longer than 250 nm, as it does not account for inter-band transitions (UV excitation). The optical properties of bulk silver are simulated (real and imaginary parts of the dielectric function) below and compared to experimentally obtained nanostructured silver.

Figure 24 (A) below shows how the optical properties of metals, or specifically plasmons, change from bulk to nanostructured silver. The experimentally obtained UV-vis absorption of ensemble-averaged silver nanoparticles is compared and contrasted to the simulated permittivity of bulk silver at optical wavelengths using optical constants obtained from Johnson & Christy (1972)[110] and plotted as the individual components of the form:

$$\varepsilon_m = -\varepsilon' + i\varepsilon''$$

The negativity of the real part of ε_m at visible wavelengths is the origin of many optical properties of metals, including plasmons. The imaginary component, ε'', is a measure of energy absorption by plasmons while the real component, ε', is a measure of the plasmons ability to screen electric fields *e.g.* reflect or transmit radiation (negative meaning reflection). Both components are linked to plasmons.

The real and imaginary components for silver are plotted for bulk silver in figure 24 below and contrasted to nanostructured silver. The point here is that optical resonances in nanostructures are not only dependent on silver's properties but geometry as well. Two objects made of the same metal but with different geometries have different resonance conditions.

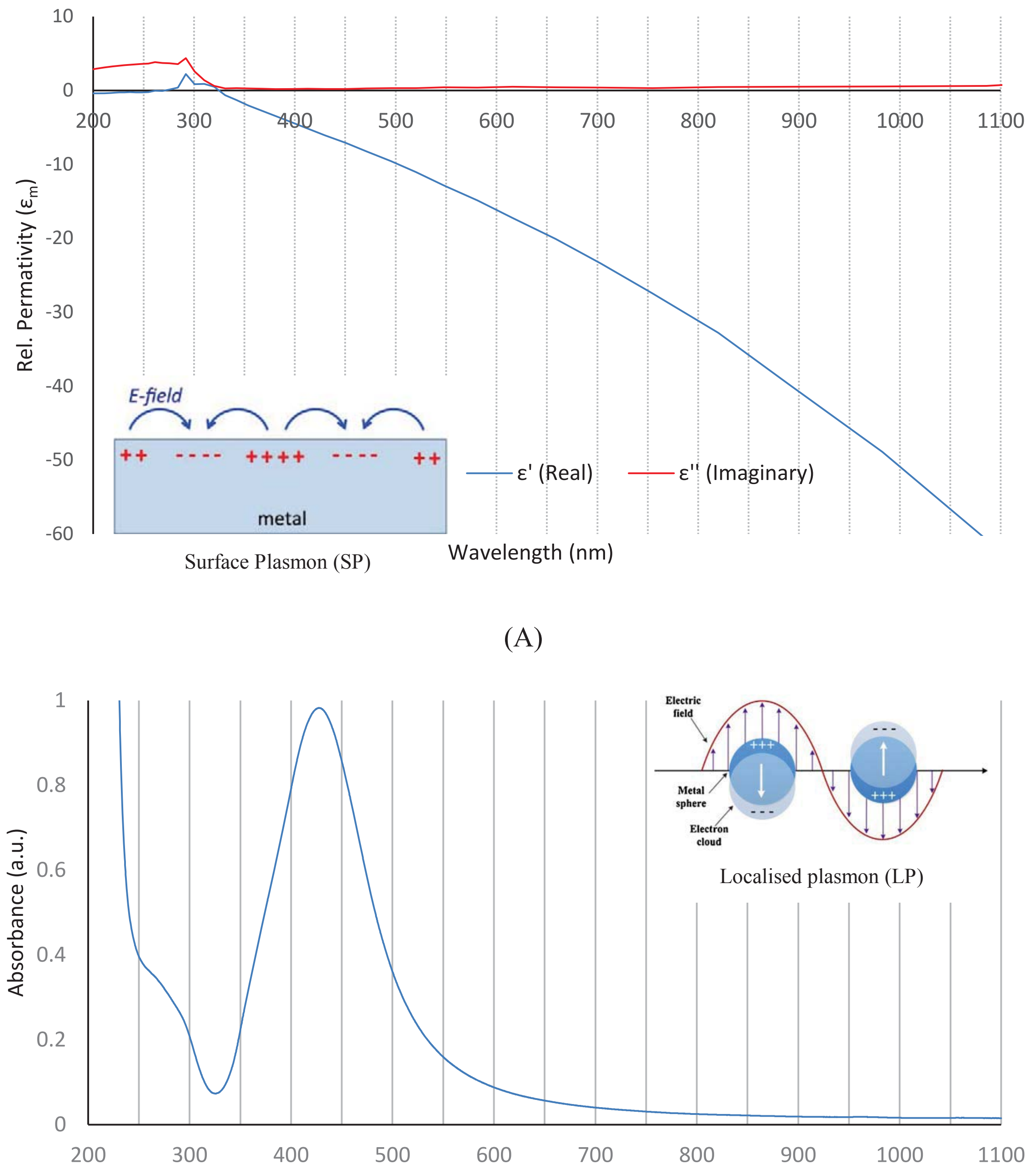

(A)

(B)

Figure 24: A) Real (ε') and imaginary (ε'') components of the dielectric function of bulk silver. Inset surface plasmon schematic and B) UV-vis absorption spectrum of citrate-capped silver nanoparticles produced by the Lee and Miesel method in H_2O. Inset of a surface plasmon resonance © Willets (2007)[124].

The two important types of plasmons here are localised plasmons and surface plasmons. Figure 24 (A) simulates the dielectric function of bulk silver and what we will see is that both the real and imaginary parts are linked plasmons. To understand this, we will consider a small metallic particle is interacting with an applied field. The complex component of the field inside the sphere is then constant and proportional to the incident field, E_0:

$$E_{In} = \frac{3\varepsilon_M}{\varepsilon(\omega) + 2\varepsilon_M} E_0$$

If the numerator approaches zero ($\varepsilon(\omega) \approx -2\varepsilon_M$), which can be met only approximately in real metals, when absorption the imaginary component is close to zero at a wavelength when the real component is $\approx -2\varepsilon_M$. Figure 24 (A) shows the plasmon resonance condition for bulk silver is met at 331.0 nm. The resonance is a surface plasmon and is shown as an insetted schematic. The plasmon is confined to the bulk air-metal interface so is a surface plasmon. Since the real component is dependent on geometry, the wavelength at which resonance occurs changes with particle size.

UV-vis absorption spectra of the silver nanoparticles in figure 24 (B) has the strongest band at 420.0 nm and is attributed to the collective electron resonances of nanoparticles (inset). Since the plasmon is geometrically confined, it is a localised plasmon. The band at 420.0 nm exhibits a resonance weakening towards higher wavelengths as the proportion of larger particles decrease. These excitations, being strongly dependent on the size and shape of the particles, exhibit plasmon resonance at visible wavelengths for small (< 40 nm) nanoparticles and localised plasmons for large (> 100 nm) particles. The silver nanoparticles both absorb and scatter strongly at shorter wavelengths, with absorption weakening towards longer wavelengths, manifesting as a ‘tail’ in figure 24 (B) as intensity decreases up to 1100 nm. The width of this tail is due to the decrease in the proportion of larger particles.

3.2.1.2 Localised Plasmons and Graphene (SEIRAS)

This section focuses specifically on localised Plasmons as contributors to plasmonic enhancement in SEIRAS of graphene on a film of isolated nanoparticles supported by a smooth (IR-reflective) metal copper surface. Localised plasmons in nanostructured metals originate from Mie's solution to Maxwell's classical theory of electrodynamics. The theory describes equations for a plane (evanescent) wave interacting with a spherical surface. The magnitude of a molecules electric field near a nanoparticle’s curved surface (‘Curved' meaning a cavity or a rough ‘inhomogeneous’ island-like film) increases. Localised surface plasmons are the hybrid excitation of free-charge carriers and a plasmon mode, coupled to a nanostructured metal-dielectric interface.

Considering the analogy of localised plasmons is an antenna, a broad spectrum of photons are absorbed over a large spatial area and focused into a smaller volume. The focusing of this light onto an analyte *e.g.* graphene means the light intensity irradiating a sample near the antenna is vastly greater, hence a significant increase in signal intensity is obtained. The nanoparticles transmit an EM field through the dielectric interface at a frequency close to the applied field as a consequence of decay. The transmitted field couples with analytes at the interface, resulting in local field enhancement at the excitation wavelength. The excitation wavelengths of interest here are those comprising the mid-IR spectral region. The confinement of the surface plasmons to the nanoparticle provides plasmons with an extreme sensitivity to features on the surface. This increased sensitivity is the basis for utilising mid-IR radiation to characterise functionality in graphene materials. For nanostructured particles that are much smaller than the incident wavelength, the applied field is uniform across the particle. The electrons inside the structures follow the incoming field and transmit dipole radiation.

3.2.1.3 Phonons as Enhancement Contributors

The optical response of phonons also leads to a negative Re(ε), and a phonon resonance, but the conditions are not satisfied till much longer wavelengths. In this final contributor to the EM mechanism, phonons are considered. In the previous section, plasmons were discussed as an accepted contributor to the EM mechanism. The similarities of plasmons to phonons lead to the question 'can phonons be a potential enhancement contributor?'. Phonons are the collective oscillations of lattice vibrations and have many of the same features as their plasmonic counterparts. The difference being that the optical response is not dictated by free electrons but by phonons – effects which are referred to as phononics. The case here would be the interactions between the plasmons (localised to metallic nanostructures) and phonons (graphene) where mixing would result in a hybridised optical phonon. The literature is scarce on hybrid graphene optical phonon modes as a possible contributor to the EM mechanism, so its occurrence here is conjecture noted in passing for completeness. Optical near-field coupling in the infrared by lattice vibrations (phonons) is a distinct possible enhancement factor intrinsic to graphene materials[100]. At lower frequencies, the surface plasmon's dispersion relation breaks down due to confinement at the interface as the propagation decreases towards the wave vector of the dielectric material. The breakdown is understood experimentally as phonon modes in graphene not being dampened by the substrate[77]. When graphene is on a polarizable substrate such as a supporting reflective substrate, the surface optical phonons may interact with graphene through electronic states in the metal or nanoparticles leading to the possibility of interactions whereby a mixture may result in an hybridised optical phonon consisting of plasmons and phonon modes[78]. Although typically not tunable, phonons are still of interest in graphene literature because they represent a reasonably low-loss, crystal dependent optical response over a small spectral region, *i.e.* exceedingly large enhancement over a small spectral range. Phonons were the final discussion point for possible contributors to the EM mechanism. The following section describes the molecular contribution to enhancement.

3.2.2 Molecular Enhancement Mechanism

The orientation and change in absorption of an analyte as a result of chemisorption onto metal nanoparticles and can provide additional enhancement. The molecular mechanism is a product of a redistribution of electron density due to covalent attachment of an analyte to the interface of metal particles. Molecules chemisorbed on a metal surface show a larger enhancement than do physisorbed molecules suggesting covalent effects between the molecule and surfaces[60]. The molecular mechanism is backed up by evidence of dependency of SEIRA spectra on the molecular geometry of the analyte. Covalent attachment is not required for surface enhancement, however, as confirmed by the presence of enhancement on ATR-FTIR experiments, interactions between the dipoles of adsorbed molecules affects band intensities and positions[79]. Distribution of local optical fields exhibited by the nanoparticles is random. These randomly oriented localised fields have an effect on the vibrational intensities similar to an unbound or free-to-rotate molecule. As a result, the enhancement shows no polarisation dependence.

3.3 Experimental Development of SEIRAS

3.3.1 Attenuated Total Reflectance Accessory

To provide context for the development of the SEIRAS substrates, a background of the original problem is described in this section. During the initial stages of this work, a number of techniques were attempted to characterise graphene flakes. Since covalent functionalisation of graphene was the overall goal, mid-IR FTIR spectroscopy was thought to be the most valuable technique. Figure 25 below shows the FTIR spectrum of a sample of graphene obtained with an ATR accessories by placing dry graphene material onto the germanium crystal.

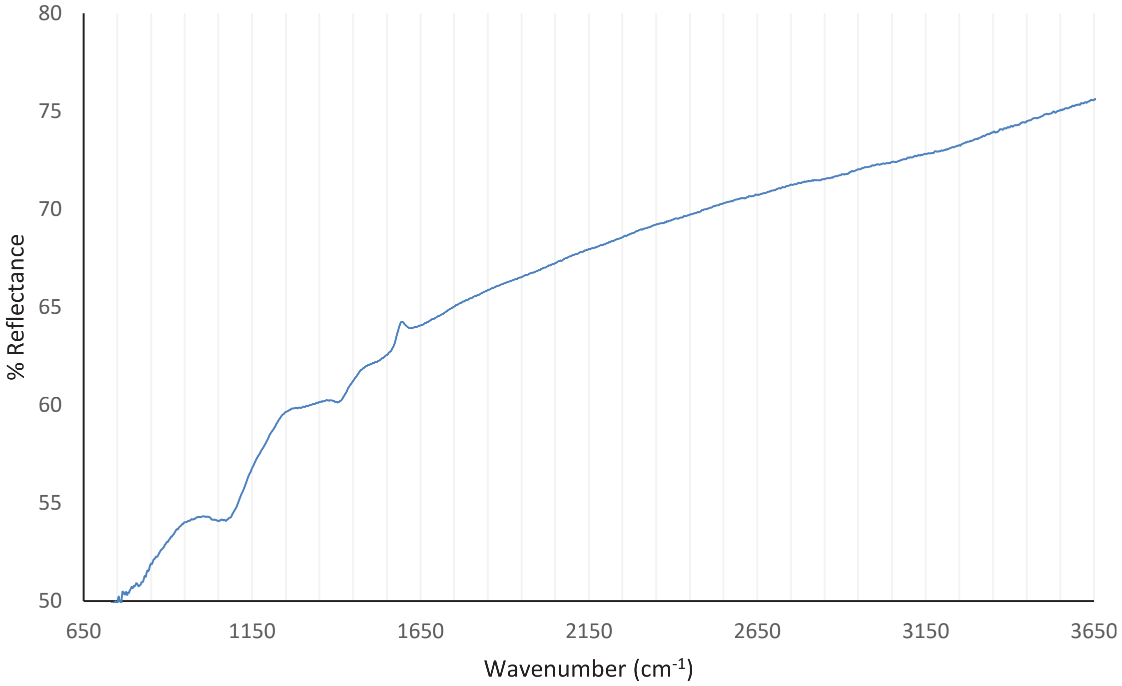

Figure 25: ATR-FTIR mid-IR reflection spectrum of xFlakes over the 650 – 3650 cm^{-1} spectral range.

The mid-IR spectrum of xFlakes in figure 25 above makes it clear that the setup was not sensitive enough to baseline resolve the bands to elucidate information on the functional groups present in the material. Since baseline resolving bands requires the signal-noise ratio to increase, there were two options. Increase the signal intensity or decrease the noise. Because the detector on the other FTIR bench (with an IR-microscope attachment) provides higher sensitivity (lower noise), the IR microscope was used in an attempt to obtain better data. The increased detector sensitivity also, however, lead to a similar problem in spectral detail (see figure 27 below for example). The other approach to increase spectral detail was increasing the signal component of the ratio which is not as easy. The options used a synchrotron, which worked (data not shown) or plasmonics. Since the synchrotron option was not immediately available, inspiration from SERS was obtained. The thinking was that if small nanoparticles provide enhancement at visible wavelengths (SERS), large nanoparticle could provide enhancement at longer wavelengths *e.g.* mid-IR. This logic led to the literature search on infrared enhancement techniques where the SEIRAS technique was discovered and shown to be used mostly in ATR and transmission modes. Since these modes were straight forward to attempt, the development of SEIRAS of graphene started here. Both ATR and transmittance setups ultimately failed because drop casting could not obtain films that covered the ATR crystal (≈ 1 mm^2) at a uniform thickness of less than 10 nm (the literature used vacuum evaporation to coat the germanium ATR crystal).

3.4 Microscope Accessory

Due to lack of success of obtaining SEIRAS with an ATR or transmission mode, it was decided an IR-microscope setup would be the best next option as the focused beam means regions of only ≈ 30 µm were required to be at the required 10 nm thickness. Since neither the ATR or transmittance mode worked, a method using a microscope attachment was developed which, as shown in the following section, worked well, after trial and error.

3.4.1 SEIRAS substrate preparation

Successful preparation of graphene samples for SEIRAS ultimately comes down to sample thickness. Regions irradiated with mid-IR radiation need to be ≤ 10 nm to obtain near-field optical enhancement. Langmuir-Blodgett-based deposition or slow solvent evaporation are used to achieve appropriate sample thickness before AgNP deposition. AgNP concentrations used in sample preparations have a UV-vis absorbance maxima of 0.2. Graphene samples appear pale grey with absorbance maxima ≈ 0.05.

3.4.1.1 Drop-casting

Drop-casting is possible for solvents that disperse graphene, and have a high vapour pressure. This method takes 3 μL of a graphene dispersion (after two hours sonication) and drops it onto the surface. After the solvent has evaporated, many 1 μL drops of AgNPs are placed onto the surface and allowed to dry.

3.4.1.2 Langmuir-Blodgett Deposition

Langmuir-Blodgett (LB) based deposition is useful for materials that disperse in water-insoluble liquids. This method of sample preparation utilises the hydrophobic nature of graphene. AgNPs (50 μL) are pipetted onto the surface of the mid-IR reflective substrate to form a large surface area droplet. Graphene dispersed in a water-soluble solvent *e.g. isopropyl alcohol (IPA)* is then pipetted (≈ 2 μL) on top of the droplet. As IPA dissolves, the graphene crashes out and spreads out across the liquid-air interface to minimise surface area. The droplet is left to evaporate to produce a thin film graphene on top of nanoparticles.

3.4.1.3 Solvent Evaporation

Sample preparation using solvent evaporation has been successful in providing thin films of graphene required for SEIRAS. Self-organisation of the graphene using evaporation as the driving force allows the slow deposition and minimal aggregation of graphene resulting in thin ≈ few nm films of graphene aggregates of approximately 30 x 30 µm. A 2 x 20 mm piece of copper coated silicon wafer (mid-IR reflecting) is placed vertically upright in a 5 x 40 mm glass vial such that the reflective side faces the perimeter. Graphene is dispersed in an organic solvent of high vapour pressure such as THF, IPA or EtOH. Pipetting 3 µL of the sample into the vial draws the sample into the space between the glass wall and substrate. Liquid not held by capillary forces is discarded. The Solvent is allowed to evaporate over 20 minutes before pipetting silver nanoparticles (≈ 3 µL) into the vial and leaving to evaporate onto the prepared graphene sample (≈ 60 minutes).

3.5 SEIRAS in Practice

Graphene sheets absorb 2.3 % of incident white light per layer meaning 50 layers would absorb all incident light and appear black meaning the average thickness is 15 nm. The colour scale from black to light grey is thus used as an indicator of thickness. This intrinsic absorption of graphene may be useful in determining an approximate sample thickness. Bright field image in figure 26 shows a microscope view of the SEIRAS substrate prepared with graphene. Note that the orange discoloration of bright field images below is due to the nanoparticles. The appearance of the graphene sample as grey, as opposed to black, indicates that the sample thickness is on average approximately a few nanometers, consistent with the approximate thickness of samples based on bright field images.

3.5.1 SEIRAS – A Microscopic (Brightfield) View

Figures 26-28 below are bright field images of typical regions of the SEIRAS substrate prepared by the three methodologies above to illustrate problems during the development of the SEIRAS substrate.

3.5.1.1 Drop-Casting

The first method attempted was simple – drop casting. The images below clearly show the lack of potential in this method.

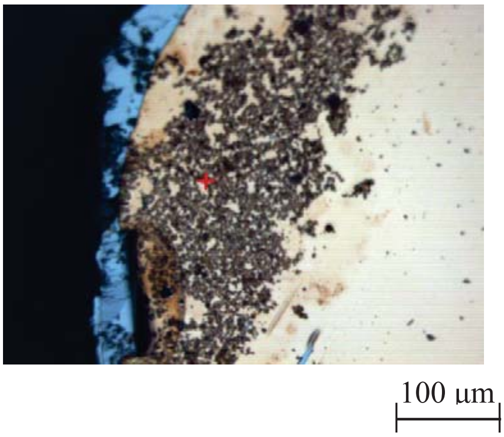

(A)

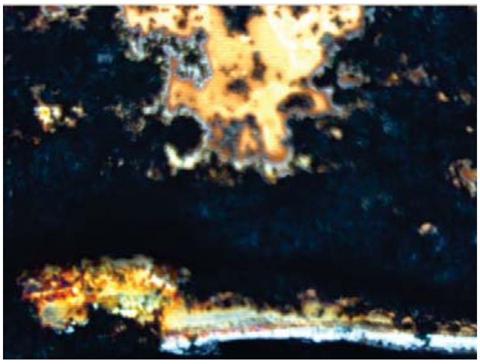

(B)

(C)

Figure 26: A) Thin film of aggregates at the SEIRAS substrate's edges and B) Large cluster of aggregates sitting on the substrate's edge and C) Bright-field image showing the coffee-ring drying effect.

Figure 26 shows the SEIRAS substrate prepared by drop casting. Figure 26 (A/B) shows a small and large amount of aggregates respectively accumulating at the edges of the substrate. These aggregates are far too thick to provide a SEIRAS spectra for the sample. Another problem was the formation of coffee rings where the majority of the material is concentrated as aggregates around the edges. This can be seen in figure 26 (C) above. Coffee rings are a common result of drop casting, and the underlying causes have been reported in literature[122].

3.5.1.2 Langmuir-Blodgett Deposition

The LB deposition method was met with limited success. The relative size distribution decreased compared to the drop-casting method.

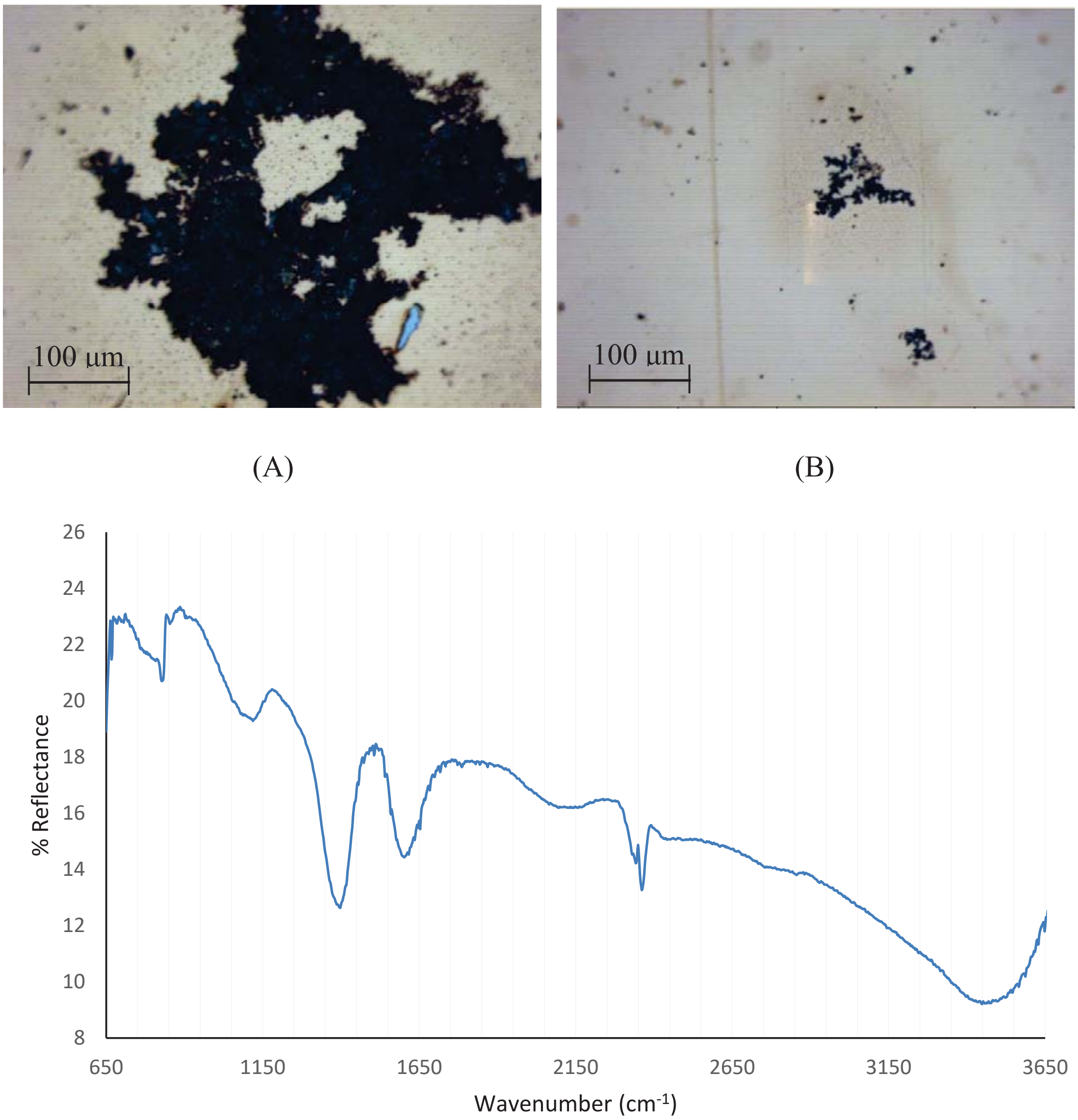

(A) (B)

(C)

Figure 27: A/ B) Large and small aggregates respectively obtained by LB deposition and C) SEIRAS spectra obtained from B. Note the sloping baseline spectral artefact.

Figure 27 (A) is an image of a large aggregate on the SEIRAS substrate prepared by the LB method. The number of aggregates significantly decreased compared to the drop casting method, and no coffee rings were observed. The technique did, however, have dendrimers formed by the nanoparticles (not shown). These have been observed in literature as a drying effect[123]. Figure 27 (B) shows how the nanoparticles appear to have been captured by the aggregate and held by capillary forces. The nanoparticles dry around the aggregates indicating the drying was relatively quick causing viscous drag to occur. A small number of aggregates were almost thin enough to provide maximum SEIRAS enhancement. An example SEIRAS spectra obtained from the substrate prepared by LB deposition can be found in Figure 27 (C). The problem here being the large baseline slope which could be a result of small variations in sample thickness. Since this led to spectral artefacts, and less than optimum enhancement, the slow-solvent evaporation technique was developed as described in section 3.5.3.

3.5.1.3 Slow-Solvent Evaporation

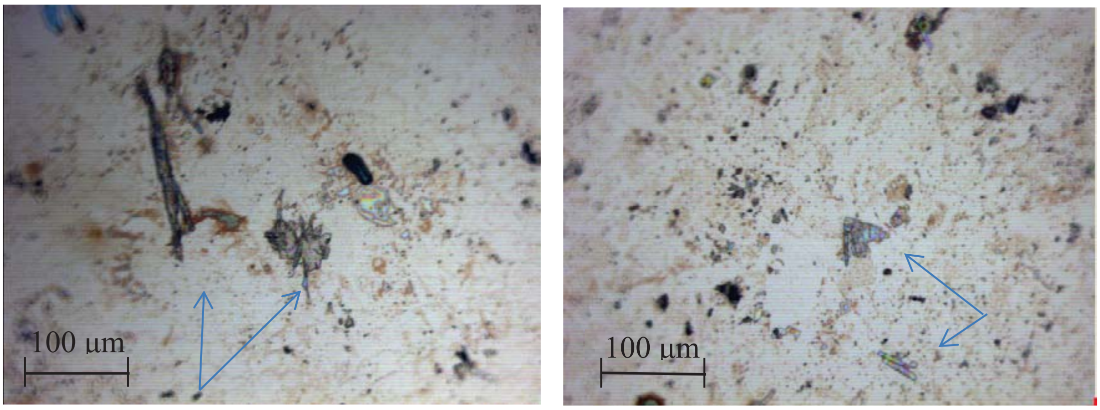

Figure 28: Example Bright field illumination micrograph of SEIRA substrate prepared by solvent evaporation.

Figure 28 above shows a typical SEIRAS substrate prepared by the slow-solvent evaporation method. The sample regions on the SEIRAS substrate are 20 – 80 µm in diameter, and appear grey due to the limited absorption of visible light meaning the samples are on the order of a few nm. The orange background discoloration is a result of nanoparticles, and the rainbow coloured regions are likely the result of optical diffraction effects from nanoparticles. This slow solvent evaporation method is consistent with obtaining the required thickness, so no other methods were trialled, and the substrate characterised further below. This method was likely successful due to the approximately zero viscous drag associated with the deposition. This means that effects such as dendrimers[122] and coffee-rings[123] did not occur as in the other methods. Figure 29 below shows a typical SEIRAS spectra obtained from graphene samples prepared in this manner.

3.5.2.1 Characterisation of the Slow-Solvent Evaporation Substrate

3.5.2.2 SEIRAS vs. Reflection Absorption Spectroscopy

A Nicolet 6700 FT-IR spectrometer with microscope attachment was used to perform absorption measurement in reflection mode. A liquid nitrogen cooled, type-a mercury-cadmium-telluride (MCT-a) detector was used to cover the mid-IR (650 - 3650 cm^{-1}) spectral region in conjunction with a KBr beam splitter. Background spectra were obtained from clean substrate regions immediately before performing measurements, which were carried out at room temperature with a spot size of ≈ 30 x 30 μm.

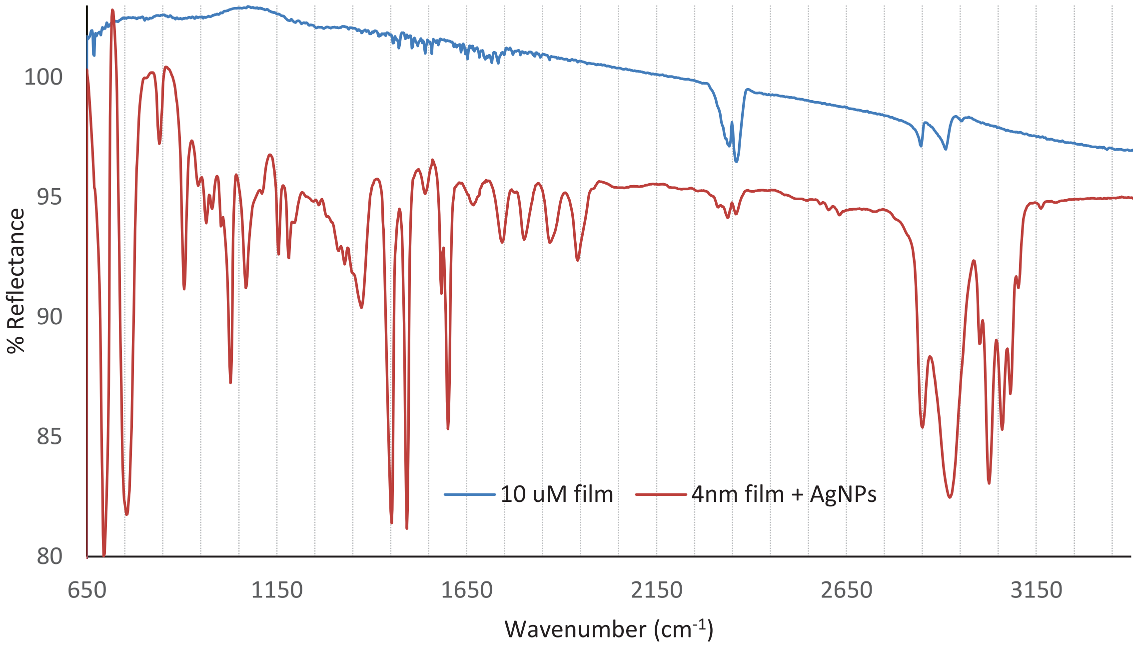

Figure 29: A comparison of the sensing results over the 650 - 3400 cm^{-1} spectral range of a 10 μm thick film without and a 4 nm thick film utilizing AgNP surface enhancement.

Figure 29 shows the mid-IR spectra of graphene as a film (10 µm) and SEIRAS spectra of a 4 nm sample. The figure illustrates the sensitivity problem in the characterisation of graphene materials in the mid-IR by comparing standard reflectance and the enhanced obtained by SEIRAS substrates. The spectral analysis of the SEIRAS spectra is the subject of the next chapter so is not mentioned here further, but the relative comparison is noteworthy. A 4 nm film with nanoparticles provides two orders of magnitude band intensity increase over the reflection spectra of a graphene film without near-field enhancement while being 2500x thinner. The CO_2 band at 2350 cm^{-1} can also be used as an approximate intensity standard *i.e.* SEIRAS spectra bands are 11 x more intense than the CO_2 while the reflection spectra is 0.4 x. This indicates SIERAS spectra bands are 28 x stronger, however, this is only a rough comparison. The success of this substrate preparation method meant no other techniques were trialled, and the substrate was characterised further.

3.5.2.3 Solvent Evaporation - Microscopic (TEM) view

TEM provides images of the graphene samples on the SEIRAS substrate. Preparation of TEM samples mimics the SEIRAS slow-solvent evaporation method described above. TEM substrates are prepared by diffusion deposition of organic solvent dispersed graphene, driven by solvent evaporation and diffusion deposition of silver nanoparticles.

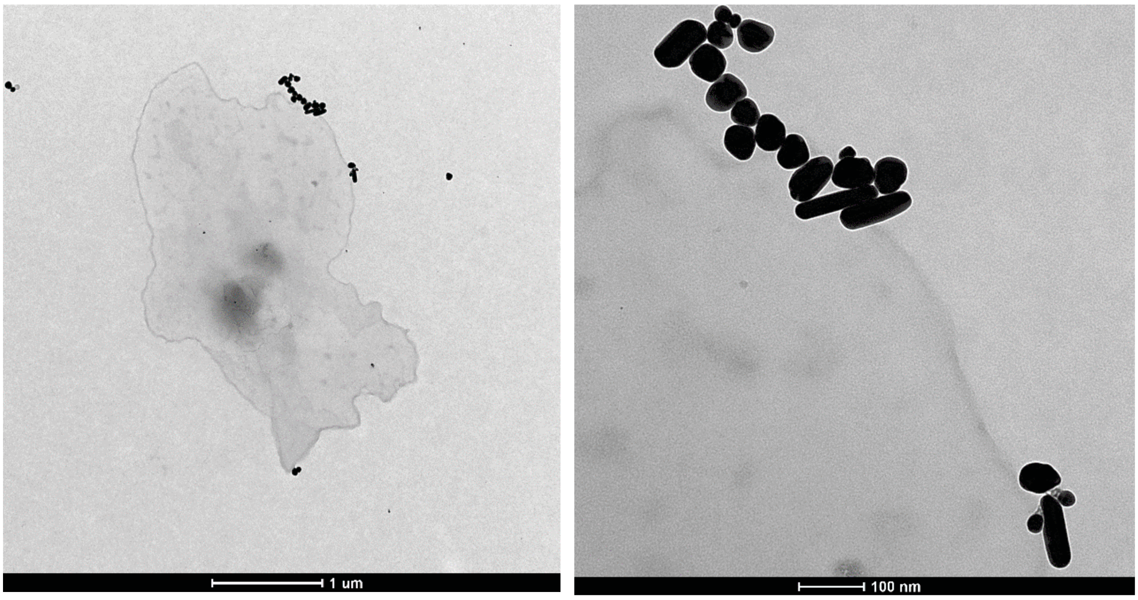

(A) (B)

Figure 30: Tunnelling electron microscopy image of graphene flakes with AgNPs deposited on top showing accumulation at a small region at an edge. A) ≈ 1x1.5 µm flake with 'dotted' 60-100 nm AgNPs and B) Nanoparticle-edge interface zoom showing rod and spherical nanoparticles of varying size (20-150 nm) and geometric (sphere, ellipse and rods) distribution.

Figure 30 above shows a TEM image of a ≈ 1x1.5 µm flake graphene flake with A) AgNPs deposited (via diffusion) on top and B) magnified image of AgNP clustered at edges. The image shows the relatively small number of nanoparticles present which, as discussed in the theoretical section above, is beneficial as large clusters of particles dampen enhancement[116-121]. It is also interesting to note that the rods sit over ≈ 20 nm either side of the edge-basal plane interface. Approximately 10 % of graphene flakes on the surface were similar in nature to figure 30 with nanoparticles sitting on and around graphene while the remaining 90% had no nanoparticles. The low number of graphene flakes with nanoparticle decoration may indicate the lack of a preference of nanoparticles towards graphene *e.g.* random distribution.

3.6 Summary

In summary, SEIRAS is a phenomenon similar in nature to SERS and is characterised by an infrared absorption enhancement of up to three orders of magnitude. SEIRAS was demonstrated and explained with a focus towards graphene materials due to a utilisation of the technique in later chapters. The explanation was focused towards the underlying molecular and plasmonic enhancement mechanisms of SEIRAS before providing experimental insights. The IR-microscope SEIRAS technique presented in this chapter offers a viable tool to characterise functionalised graphene materials with samples being prepared reasonably quickly for high sample throughput. The experiments above have been tailored to attain enhanced optical fields and thereby SEIRAS spectra for graphene materials and to monitor chemical functionalisation of graphene's defects. Challenges for SEIRAS in the future regarding widespread adaptation are the development of lower cost, easily prepared substrate that are also reusable. Addressing these challenges would widen the scope of SEIRAS promoting the development of the technique and application to a wider range of materials. Further understanding of the underlying mechanisms of enhancement, specifically phonon enhancement is of academic interest.

Chapter Four – Graphene's Defects and their Covalent Functionalisation

Background

The production of novel functional materials provides the groundwork for the development of new electronic and photonic devices. The key to providing functionality is in the chemistry. However, a definitive picture of the chemical nature of graphene flakes, and their edges, is largely unclear and debated in the literature. Many models exist for potential edge structure, one being the existence of oxygen-free sites where, among H-terminated edges, are benzene-like armchair sites, and carbene-like zigzag edge types.[80] An argument against this picture is graphene's well-known affinity for heteroatoms that results in terminal edges consisting not of free radicals and carbynes, but aromatic functionalities such as, Ar-COOH, Ar-OH and Ar=O[81]. The challenge with covalent graphene edge chemistry is identifying the functionality where chemical bonding can occur, especially since individual flakes of graphene could contain a range of chemical handles.

The first objective of this chapter is to use SEIRAS to identify the chemical functionality present in native graphene flakes. The second objective is to modify the functional groups with Steglich esterification to add novel functionality. Since the specific functionality and exact proportions depend on a material's origin and chemical pre or post-treatment, literature comparisons are difficult.

The aromatic rings of benzene and its heterocyclic analogues show characteristic bands in the mid-IR. Graphene may contain a large number of functional groups providing multiple overlapping bands. There are, however, distinct bands which can be used to provide insight regarding the chemical environment present in graphene materials.

The literature reports positions and intensities of IR bands that differ based on production method or research group. A description of the most important characteristic frequencies of aromatic rings is given below. Two spectral regions classify the characteristic frequencies. Bands above 1500 cm^{-1} contain mostly stretching modes while the lower frequency range (the ‘finger-print region') includes the modes of the molecule backbone. Aromatic rings also show the C-H absorption around 3030 cm^{-1}, and a number of peaks between the 1450 and 1600 cm^{-1} range due to the aromatic ring stretches. Due to complex ring motions, it is not uncommon to see up to four peaks in this region. Two bands, one at 1500 cm^{-1} and another 1600 cm^{-1} are usually the most intense. Aromatic compounds also show weak absorption bands in the 1650 to 2000 cm^{-1} region that arises from combination and overtones (collectively referred to as summation bands). These are formally known in the literature as the summation bands or informally as ‘benzene fingers’ due to their characteristic shape and appearance in aromatic ring containing-molecules. Strong absorptions are also typical in the 690 to 900 cm^{-1} range due to *out-of-plane (oop)* bending of aromatic C-H bonds. Oop bends are very sensitive to ring substitution pattern and number of substituents as shown in table 2 below.

Substitution Pattern	Frequency (cm^{-1})
Monosubstituted	690-710, 730-770
o-disubstituted	735-770
m-disubstituted	690-710, 810-850
p-disubstituted	810-840
1,2,4-trisubstituted	780-830, 870-900
1,2,3-trisubstituted	670-720, 750-790
1,3,5 trisubstituted	660-700, 830-900

Table 2: Characteristic fundamental absorption frequencies of substituted aromatic rings.

4.0 SEIRAS of Graphene Flakes

4.0.1 xFlakes

Assigning bands in the fingerprint region is difficult, to say the least. The bands in the 900-3500 cm^{-1} spectral region tend to be well-defined and are useful for making assignments of the functionality present in the base flake material so that the appropriate chemistries can be selected to target them. Data obtained from other techniques would be of value in the confirmation of SEIRAS band assignments, although this is no small challenge.

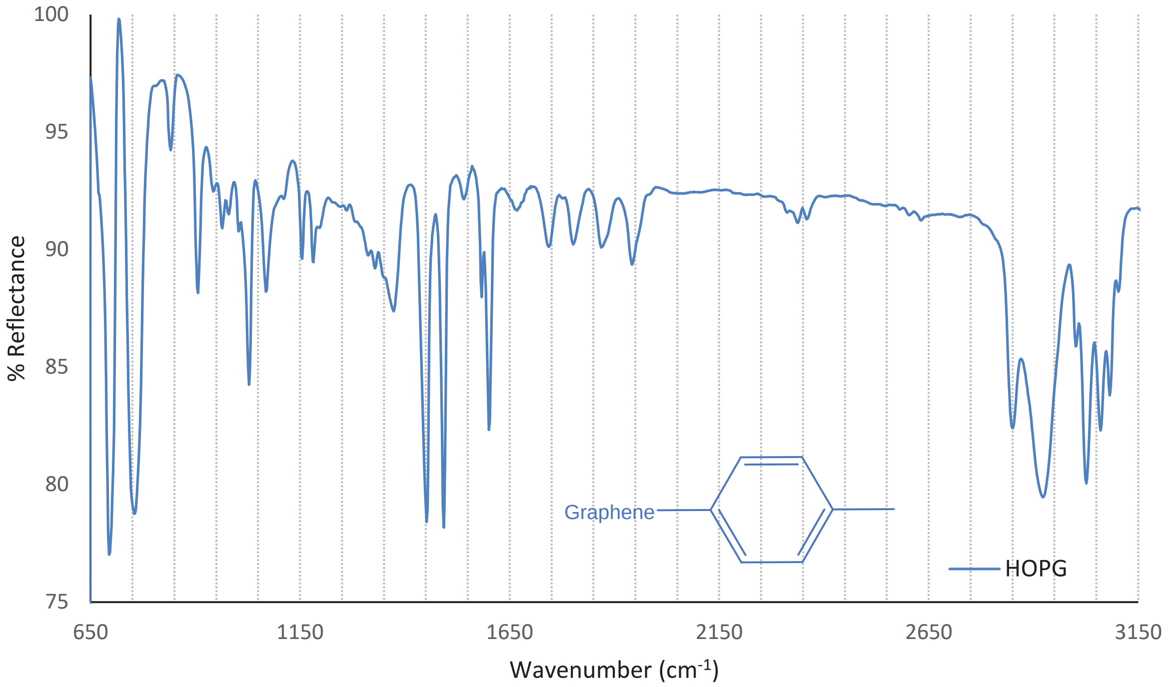

Figure 31: SEIRAS spectra of HOPG, the graphite source used in graphene production, over the 650-3150 cm^{-1} spectral range. Inset of predicted structure.

Figure 31 shows the SEIRAS spectra of ‘powdered HOPG’ e.g. small (≈ 20 μm) flakes of HOPG produced through uneven cleaving or shearing pieces off before dispersion in an organic solvent. The weak features between 1650 and 1940 cm^{-1} are indicative of substituted aromatic rings. Figure 31 above exhibits these 'benzene fingers' with a remarkable similarity to toluene. Bearing in mind the sample has had no contact with toluene; the literature contains a mechanism of CVD growth (HOPG being stacks of CVD graphene sheets) that shows lateral growth of graphene sheets via the formation of methyl groups on aromatic rings[83]. It is not a huge leap to assume that the HOPG which is the starting material for graphene flakes produced in this body of work has edges existing of a significant number of methyl groups; the structure is inset in figure 31 above. An important point to make is that to the best of my knowledge, benzene fingers have not been previously observed in HOPG meaning this is the first IR spectra of HOPG that exhibits these features.

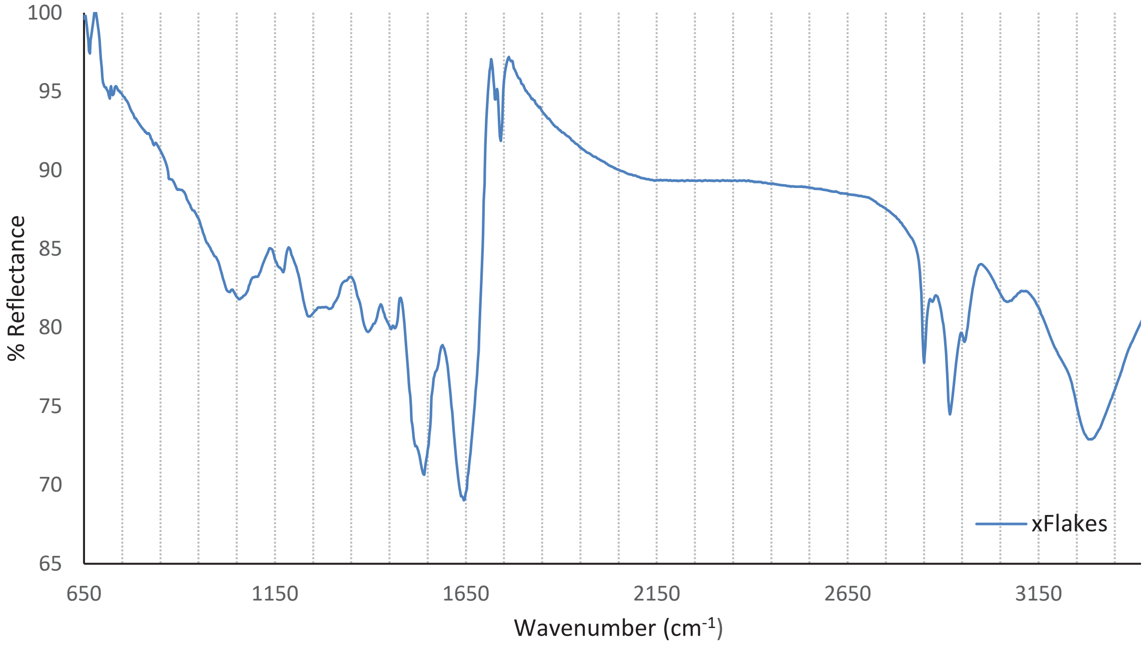

Figure 32: SEIRAS spectra of xFlakes over the 650 - 3450 cm^{-1} spectral range.

The SEIRA spectrum of an xFlake sample is shown in figure 32. This spectrum is consistent between batches of graphene, indicating good reproducibility. The spectra exhibit an OH stretch at 3270 cm^{-1}, and aromatic/aliphatic CH stretches between 2920 and 3060 cm^{-1}. The sharp band with a weaker shoulder around 1740 cm^{-1} is assigned to a C=O stretch which could indicate the presence of carboxylic acids (or possibly ketones or aldehydes) in this material. The most intense band at 1650 cm^{-1} is assigned to a C=C stretch. The discussion of the asymmetric shape of this band is given below. The bands within the fundamental region up to 1530 cm^{-1} are attributed to oxygen-containing functional groups. The broad, obscured nature of this region makes assignments difficult. However, 1380, and 1440 cm^{-1} are possibly due to the bending modes of tertiary alcohols. xFlake's edge structure appears to closely resemble the model proposed by Peralta-Inga[81] *i.e.* edges are saturated mostly with oxygen functionality as opposed to being dangling bonds or hydrogen saturated. A summary of these bands can be found in table 3 below.

Band assignment (xFlakes)	**Frequency (cm^{-1})**	**Type**
Carb. Acid/ Alcohol (OH)	3270	Broad, medium
Ar/aliphatic (CHx)	2920 - 3060	Sharp, medium
(C=O)**H**	2850	Weak, broad
Ketone (Aldehyde)	1744/1726	Sharp, weak
C=C	1650	Stetch, Asymmetric/bipolar
Tertiary alcohol	1394	Bend
Epoxide	1230	Shoulder

Table 3: Summary of xFlakes SEIRA spectra absorption frequencies and assignments.

The SEIRA spectra of xFlakes above contain a somewhat unusual spectral feature around 1650 cm^{-1}. While this asymmetric or ‘derivative-like’ Fano-type band shape may appear unusual but is not uncommon in SEIRA spectra[82]. Recalling Fano’s theory from chapter one, the asymmetric band shape around 1650 cm^{-1} in figure 32 above can be fit to a Fano line shape of the form[29]:

$$C\,\frac{[q\gamma+(E-E_{\Omega})]^2}{(E-E_{\Omega})^2+\gamma^2}$$

where C, q, E_{Ω} and γ are fitting parameters.

These asymmetric bands in SEIRAS spectra are indicative of a highly localised surface absorption of free carriers[82] or a Fano interference between coupled G mode-phonons and plasmons[84].

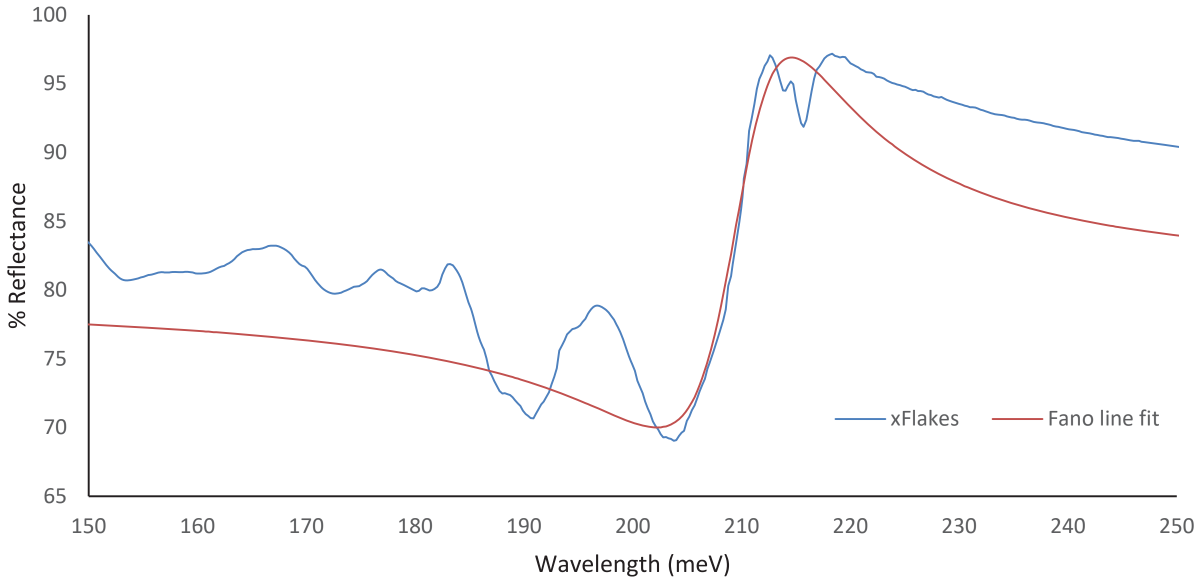

Figure 33: SEIRA spectrum of xFlakes over the 150-250 meV spectral range with a Fano line fit to the asymmetric band shape.

Figure 33 above fits the Fano line shape to the asymmetric band shape with q, E_Ω and γ being 1.3, 210 meV and 6 meV respectively. The line shape fits the resonance well where a q value of 1.3 indicates the phonon contribution is slightly higher than the electron contribution to the mixed state.

4.0.2 GN-Flakes

Graphene produced by graphite nanotomy (GN-Flakes) are almost free of basal plane defects, so any functionality is most likely located at the edges. Saturating edge atoms with oxygen increases the stability of edge states and enhances the adsorption of polar molecules[85]. With this in mind, it would appear that the small sharp peaks around 1600 – 1650 cm^{-1} are the ro-vibrational absorption bands of intercalated water. It is also interesting to note that a significant component of the band which was assigned above as C=C stretching modes (a reasonable assignment), could be intercalated H_2O. These assignments could be differentiated by replacing H_2O with D_2O throughout the sample preparation procedure and monitoring whether the band shifts by a factor of 1.37 (H/D mass ratio)[86].

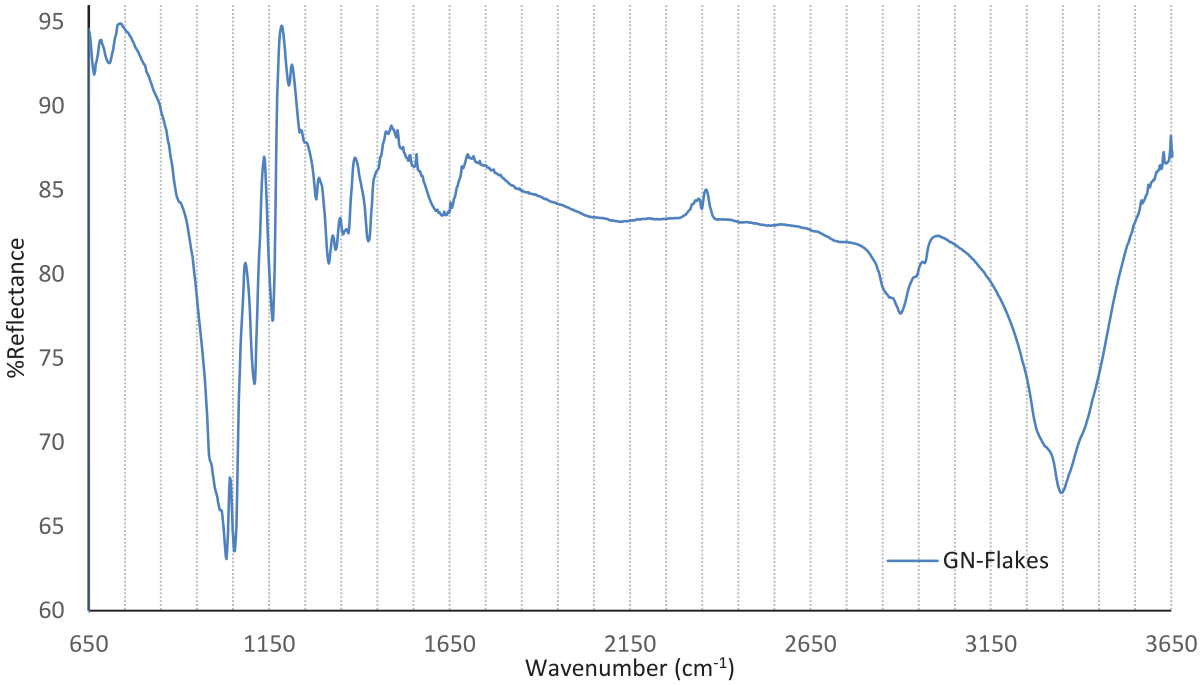

Figure 34: SEIRA spectra of GN-Flakes over the 650-3650 cm^{-1} spectral region.

The most intense bands appear in the fingerprint region at 1034 and 1060 cm^{-1}. The literature often assigns these bands as epoxide, but there is a debate as to if this is a correct assignment, so it is with this in mind that table 4 below cites this as an epoxide. Assignment of the fingerprint region band at 1370 cm^{-1} is to bending modes of tertiary alcohols[87, 88]. 1424 cm^{-1} is assigned to deformation modes of an hydroxyl H-bonding to heteroatoms of other hydroxyls or epoxides respectively[89]. The presence of oxygen functionality means the Peralta-Inga model[81] type edge structure model best describes this material *i.e.* oxygen-containing functional groups terminate edges.

Band assignment (GN-Flakes)	**Frequency (cm^{-1})**	**Type**
OH	3350	Broad (H-bonding)
NH	3280	Sharp, shoulder
Ar/aliphatic –CH	2850-2950	Broad (overlapping)
C=C	1630	broad
H-Bonding	1424	See discussion
Tertiary-OH	1370	Strong
Unknown	1040	See discussion
Mono-sub Ar. Ring	665/705	weak
Epoxy ring	1034/1060	Disputable assignment*

Table 4: Summary of GN-Flakes SEIRA spectra absorption frequencies and assignments. * see discussion

4.1 Covalent Modifications

Section 4.1 describes the chemical procedures carried out on the graphene materials. The chemical modification procedures described below were applied to both GN-Flakes and xFlakes and are collectively referred to as ‘graphene flakes’ in the functionalisation protocol. It is important to note that graphene has a range of oxygen functionality. The chemical targets of the Steglich esterification sections below are only guidelines as graphene may have reactive functionality other than those ascertained from figures 32 and 34 above.

4.1.1 Reduction

The literature has no popular, widely used reducing agent for graphene. $LiAlH_4$ and $NaBH_4$ are, however, known to be effective[90]. The difference in reactivity of these reducing agents is well understood. $LiAlH_4$ is capable the unselective reduction of carbonyl, esters, carboxylic acids and epoxy functional groups to alcohols. $NaBH_4$ is selective towards the reduction of aldehydes and ketones to alcohols.

4.1.1.1 Lithium Aluminium Hydride ($LiAlH_4$)

$$\text{Graphene-OR} \xrightarrow{LiAlH_4} \text{Graphene-OH}$$

Figure 35: Scheme 2. Chemical reaction of the reduction of graphene over $LiAlH_4$

Graphene flakes (10.0 mg) were dispersed in THF to give a 1 mg/ml colloidal suspension. The black solution was sonicated at 1200 W for 3 hours. $LiAlH_4$ (21.0 mg) was dispersed in THF, and the grey solution was added drop-wise to the dispersed xFlakes over 20 minutes. The resulting solution was purged with argon and sonicated at 1200 W for 24 hours. The solution was quenched with 1.5 ml of water added drop-wise, before an addition of 1ml HCl (2 mol/L). The material was then washed with 3:87:10 HCl: THF: water seven times, three times with a 70:30 THF: water, and eight times with 100% THF. Residual solvent was removed under high vacuum line overnight to obtain black solid; *xFlake-LiAlH*$_4$

4.1.1.2 Sodium Borohydride ($NaBH_4$)

$$\text{Graphene-OR} \xrightarrow{NaBH_4} \text{Graphene-OH}$$

Figure 36: Scheme 3. Chemical reaction of the reduction of graphene over $NaBH_4$

Graphene flakes (20.0 mg) was dispersed in THF to give a 1.0 mg/ml colloidal suspension. The black solution was sonicated at 1200 W for 3 hours. $NaBH_4$ (20.0 mg) was dispersed in THF, and the solution was added drop-wise to the dispersed xFlakes over 20 minutes. The solution was sonicated at 1200 W for 24 hours before the reaction was quenched. The solution was acidified with 0.1 ml H_2SO_4 (2 mol/L) to decompose remaining starting material, then neutralised by washing with a 90:10 THF: $NaHCO_3$ mixture four times. The black solid was then washed with 80:20 THF: water four times and 13 times with 100% THF. Residual solvent was removed under high vacuum overnight to obtain black solid; xFLake-$NaBH_4$.

4.1.2 Steglich Esterification

The Steglich esterification reaction is the primary graphene functionalisation tool. It is mild while allowing the smooth and selective conversion of sterically demanding acid-labile functional groups. It is well known in the literature to be straight-forward and successful for reactions between carboxylic acids and amines with N,N'-Dicyclohexylcarbodiimide (DCC) or alcohols when DCC is used in conjunction with 4-dimethylaminopyridine (DMAP)[91]. Formation of esters requires the use of DMAP to suppress side reactions. With amines, the reaction proceeds to amides without the use of DMAP as amines are more nucleophilic than alcohols. Alcohols are less nucleophilic than amines, and a side-reaction occurs because of the slower esterification. This result in the formation of inactive diimides at edges. Figure 33 below shows the generalised Steglich esterification reaction schematic.

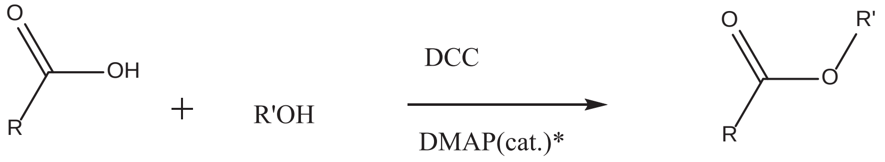

Figure 37: Scheme 4. General reaction scheme of Steglich carboxylate-alcohol esterification reaction. DMAP = 4-dimethylaminopyridine. *Amines can replace alcohols for which DMAP is not required.

4.1.2.1 Sulfanilic Acid

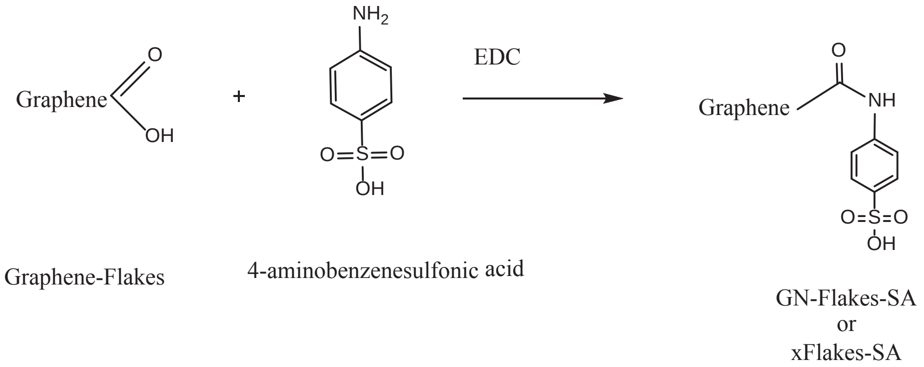

Figure 38: Scheme 5. Coupling reaction between amines on Sulfanilic acid and carboxylates on graphene through an amide forming Steglich esterification reaction.

Graphene flakes were dispersed in THF to give a 0.5 mg/ml colloidal suspension. The black solution was sonicated at 1200 W for three hours. DCC (4.0 mg, 8.7 mol%) and *Sulfanilic acid* (*SA*, 2.0 mg) was dissolved in DMF (0.6 ml) and added to dispersed graphene flake solutions, and sonicated for 24 hours before being washed with DMF and THF three times through centrifugation to separate the solid. Residual solvent was removed under vacuum to obtain black solids; *xFlake-SA and GN-Flake-SA.*

4.1.2.2 4-Nitrobenzoic acid

Graphene flakes were dispersed in THF to give a 0.5 mg/ml colloidal suspension. The black solution was sonicated at 1200 W for three hours. DMAP (0.5 mg), DCC (4.0 mg, 8.7 mol%) and *4-nitrobenzoicacid (NBA*, 2.0 mg) were dissolved in DMF (0.6 ml) and added to dispersed graphene flake solutions and sonicated for 24 hours before being washed with DMF and THF three times using centrifugation to separated solid. Residual solvent was removed under vacuum to obtain black solids; *xFlake-NBA and GN-Flake-NBA.*

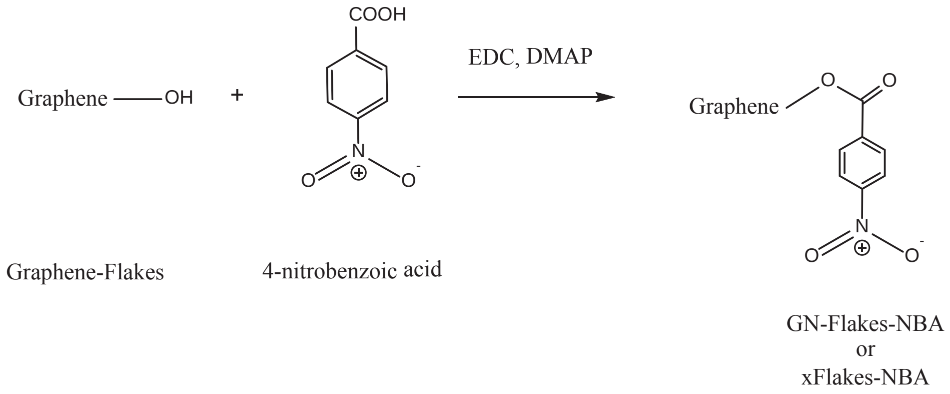

Figure 39: Scheme 6. Coupling reaction between carboxylates on 4-nitrobenzoic acid and alcohols on graphene through an ester forming Steglich esterification reaction.

4.1.2.3 4-Nitroaniline

Graphene flakes were dispersed in DMF to give a 0.5 mg/ml colloidal suspension. The black solutions were sonicated at 1200 W for three hours. DCC (4.0 mg, 8.7 mol%) and *4-Nitroaniline (NA*, 2.0 mg) were dissolved in DMF (0.6 ml) and added to dispersed graphene flake solutions, and sonicated for 24 hours before being washed with DMF and THF three times using centrifugation to separated solids. Residual solvent was removed under vacuum to obtain black solids; *xFlake-NA and GN-Flake-NA.*

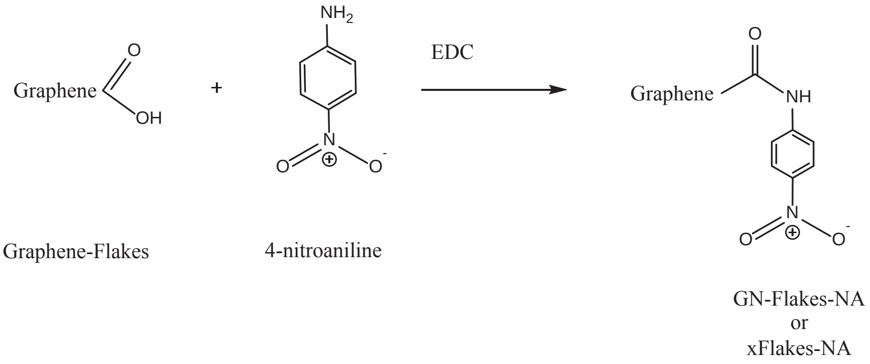

Figure 40: Scheme 7. Coupling reaction between amines on 4-nitroaniline and carboxylates on graphene through an amide forming Steglich esterification reaction.

4.1.2.4 Ethylenediamine

Graphene flakes were dispersed in DMF to give a 0.5 mg/ml colloidal suspension. The black solutions were sonicated at 1200 W for three hours. DCC (4.0 mg, 8.7 mol%) and *1,2 Ethylenediamine (ED,* 20 μL) were added to dispersed graphene flake solutions and sonicated for 24 hours before being washed with DMF and THF three times using centrifugation to separate solids. Residual solvent was removed under vacuum to obtain black solids; *xFlake-ED and GN-Flake-ED.*

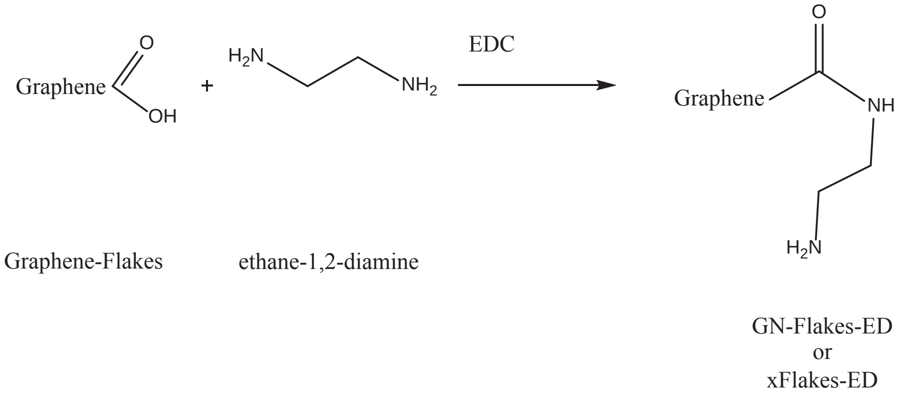

Figure 41: Scheme 8. Coupling reaction between amines on 1,2-Ethylenediamine and carboxylates on graphene through an amide forming Steglich esterification reaction.

4.1.3 Reductive Amination

GN-Flakes-ED and xFlakes-ED were further functionalised with a ferrocencarboxaldehyde-derivative by an ester forming reductive amination for electrochemical applications as described later in section 4.3.

4.1.3.1 Ferrocencarboxaldehyde

xFlakes were dispersed in MeOH (0.6 ml) to give a 0.5 mg/ml colloidal suspension. The black solutions were dispersed at 1200 W for three hours. 20 μL of a 1 mg/ml solution of the

Ferrocencarboxaldehyde derivative was added and the mixture sonicated for 3 hours at rt. 1.6 eq $NaBH_4$ was added and allowed to sonicate for 30 minutes before being washed with DMF and THF three times each respectively, using centrifugation to separated solids. Residual solvent was removed under vacuum to a obtain black solid; xFlake-ED-Fe.

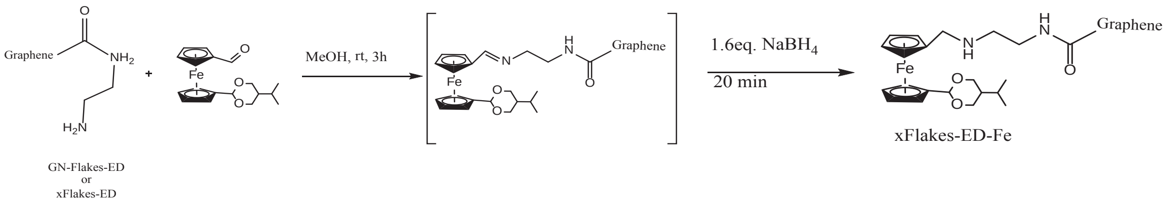

Figure 42: Scheme 9. Coupling reaction between amines on graphene and aldehydes on a Ferrocencarboxaldehyde derivative via a reductive amination reaction.

4.2 SEIRAS of Functionalised Graphene Materials

This section presents the SEIRAS spectra of the materials functionalised with novel reagents as described above in 4.1. SEIRAS spectra of the materials functionalised by reduction or the Steglich esterification method are shown below. The IR data is used to confirm the presence of a functional group, e.g., nitro, sulphate or amine but cannot confirm the specific manner in which these groups are attached to graphene *e.g.* At basal or edge planes via covalent or non-covalent functionalisation. SEIRAS spectra can appear complex, but one thing is clear - the functional group is typically unique to a small frequency range regardless of how the reagent containing the functional group is attached. Reference mid-IR spectra of reactants were obtained by ATR-FTIR. The first section below explores the chemical effect of reducing xFlakes with $NaBH_4$ and $LiAlH_4$.

4.2.1 Reduction

4.2.1.1 NaBH$_4$

Figure 43: SEIRAS spectra of xFlake-NaBH$_4$ over the 900 - 3500cm^{-1} spectral range. xFlakes overlaid for comparison. Spectra offset for clarity.

Upon reduction with NaBH$_4$ (xFlake-NaBH$_4$), some spectral features disappear, and others appear. Bands at 1110 and 1350 cm^{-1} corresponding to the C-OH vibrations manifest. Also, bands corresponding to epoxides around 1222 cm^{-1} are absent, presumably due to their reduction to C-OH. The peak at 1790 cm^{-1} corresponds to C=O based on the sharp and weak spectral feature it exhibits. The slightly higher wavenumber than its unreduced counterpart indicates the ketone is conjugated. This spectrum also shows a decrease in relative intensity for the hydroxyl band at 3500 cm^{-1}. The decrease in aliphatic CH stretches could indicate the presence of unsaturated bonds conjugated to ketone functional groups. This assumption seems bizarre as no observation of increased CH bands is seen. The feature at 2420 cm^{-1} (2350 cm^{-1} is CO_2) is currently unknown but is of interest as it could be a summation band which would allow for easy identification of the functionality and possible explanation of fundamental stretches. The fundamentals for the summation band cannot be assigned with confidence due to bands being obscured.

Band Assignment (xFlake-NaBH$_4$)	**Frequency (cm^{-1})**	**Type**
OH	3470	Weak, broad
Ar/aliphatic (CH)	2860-2920	Weak
Summation?	2440	Weak
C=O	1790	Weak, sharp
C=C	1610-1670	medium, broad
C-O(H)	1350	Strong, sharp
C-O	1110	Medium, sharp

Table 5: Summary of GN-Flake-NaBH$_4$ SEIRA spectra band assignments.

4.2.1.2 $LiAlH_4$

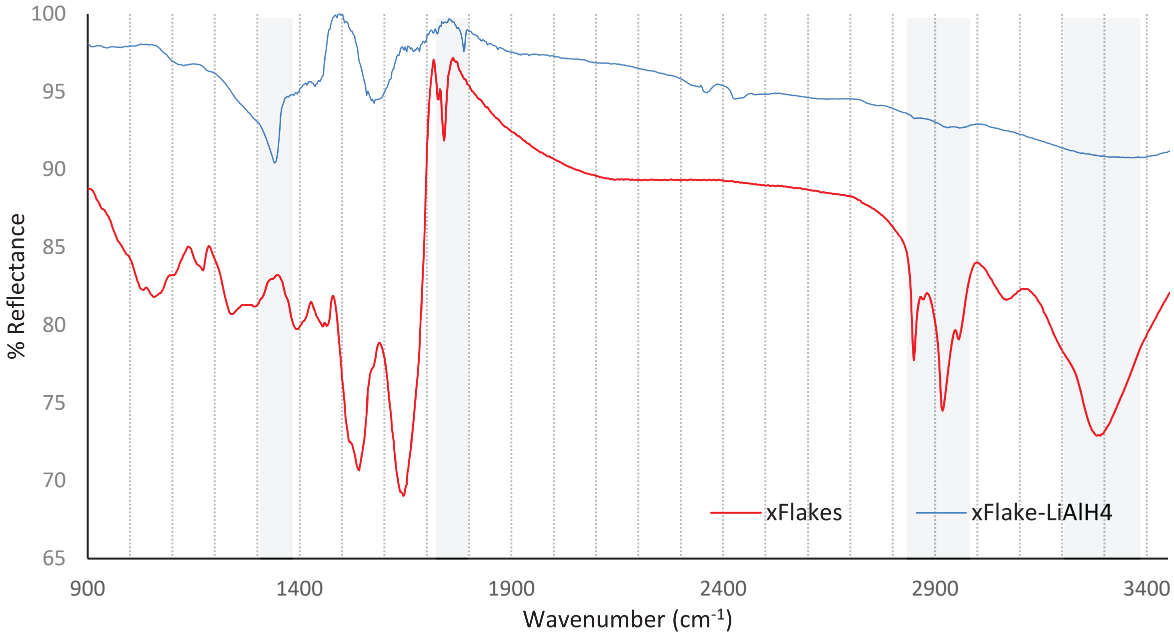

Figure 44: SEIRAS spectra of xFlakes-$LiAlH_4$ over the 900 – 3500 cm^{-1} spectral region. xFlakes overlain for comparison and offset for clarity.

Initial observations of figure 44 above of xFlake-$LiAlH_4$ are that the baseline is sloped and many bands have disappeared, and others appeared. The spectra exhibit similar bands such as the OH at 3330 cm^{-1}, a ketone at 1790 cm^{-1}, and also shows a stretch at 1690 cm^{-1} which may be from the reduction to a different ketone containing functionality. Assignment of the 1580 cm^{-1} band is to the C=C stretch. The major effects exhibited between the two reducing agents is the appearance of only one strong band in the fundamental region at 1340 cm^{-1} and 1420 cm^{-1} assigned to tertiary alcohols. $LiAlH_4$ reduced graphene also exhibits this band, but it is much broader and overlaps with other bands. This may be a result of the different reducing power of the two reagents. Sharp and weak spectral features around 1680 cm^{-1} indicate the presence of water.

Band assignment (xFlakes-LiAlH$_4$)	**Frequency (cm^{-1})**	**Type**
OH	3330	Broad/weak
Ar/aliphatic –CH	2850-2970	shoulder
Summation?	2420	broad/weak
C=O (Conjugated)	1790	Sharp/weak
C=C	1580	broad
C-OH	1340	Broad

Table 6: xFlakes-LiAlH$_4$ SEIRAS spectra absorption frequencies assignments.

4.2.2 Steglich Esterification

4.2.2.1 Sulfanilic Acid

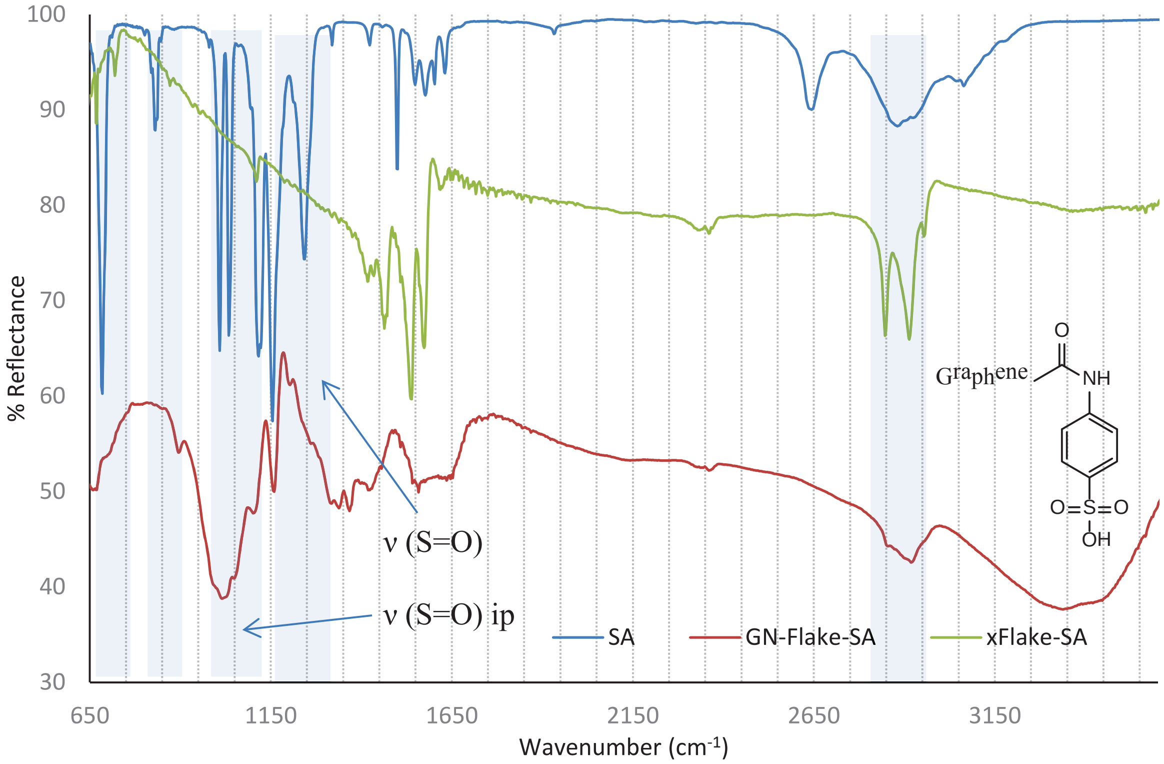

Figure 45: Reflection absorption spectra of sulfanilic acid and SEIRA spectra of GN-Flake-SA and xFlake-SA over the 650-3650 cm^{-1} spectral range. Inset of expected edge structure of GN-Flake-SA and xFlake-SA. Spectra offset for clarity.

Figure 45 above shows the SEIRAS spectra of sulfanilic acid and SEIRAS spectra of GN-Flake-SA and xFlake-SA. Sulfonic acid shows two characteristic band stretches for S=O. The ip stretch appears in the 1025-1085 cm^{-1} region, while the oop appears between 1120-1230 cm^{-1}. xFlake-SA exhibits a weak band in the region where the in-phase stretch is expected but does not show on where the out of phase is expected. It does, however, show a weak, sharp band at 1620 cm^{-1} which is indicative of a ketone (expected for an ester). GN-Flake-SA shows strong bands in the regions where the ip and oop S=O are supposed to be observed. Both SA functionalised graphene flakes show CH_x, but these cannot be used. The 650-900 cm^{-1} region exhibits bands in similar regions in all three materials, but their assignments are not known.

4.2.2.2 4-Nitrobenzoic acid

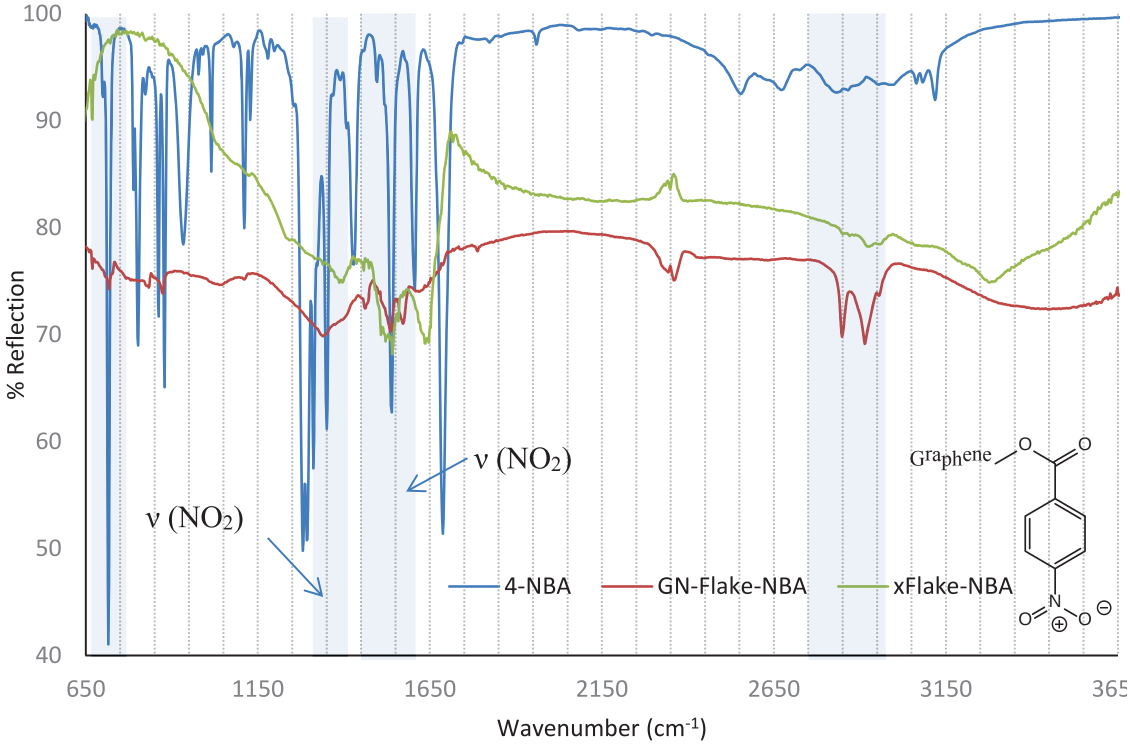

Figure 46: Reflection absorption spectra of 4-Nitrobenzoic acid and SEIRA spectra of GN-flake-NBA and xFlake-NBA over the 650-3650 cm^{-1} spectral range. Inset of expected edge structure of GN-Flake-NBA and xFlake-NBA. Spectra offset for clarity.

Figure 46 above shows the SEIRAS spectra of GN-Flake-NBA and xFlake-NBA. Aromatic nitro functional groups show characteristics for the in-phase and out of phase N=O stretch at 1320-1400 cm^{-1} and 1485-1555 cm^{-1} respectively. Both GN-Flake-NBA and xFlake-NBA have broad bands in these spectral regions, meaning they are possibly obscured by other bands. The 650-700 cm-1 region shows similar band positions as in the reference NBA spectra, indicating a similar substitution pattern of the functionalised materials. Both functionalised materials also show typical CH_x, but these cannot be used to identify the presence of the introduced 4-NBA.

4.2.2.3 4-Nitroaniline

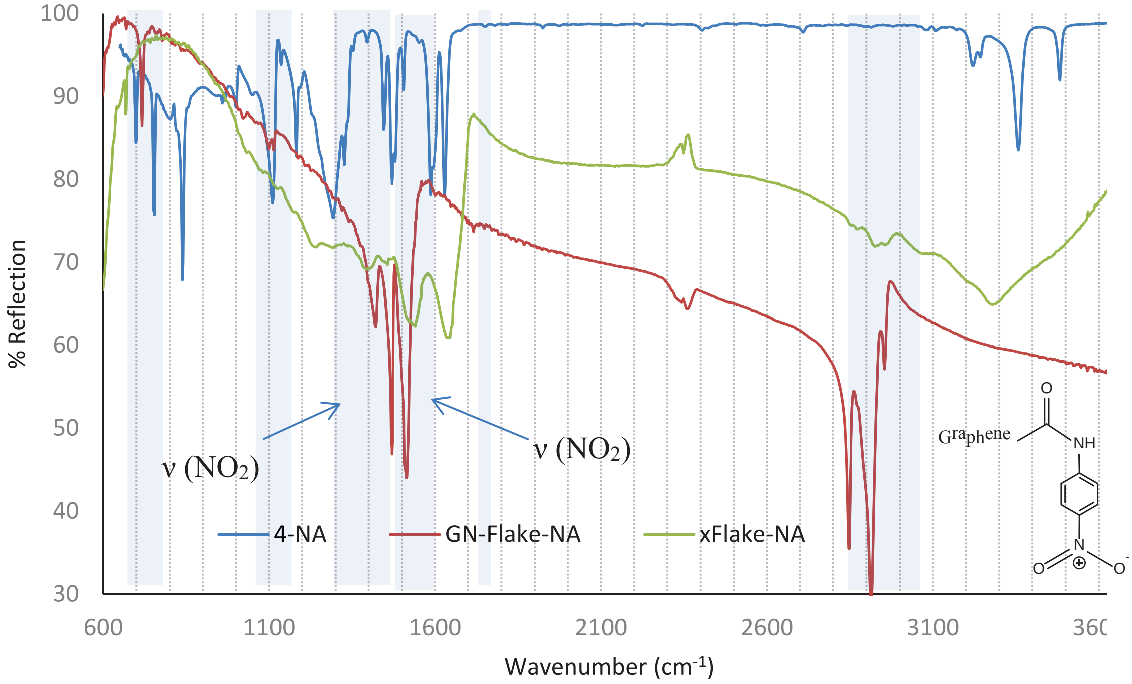

Figure 47: SEIRAS spectra of xFlake-NA, GN-Flake-NA and reflection spectrum of 4-Nitroaniline over the 600-3600 cm^{-1} spectral range. Inset of expected edge structure.

Figure 47 above shows the SEIRAS spectra of xFlake-NA and GN-Flake-NA. The oop and ip NO_2 stretches are characteristic to the 1485-1555 cm^{-1} and 1320-1400 cm^{-1} spectral regions respectively. We can see that both functionalised graphene materials (including the reference spectrum) exhibit bands in this region. The bands are broad, however, and obscured by other bands in this region. Both materials also show CH_x bands lower than would be expected. The ketone is usually weak in SEIRAS spectra of graphene but can be seen at 1690 cm^{-1} in GN-Flake-NA, and is possibly hidden by the broad band at 1650 cm^{-1} in xFlake-NA. The low-frequency region of the spectrum (600-900 cm^{-1}) shows bands for the functionalised materials at similar frequencies to the reference indicating a similar substitution pattern, although this does not confirm what is substituted.

4.2.2.4 Ethylenediamine

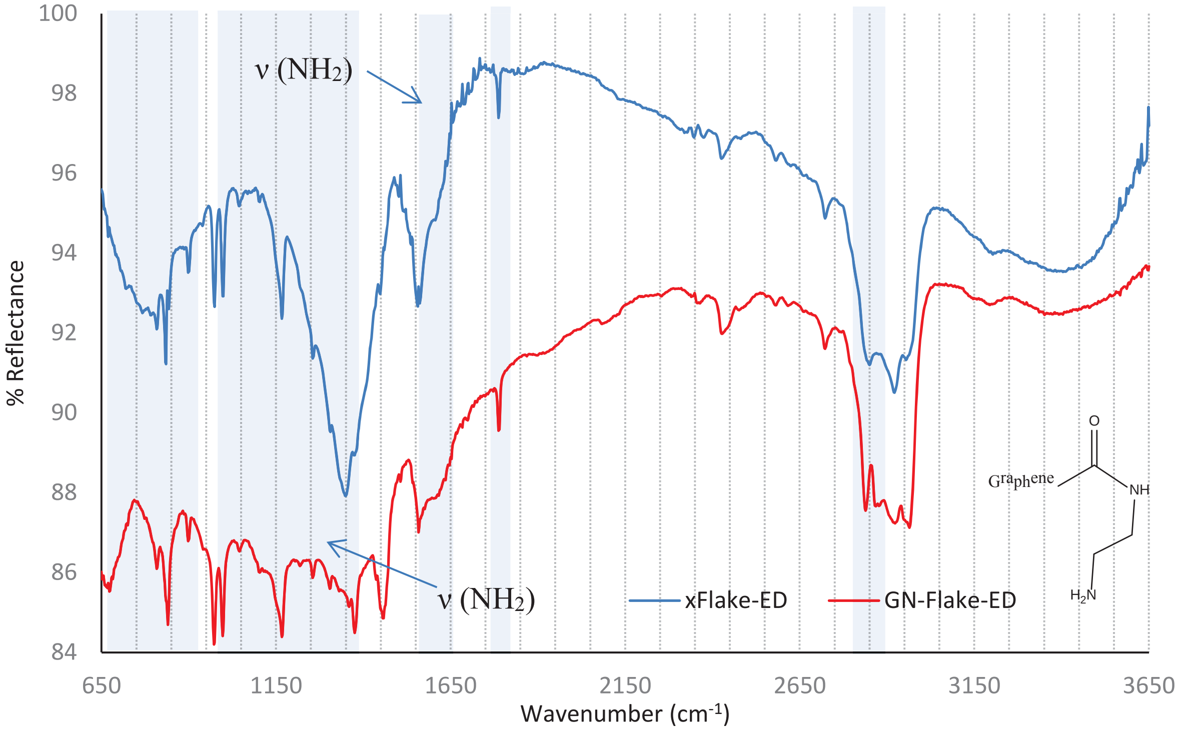

Figure 48: SEIRAS spectra of GN-Flakes-ED and xFlake-ED over the 650-3650 cm^{-1} spectral range. Spectra offset for clarity. Inset of expected edge structure.

Figure 48 above shows the SEIRAS spectra of GN-Flake-ED and xFlake-ED. Ethylenediamine does not have many bands that help differentiate it from functional groups native to graphene flakes. The NH oop stretch can be found around 1500-1650 cm^{-1}. Both ED functionalised graphene samples show a band in this region, but it is also where you would expect to find the C=C ring stretch, making this assignment ambiguous. A similar argument is made for the CH_2 stretch around 2900 cm^{-1}. The N-H rock is characteristic of the 1000-1370 cm^{-1} region. However, this is a wide frequency range so a specific band within this region cannot be assigned. Both functionalised materials show a sharp, weak band at 1790 cm^{-1} assigned to the ketone stretch.

4.2.3 Reductive amination

4.2.3.1 Ferrocencarboxaldehyde Derivative

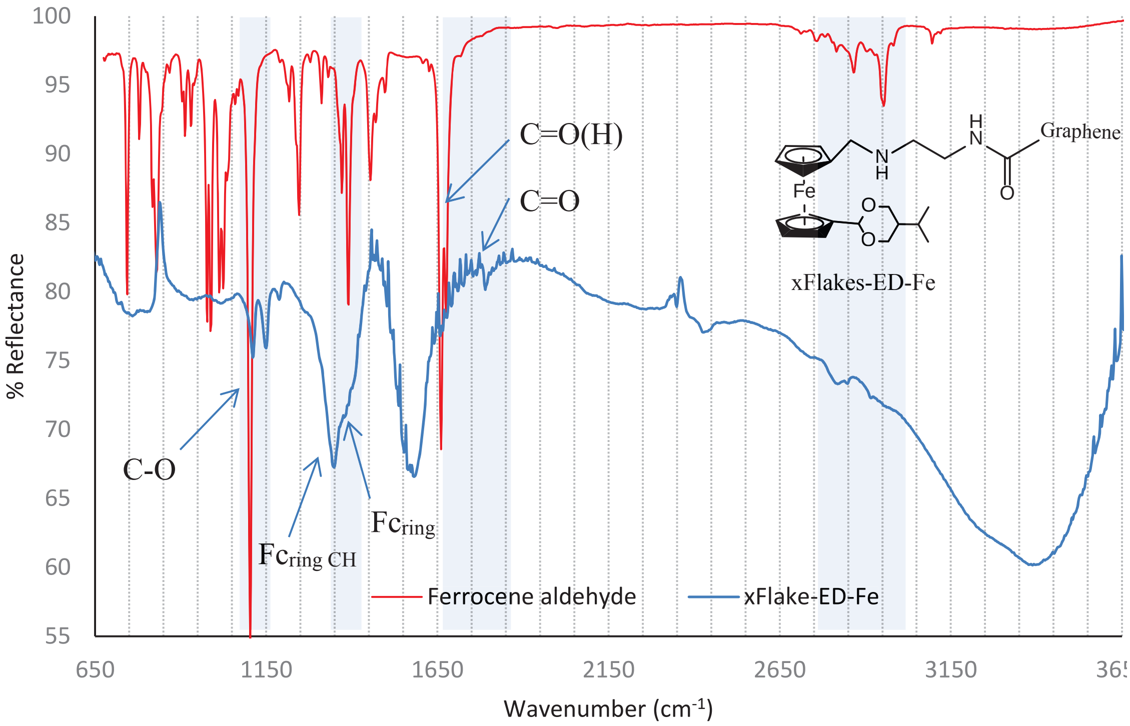

Figure 49: SEIRAS spectra of xFlake-ED-Fe over the 650 - 3650 cm^{-1} spectral range. Spectra offset for clarity. Inset of expected edge structure.

Figure 49 above shows the SEIRAS spectra of xFlake-ED functionalised with the ferrocene derivative and ATR-FTIR spectra of the ferrocene derivative. The ferrocene cyclopentadiene (Fc) ring has characteristic stretches[127] for the ring mode at ≈ 1400 cm^{-1} (Fc$_{\text{ring}}$), the ring CH at ≈ 1350 cm^{-1} and C-O in the 1100-150 cm^{-1} spectral region. These bands can be found above at 1110 cm^{-1} for the C-O stretch, ring C-H at 1348 cm^{-1}, the ring stretch as a shoulder at ≈ 1410 cm^{-1} and the C-O at 1110.8 cm^{-1}. The aldehyde present in the ferrocene compound around 1670 cm^{-1} is not present in the xFlake-ED-Fe which does not indicate successful functionalisation, but does indicate the aldehyde has been reduced. The next section develops the electrochemical setup to monitor redox interconversion of xFlake-ED-Fe.

4.3 Application of SEIRAS to Electrochemistry

The development of electrochemical graphene-based devices requires a better understanding of electrochemical details of graphene materials. This includes the roles that functionality and inherent defects and oxygen contain groups at the edges of graphene. In this section, SEIRAS in conjunction with electrochemistry or *Surface enhanced infrared reflection absorption spectroelectrochemistry* (SEIRASEC) is used to probe the effect of gate bias on the ferrocene functionalised graphene described in section 4.2.6 above. The aim here is to probe, in real time, the interconversion of redox states in xFlakes-ED-Fe.

4.3.1 Electrochemical Device

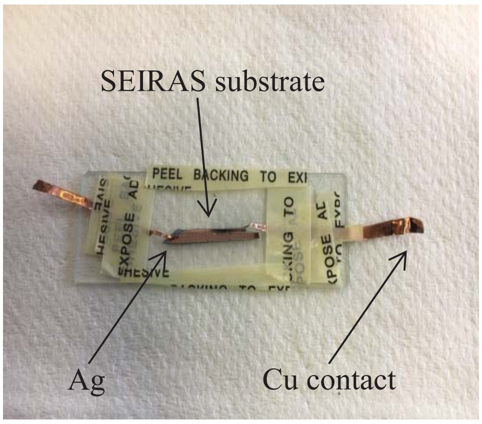

Figure 50: Spectroelectrochemical cell for performing SEIRAS under gate biasing conditions.

The device shown in figure 50 above was fabricated to apply a gating voltage to a SEIRAS substrate. The construction of the cell was carried out as follows. The SEIRAS substrate is first prepared with sample and nanoparticles as described in chapter two and on a glass microscope coverslip located on top of a 3” x 1” glass microscope slide. Source and drain contacts are cut out of copper foil using scissors. The cut is such that the ends connecting to the potentiostat clips are 5 mm wide, and the end contacting the SEIRAS surface is 0.1 mm wide. Before securing the contacts to the microscope slide using cello tape, ends are dipped into dilute HNO_3 to remove oxide before washing with copious amounts of Milli-Q to removal remaining reactants. The copper above the SEIRAS substrate is filled with elemental silver to complete the electrical pathway, secures the circuit and support the contact of the copper to the substrate. This is carried out by carefully placing 2 μL of a complex ion based conducting silver ink $2[Ag(NH_3)_2]CH_3CO_2$ between the headspace of the copper contact and the prepared SEIRAS substrate. The ammonia evaporates over a few minutes precipitating elemental silver as the contact. Resistance across the entire cell measured ≈ 1.0 Ω. If resistance is higher than 1.0 Ω, the cell can be sintered at 90°C to solidify the silver contact.

4.3.2 Redox Activity of Ferrocene Functionalised Graphene Flakes

The goal here is simply to answer the question ‘Can SEIRAS be used to monitor the interconversion of redox states?’ The material being monitored is xFlakes-ED-Fe meaning the conversion of $FeCp_2$ to the ferrocenium cation, $FeCp_2^+$.

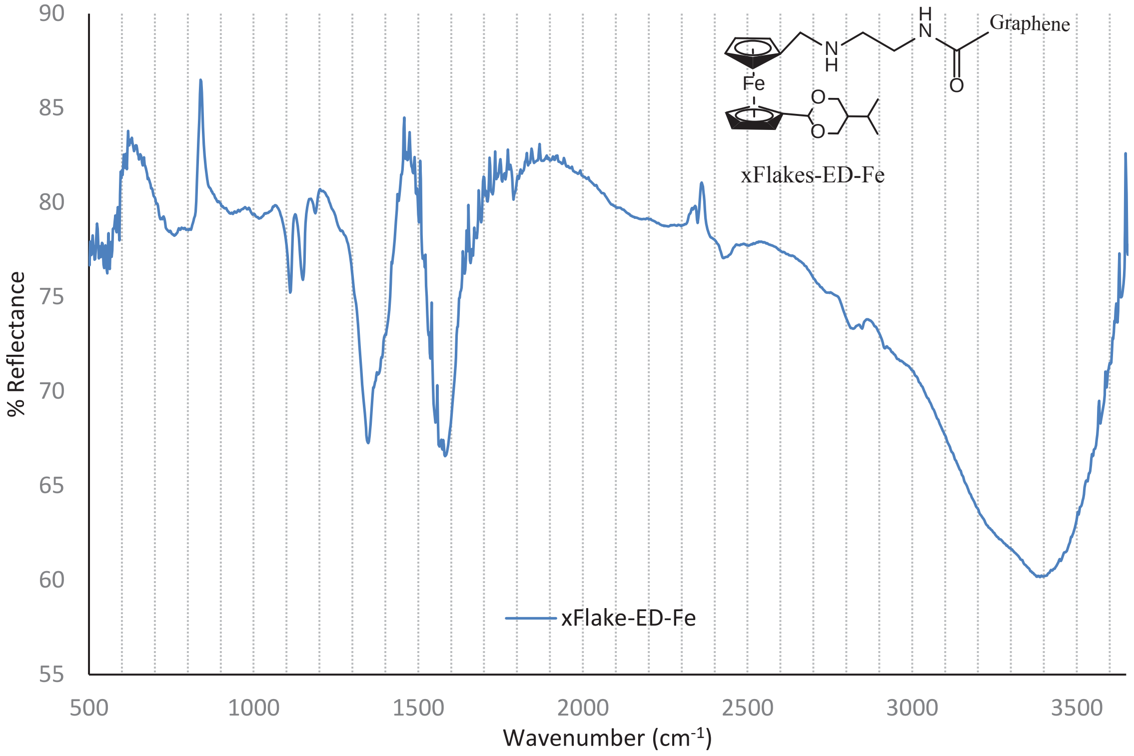
90
85
80
75
70
65
60
55
% Reflectance
500
1000
1500
2000
2500
3000
3500
Wavenumber (cm⁻¹)
xFlake-ED-Fe
Graphene
H
N
N
H
O
Fe
O
O
xFlakes-ED-Fe

(A)

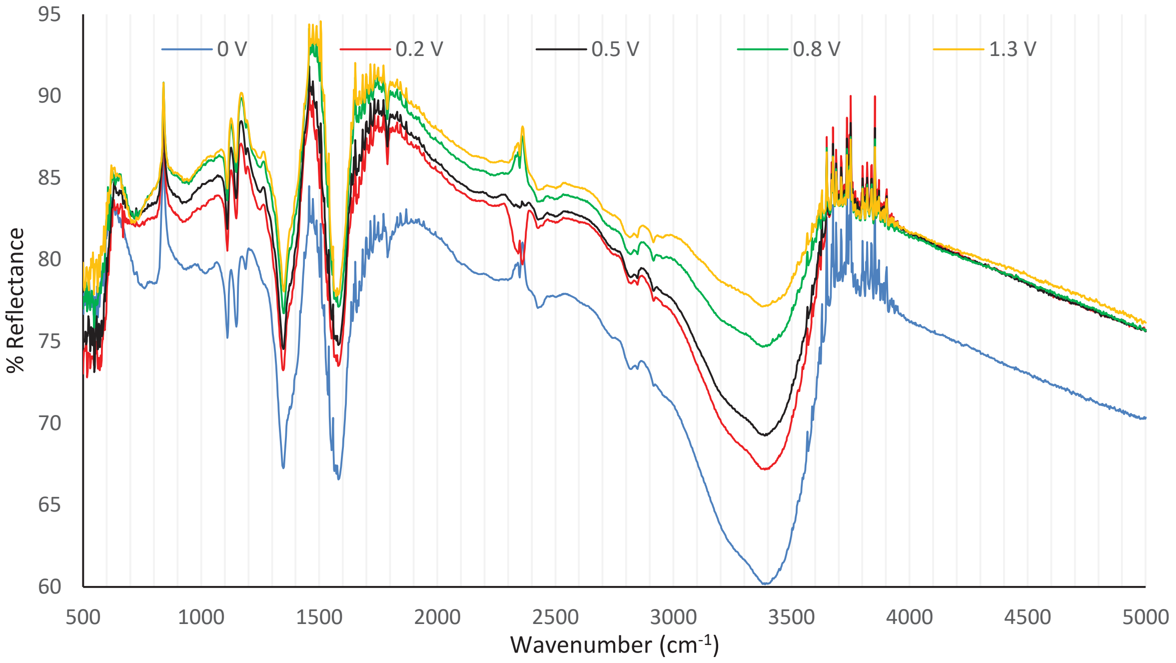
95
90
85
80
75
70
65
60
% Reflectance
0 V
0.2 V
0.5 V
0.8 V
1.3 V
500
1000
1500
2000
2500
3000
3500
4000
4500
5000
Wavenumber (cm⁻¹)

(B)

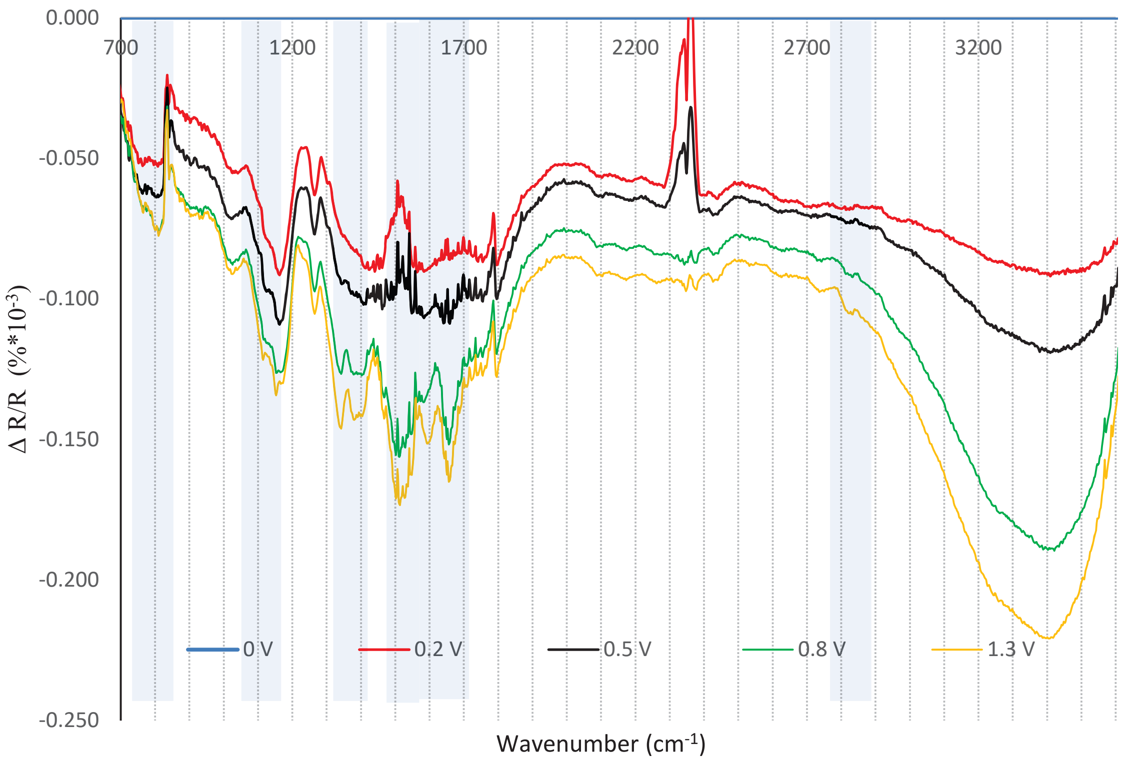

(C)

Figure 51: A) SEIRAS spectra of Flake-ED-FE B) SEIRAS spectra of xFlake-ED-Fe as a function of applied gate voltage and C) Differential spectra of xFlake-ED-Fe as a function of applied voltage. All differential spectra were calculated relative to R_0 representing the scan at 0 V.

Figure 51 (A) shows the SEIRAS spectra of xFlake-ED-Fe without gate biasing for clarity. The bands of interest are at 1110 cm^{-1} for the C-O stretch, 1348 cm^{-1} for the ring C-H and the shoulder at ≈ 1410 cm^{-1} for the Fc rings. Figure 51 (B) overlays SEIRAS spectra as a function of voltage which shows a general trend in reflectivity where increased voltage decreases % reflection. To see more clearly the effect that gate biasing has on individual bands, figure 51 (C) plots the spectra as a differential of the form:

$$\frac{\Delta R}{R}$$

where R is the %R at + 0 V and ΔR is the change in % R between R and R at an applied voltage.

The differential spectra show a number of bands change in intensity. As a function of voltage, the following bands become increasingly more negative e.g. decrease in intensity: 800 cm^{-1} (unassigned), 1348 cm^{-1} (Fc-H), ≈ 1520 cm^{-1} and 1660 cm^{-1} (unassigned), and 2830 cm^{-1} (CH_x). Small shifts are observed for the ketone, and Fc-H stretches of 1789.65 cm^{-1} to 1787.7 cm^{-1} at + 0.8 V for the ketone and 1348.02 cm^{-1} to 1350 cm^{-1} for Fc-H. These could be a result of changes in the orientations of the functional groups or the case of the Fc-H, the ferricenium inductively withdrawing electron density from the carbon as a result of a change in the Fe centres oxidation state from +2 to +3. These assignments as a function of voltage can be found in table 7 below and are in line with what is expected[126-127]. The C-O at 1110 cm^{-1} does not change in intensity but becomes slightly sharper.

Stretch (cm^{-1})	**0 V**	**+ 0.2 V**	**+ 0.5 V**	**+ 0.8 V**	**+ 1.3 V**
Fc stretch	≈ 1410	*	*	*	*
Fc-H	1348.02	1348.02	1350.0	1350.0	1350.0
C-O	1110	1110	1110	1110	1110
C=O	1789.65	1789.65	1789.65	1787.7	1787.7

Table 7: Summary of band positions as a function of applied voltage. *The band appears on a shoulder, so an accurate peak position is not possible.

4.4 Summary

The SEIRAS spectra of functionalised graphene flakes above provide evidence of successful functionalisation with novel reagents, but it is a challenge to confirm the exact chemical bonding through which the functionalisation occurs through as any given individual flake contains a range of functional groups. Since the specific functionality and exact proportions depend on a materials origin and chemical pre/post treatment, literature comparisons are also impossible. Future challenges involve the confirmation of successful synthesis by utilisation of other characterisation methods

The foundation has been laid for SEIRASEC where a change in the intensity of ferrocene functionalised flakes bands were observed. Future work regarding the electrochemistry would involve the use of other metal ferrocenes.

Chapter Five – BODIPY Functionalisation of Graphene

Background

Boron dipyrinns ('BODIPYs') or 4,4-difluoro-bora-3a,4a-diaza-s-indacene's (*e.g.* Cl-BODIPY) as shown in figure 51 can be thought of as half-porphyrins. Cl-BODIPY, in particular, has excellent photo absorbing properties, well-defined chemistry[102], an $\varepsilon > 80{,}000\ \mathrm{Mol}^{-1}\mathrm{cm}^{-1}$ and a quantum yield close to one in Chloroform[94]. These photonic properties have facilitated its use in many applications (*e.g.* solar cells)[95]. However, the major challenge of using BODIPYs in conventional solar cells are their narrow absorption range meaning the majority of the sun's energy is left untapped. Ideally, solar cells would absorb over the entire 200 - 1200 nm spectral range. Cl-BODIPY in conjunction with graphene may provide a solution to this problem. Carbon-based materials offer attractive features for use in next-generation solar cells. Firstly, carbon is abundant, offering potential for cheap devices which also exhibit unique electronic and mechanical properties (*e.g.* electrically conductive, flexible devices). Secondly, graphene can be dispersed and deposited using solution-based processing techniques allowing their integration and incorporation into large scale fabrication processes.

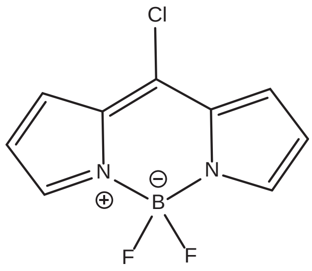

Figure 51: Cl-BODIPY

The aim of this chapter is to utilise Cl-BODIPY's electrophilic C-Cl bond to covalently functionalised graphene and the charged, flat molecular backbone for it's physisorption to produce potential photo-sensitive materials. These aims are carried out to lay the groundwork for producing photo-active BODIPY-Graphene materials as a basis for producing solid state solar cells. It is noted that the building of a working cell is outside of the scope of this chapter.

5.0 BODIPY Functionalisation of Graphene Flakes

Two methodologies were used to attach Cl-BODIPY to graphene. Adsorption or 'physisorption' and chemical attachment or 'chemisorption'. Physisorption is defined as a reversible adsorption to a surface by van der Waals or other weak interactions. Physisorption has the benefit of being a quick and easy to prepare functionalisation route. The materials may also have predictable electronic properties due to the minimal disturbance that occurs upon adsorption (*e.g.* absence of an activation energy barrier).

Chemisorption is the direct covalent attachment of a molecule (or fragment) to a surface and is carried out by nucleophilic addition at Cl-BODIPYS electrophilic C-Cl bond. Chemisorption does, however, have an activation energy which may add complexity to the material. Figure 52 below schematically shows a solid-state solar cell to highlight the role of these materials and as the context for the remainder of this chapter.

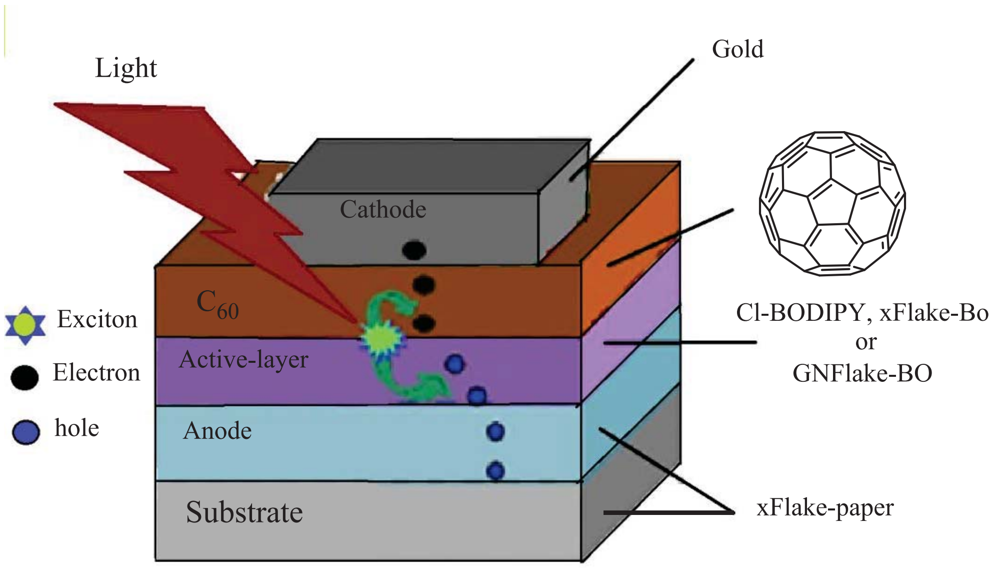

Figure 52: Scheme 10. Diagram of a solid-state solar cell. Figure recreated with permission from Ramuz[99]. © 2012 American Chemical Society.

Figure 52 above shows the general structure of a *solid-state solar cell (SSSC)*. SSSCs consist of a substrate as the solid support (*e.g.* glass). The Anode is an electrically conducting or 'electron accepting' layer. The active-layer is a sensitiser or, colloquially, exciton generating active layer. The hole-accepting layer, denoted as C_{60}, is a spherical fullerene, colloquially, Buckminsterfullerene - commonly used as a hole acceptor. The final layer on top is an electrically conducting layer of ≈ 50 nm of gold obtained via sputtering. The production and characterisation of materials for the first three layers is carried out in the remainder of this chapter.

5.1 Covalent Functionalisation

Chapter four showed the presence of hydroxyl functional groups in GN-flakes and xFlakes. A huge range of reactions has been carried out in literature through substitution of the highly electrophilic chlorine on the base BODIPY and a nucleophile. A very straight forward reaction occurs between alcohols and BODIPY, where covalent bonds form via a substitution reaction between chlorine and an alcohol. Figure 53 below shows the generalised nucleophilic substitution reaction scheme utilised to covalently functionalised xFlakes and GN-Flakes.

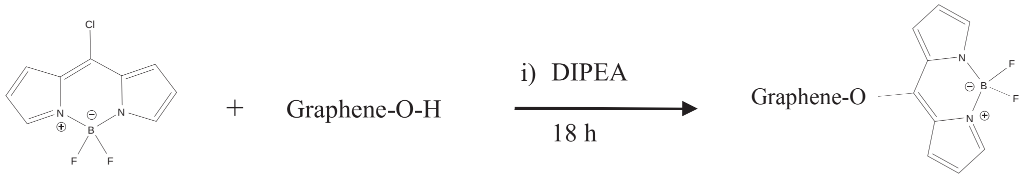

Figure 53: Scheme 11. Covalent functionalisation of graphene with BODIPY via base assisted nucleophilic addition over 18 hours. i) Diisopropylethylamine.

Graphene flakes were dispersed in THF to give a 0.5 mg/ml colloidal suspension. The black solutions were sonicated at 1200 W for 30 minutes. 2.0 µL (2.0 eq) of *Diisopropylethylamine (DIPEA)* was added to the dispersed graphene flake solutions and sonicated for a further 30 minutes before addition of Cl-BODIPY (1.3 mg, 1.0 eq.). The solutions were purged and placed under an inert atmosphere of argon and allowed to sonicate for 18 hours before being washed with THF five times using centrifugation to separated solid from the supernatant. Residual solvent was removed under vacuum to obtain black solids: *xFlake-BO and GN-Flake-BO.*

5.1.1 SEIRAS

SEIRAS is utilised to characterise the covalent functionalisation of graphene flakes with Cl-BODIPY. BODIPY compounds exhibit a number of bands in the spectral region comprising fundamentals. For clarity purposes, the spectral analysis of bands is limited to 650-1750 cm^{-1}. BODIPY compounds exhibit five common bands in the 650-1750 cm^{-1} region, with band shapes and positions deviating only slightly between similar compounds. Figure 54 shows a mid-IR reflection spectrum of Cl-BODIPY where these characteristic bands are present at approximately 770, 1100, 1240, 1400 and 1600 cm^{-1}. Theses bands are utilised to analyse SEIRAS spectra of BODIPY functionalised graphene flakes as also shown in figure 54.

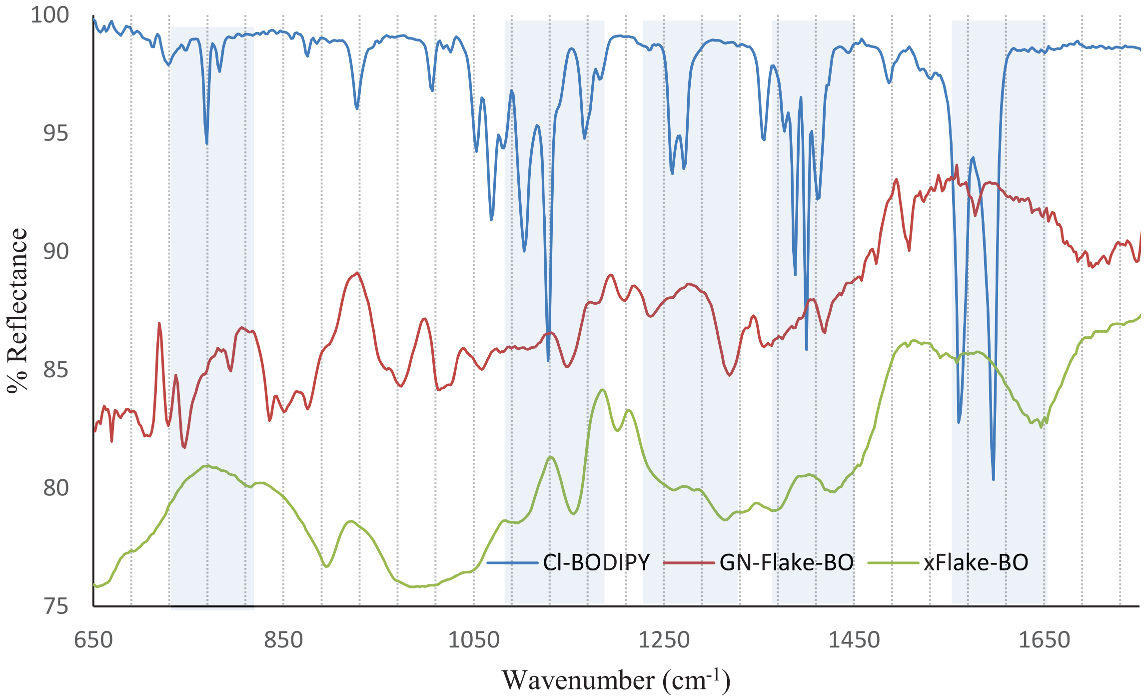

Figure 54: Reflection absorption spectra of Cl-BODIPY and SEIRA spectra of GN-flake-BO and xFlake-BO between 650-1750 cm^{-1}. Spectra off-set for clarity.

Figure 54 above shows the SEIRA spectra of GN-flake-BO and xFlake-BO over the 650-1750 cm^{-1} spectral region. Cl-BODIPY mid-IR reflectance spectra is overlaid as a control and an illustration of characteristic band positions. GN-Flake-BO and xFlake-BO both exhibit bands around 770, 1100, 1240, 1400 and 1600 cm^{-1}. Assigning these bands unambiguously is not possible but it may be possible using computational chemistry. This is, however, outside the scope of this chapter. The appearance of these five bands in their particular regions provides evidence that covalent functionalization was successful. Further evidence from other techniques is of value to back this conclusion.

5.2 Physisorption

Electrostatic or ‘physical absorption’ of BODIPYs represent an alternate method for producing photo sensitive materials in a relatively easy and straight forward manner due to the simplicity of preparation procedures[96-98]. The large specific surface area (2600 m^2/g), outstanding mechanical, and electrical properties, and high carrier mobility make graphene an attractive material for photovoltaic devices. This section sets the groundwork for surface absorption of chromophoric compounds through van der Waals and π-π stacking interactions of Cl-BODIPY and xFlakes. The focus of this section concentrates on the use of graphene as a substrate. GN-Flakes are not utilised due to limitations in production quantities.

5.2.1 Graphene Substrate Preparation

The procedure by which Cl-BODIPY is physisorbed in proceeding sections is produced as follows: xFlakes are dispersed in DMF (2 mg/ml, 1000 W, 15 minutes), and 10 mL is poured onto filter paper (grade 1, 10 mm radii). The captured material is air dried under water pump vacuum filtration for 60 minutes, washed with THF two times, and the resulting film is left to dry overnight before being pressed at 10 tonnes of pressure for sixty seconds. The resulting material, termed *xFlake-Paper,* is shown in figure 55 below.

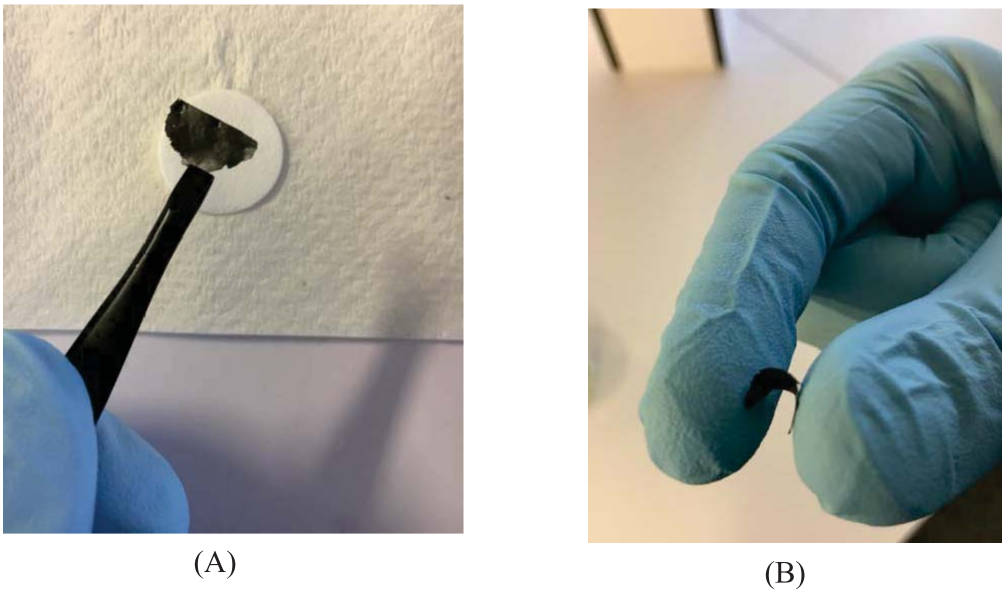
(A) (B)

Figure 55: Images of xFlake-paper produced from xFlakes showing A) Self-supporting film cut along the circular axis with scissors and B) Intrinsic material flexibility.

Figure 55 above shows the film that results from filtering and pressing graphene. Figure 55 (A/B) illustrate the free-standing, flexible easily sizeable properties of xFlake-Paper. The electrical resistance of the substrate is worthy of note. xFlake-paper was measured to have a resistance of 40 Ω/cm^2. Optimising this parameter is key before its utilisation in cell development.

5.2.2 Scanning Electron Microscopy

STEM is used to characterise topological features of xFlake-Paper. STEM provides insights into packing orientations of individual flakes and later the morphological distribution of physisorbed Cl-BODIPY.

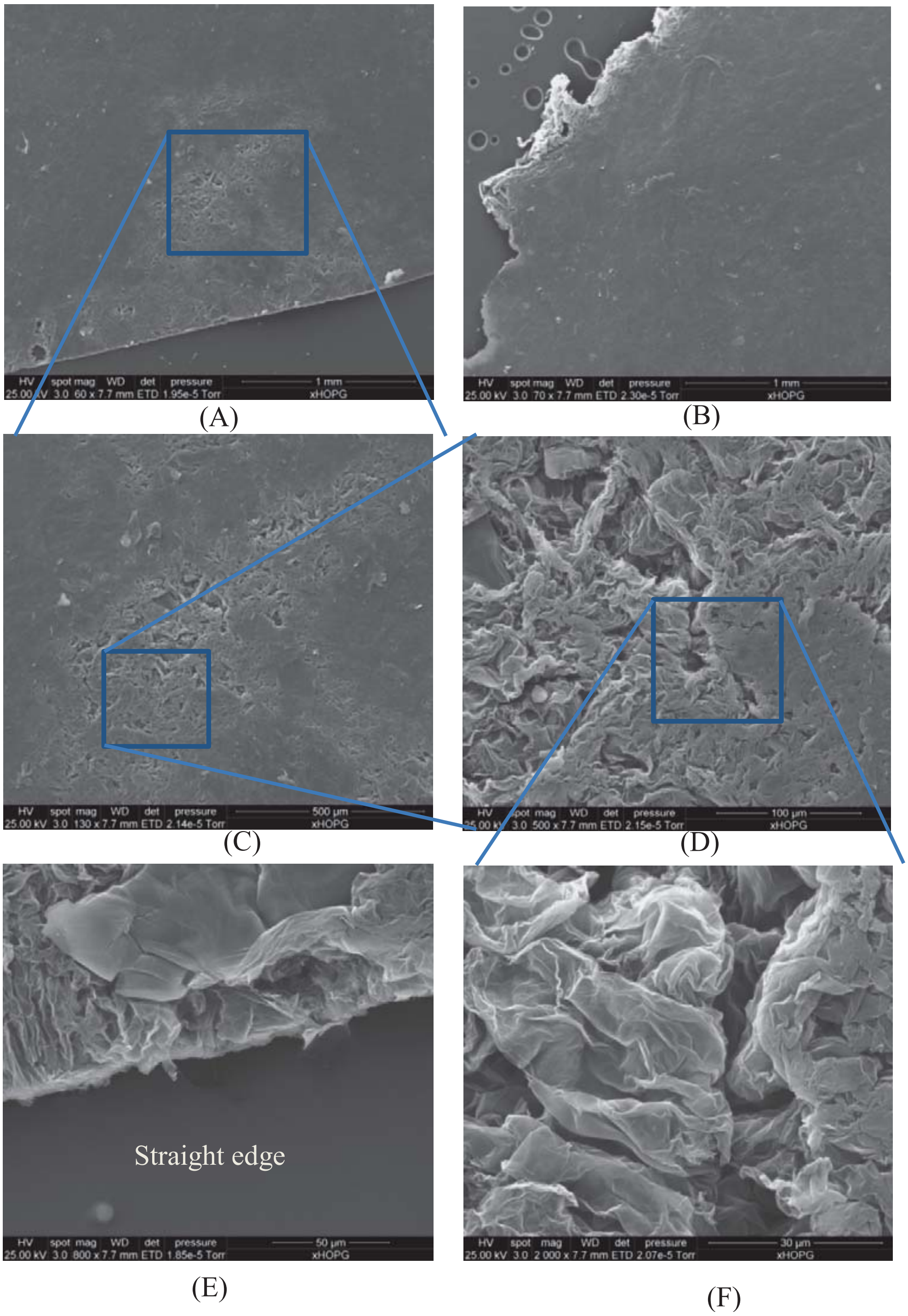

Figure 56: STEM images of xFlake-paper. A/B) 60x showing bulk and edge morphology respectively. C/D) 130 and 500x detailing microscopic roughness. E) 800x of the straight edge showing mechanical interlocking. F) 2000x showing the wrinkling of graphene sheets.

Figure 56 shows typical STEM pictures of xFlake-Paper. Figure 56 (A/B) are 60x magnification images of the morphology of two regions of a piece of the material showing the straight cut edge and rough ‘as pressed' edge regions respectively. Increasing the magnification of the area in (A) reveals a region of particular interest for solar cells. The regions appear 'rough' (*i.e.* high surface area), which could be beneficial for BODIPY absorption but also detrimental to device durability because it is a mechanically weak spot. In other words, Figure 56 (C) is a region where tears and rips will likely start. This region, as well as other similar regions, may present areas of low shunt resistance. This would effect shunt resistance and ultimately the efficiency of any solar cell utilising this material. Further understanding of how these manifest and optimisation would be of value. Figure 56 (D/F) magnifies this region to 500x and 2000x respectively, showing what appear to be the individual compressed regions of graphene flakes. The straight edge in figure 56 (E) is shown at 800x magnification and shows the overlapping packing topology of graphene sheets of various sizes which are cleaved when cutting with scissors.

5.2.3 Cl-BODIPY to xFlake-Paper

The physisorption of Cl-BODIPY to xFlake-paper was carried by pipetting $\frac{0.01\,mL}{cm^2}$ of a solution of Cl-BODIPY solution in DMF ($0.2\,\frac{mg}{ml}$) and oven drying at 110 °C. The packing of Cl-BODIPY on the surface was characterised using STEM chlorine elemental mapping. Figure 57 below shows the typical elemental mapping images of xFlake-paper with Cl-BODIPY.

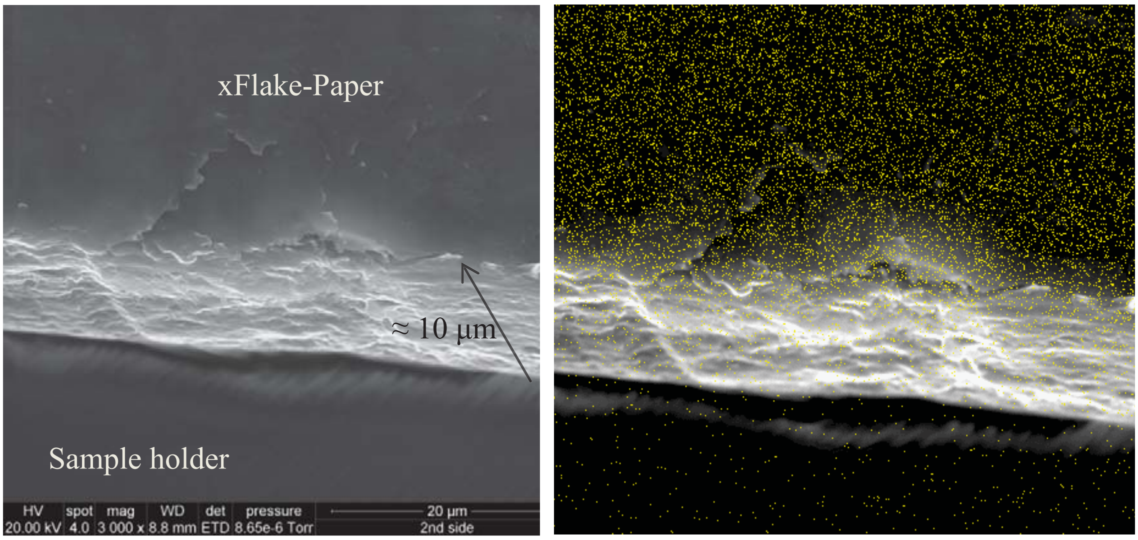

(A) (B)

Figure 57: 2D SEM images of graphene flakes with adsorbed Cl-BODIPY. A) STEM image of an edge of 10 µM height and the middle of a small region of the substrate and B) 2D chlorine mapping of xFlake-Paper with physisorbed Cl-BODIPY. The density of yellow dots is in direct proportion to the density of Cl-BODIPY.

Figure 57 (A) above shows a small region of xFlake-paper with physisorbed Cl-BODIPY. The edge, as cut with scissors, is 10 µm high. The cut was carried out after the physisorption procedure described above. The important observation is the absence of crystals and clumps indicating a homogeneous film formation on the surface. Figure 57 (B) shows a chlorine elemental STEM image. The distribution of chlorine in 2D appears as yellow spots. A trend can be observed where mapping of chlorine (Cl-BODIPY) is distributed on the top in the highest density. The absence of crystals is indicative of physisorption. Chlorine is also on the side-face but is likely a result of contamination by scissors during the cutting process. The sample holder indicates the presence of chlorine (low density) which is assumed to be noise but could also be contamination.

5.3 Summary

The successful preparation of an electrically conductive and flexible graphene substrate has laid the groundwork for the development of a graphene-BODIPY solar cell based on the physical absorption or covalent modification procedures described in this chapter. SEIRAS indicates successful covalent functionalisation while elemental STEM mapping confirms physisorption. The development of a protocol for controlling the active layer's thickness is the next step in developing a solar cell. The active layer precedes the covering with a hole acceptor and finally an electrically conductive layer of gold. The hole acceptor being C_{60} and gold layer added using vacuum assisted sputtering techniques.

Chapter Six - Conclusions

Production of graphene was carried out via two methods; liquid-phase electrochemical exfoliation and solid-phase graphite nanotomy. Ultraviolet-visible spectroscopy in conjunction with Raman, electron and atomic force microscopy was utilised to characterise materials before the development of SEIRAS, the main spectral characterisation technique. SEIRAS provided insights into graphene's defects before their use as chemical handles in functionalisation with novel reagents. The successful covalent functionalisation lead to probing the interconversion of ferrocene functionalised graphene by SEIRASEC. Exploration of Cl-BODIPY as a basis for photo-active layer laid the foundations for a graphene-based solid state solar cell. The physisorbed attachment was characterised by elemental mapping, while SEIRAS indicated successful covalent functionalisation.

Outlook and Future Directions

SEIRAS is of considerable interest due to its ability to effectively characterise functionalised graphene materials. The future direction of SEIRAS is the development of chemical modification protocols of increased complexity and further applications *e.g.* sensors and solar cells.

Graphene production methods also need to be developed further. GN-flakes edge structure appeared random so developing a protocol of controlled and repeatable cutting is desirable. SEIRAS enhancement mechanisms were discussed, however, whether phonons are contributing to enhancement is not known, so determining this by using nanoparticles without mid-IR active plasmons is one approach that will be carried out. Lastly, it is a curious thought as to whether the physisorption of BODIPY derivatives to graphene flakes can be optimised. The direction here is the study of graphene-BODIPY interactions from the viewpoint of fundamental interactions and electronic overlap to optimise the interaction between BODIPY and graphene.

Bibliography

1. Shafiee, S., Topal, E. (2009). When will fossil fuel reserves be diminished? Energy Policy, 37, 181-189.
2. International energy agency. (2015). Monthly electricity statistics (March 2015). Retrieved from http://www.iea.org/statistics/topics/Electricity
3. Saga, T. (2010). Advances in crystalline silicon solar cell technology for industrial mass production. NPG Asia Mater., 2(3) 96-102.
4. Kalogirous, S.A. (2014). Solar energy engineering processes and systems (2nd ed.). Waltham, MA: Elsevier Press.
5. Hedberg, J. (2015). Free science images. Retrieved from http://www.jameshedberg.com/scienceGraphics.php?id=graphene-wavey-lensBlur
6. Nair, R.R., Blake, P., Grigorenko, A.N., Novoselov, K.S., Booth, T.J., Stauber, T., … Geim, A.K. (2008). Fine structure constant defines visual transparency of graphene. Science, 320(5881), 1308.
7. Morozov, S.V., Novoselov, K.S., Katsnelson, M.I., Schedin, F., Elias, D.C., Jaszczak, J.A., Geim, A.K. (2008). Giant intrinsic carrier mobilities in graphene and its bilayer. Phys. Rev. Lett, 100(1), 016602.
8. Peigney, A., Laurent, C., Flahaut, E., Bacsa, R., Rousset, A. (2001). Specific surface area of carbon nanotubes and bundles of carbon nanotubes. Carbon, 39(4), 507-514.
9. Thrower, P. A. (1969). The study of defects in graphite by transmission electron microscopy. Chemistry and physics of carbon, 5, 217-319
10. Stone, A. J., Wales, D. J. (1986). Theoretical studies of icosahedral C_{60} and some related species. Chemical physics letters, 128(5-6), 501-503.
11. Wei, D., Liu, Y., Wang, Y., Zhang, G., Huang, L., Yu, Gui. (2009). Synthesis of N-doped graphene by chemical vapor deposition and its electrical properties. Nano Lett., 9(5), 1752-1758.

12. Leibniz-Institut für innovative Mikroelektronik. (2015). Sketch of the electronic structure of graphene, cone-shape linear electronic dispersion and density of states. Retrieved from http://www.ihp-microelectronics.com/de/forschung/materialien-fuer-die-mikro-und-nanoelektronik/projekte/graphene/graphene.html

13. Goerbig, M. O. (2011). Electronic properties of graphene in a strong magnetic field. Rev. Mod. Phy., 83(4), 1193-1243.

14. Jiang, D., Chen, Z. (2013). Graphene chemistry: theoretical perspectives. West Sussex, United Kingdom: John Wiley & Sons Ltd.

15. Wolf, E.L. (2014). Graphene: A new paradigm in condensed matter and device physics. New york, United states: Oxford University press.

16. Chua, C.K., Pumera, M. (2013). Covalent chemistry on graphene. Chem. Soc. Rev., 42, 3222-3233.

17. Georgakilas, V., Otyepka, M., Bourlinos, A.B., Chandra, V., Kim, N., Kemp, K. C., … Kim, K. (2015). Functionalization of graphene: Covalent and non-covalent approaches, derivatives and applications. Chem. Rev., 112(11), 6156-6214.

18. Rao, C.N.R., Gopalakrishnan, K., Govindaraj, A. (2014). Synthesis, properties and applications of graphene doped with boron, nitrogen and other elements. Nano today., 9(1), 324-343.

19. Choi, S., Jhi, S., Son, Y. (2010). Controlling energy gap of bilayer graphene by strain. Nano lett., 10(1), 3486-3489.

20. Ni, Z. H., Yu, T., Lu, Y.H., Wang, Y.Y., Feng, Y.P., Shen, Z.X. (2008). Uniaxial strain on graphene: Raman spectroscopy study and band-gap opening. ACS Nano., 2(11), 2301-2305.

21. Guinea, F., Katsnelson, M.I., Geim, A.K. (2010). Energy gaps and a zero-field quantum hall effect in graphene by strain engineering. Nat. Phys., 6(1), 30-33.

22. Gorbar, E.V., Gusynin, V.P., Miransky, V.A. (2010). Energy gaps at neutrality point in bilayer graphene in a magnetic field. J. Exp. Theor. Phys. Lett., 91(6), 314-318.

23. Roy, B., Yang, K. (2013). Bilayer graphene with parallel magnetic field and twisting: phases and phase transitions in a highly tunable Dirac system. Phys. Rev. B., 88(1).

24. Zhang, Y., Tang, T., Girit, C., Martin, M. C., Zettl, Z., Crommie, M. F., Shen, Y.R., Wang, F. (2009). Direct Observation of a widely tunable bandgap in bilayer graphene. Nature Letters., 459(7248), 820-823.

25. Mak, K. F., Ju, l., Wang, F., Heinz, T. F. (2012). Optical spectroscopy of graphene: from the far infrared to the ultraviolet. Solid state communications 152(15), 1341-1349.

26. Nicolas, R., Leveque, G., Djouda, J., Montay, G., Madi, Y., Plain, J., Herro, Z., Kazan, M., Adam, P., Maurer, T. (2015) Plasmonic mode interferences and Fano resonances in metal-insulator-metal nanostructured interfaces. Sci. Rep. (5), 14419.

27. Cardona, M. (2001). Renormalization of the optical response of semiconductors by the electron-phonon interaction. Physica status solidi(a)., 188(4), 1209-1232.

28. Langreth, D. C. (1985). Energy transfer at surfaces: Asymmetric line shapes and the electron-hole-pair mechanism. Phys. Rev. Lett., 54(2), 126-129.

29. Tang, T., Zhang, Y., Park, C., Geng, B., Girit, C., Hao, Z., Martin, M., Zettl, A., Crommie, M. F., Louie, S. G., Shen, Y. R., Wang, F. (2010). A tunable phonon-exciton Fano system in bilayer graphene. Nat. Nanotechnology., 5, 32-36.

30. Fano, U. (1961). Effects of configuration interaction on intensities and phase shifts. Phys. Rev. 124(6), 1866-1878.

31. Biro, L., Lambin, P. (2013). Grain boundaries in graphene grown by chemical vapor deposition. New J. of Physics 15(1)., 35024.

32. Yang, p., Liu, D. (2014). Understanding graphene production by ionic surfactant exfoliation: A molecular dynamics simulation study. J. App. Phys., 116, 14304.

33. Lounasvuori, M. M., Rosillo-Lopez, M., Salzmann, C. G., Caruana, D. J., Holt, K. B. (2015). The influence of acidic edge groups on the electrochemical performance of graphene nanoflakes. J. Electroanal. Chem., 753(1), 28-34.

34. Lounasvuori, M. M., Rosillo-Lopez, M., Salzmann, C. G., Caruana, D. J., Holt, K. B. (2014). Electrochemical characterisation of graphene nanoflakes with functionalised edges. Faraday Discuss., 172(1), 293-310.

35. Parvez, K., Wu, Z., Li, R., Liu, X., Graf, R., Feng, X., Mullen, K. (2014). Exfoliation of graphite into graphene in aqueous solutions of inorganic salts. J. Am. Chem. Soc., 136(16), 6083-6091.

36. Zhang, R., Chen, T., Bunting, A., Cheung, R. (2016). Optical lithography technique for the fabrication of devices from mechanically exfoliated two-dimension materials. Microelectronic engineering., 154(1), 62-68.

37. Ren, H. Li, Q., Su, H., Shi, Q. W., Chen, J., Yang, J. (2008). Edge effects on the electronic structures of chemically modified armchair graphene nanoribbons. Condensed. Matter, 1-5, doi: arXiv:0711.1700v1

38. Huang, B. Li, Z. Liu, Z., Zhou, G. Hao, S. Wu, J., Gu, B., Duan, W. (2008). Adsorption of gas molecules on graphene nanoribbons and its implication for nanoscale molecule sensor. J. Phys. Chem. C, 112(35), 13442-13446.

39. Rosenkranz, N., Till, C., Thomsen, C., Maultzsch, J. (2011). Ab initio calculations of edge-functionalized armchair graphene nanoribbons: Structural, electronic, and vibrational effects. Phys. Rev. B., 84, 195438.

40. Mohanty, N., Moore, D., Xu, Z., Sreeprasad, T. S., Nagaraja, A., Rodriguez, A. A., Berry, V. (2012). Nanotomy-based production of transferable and dispersible graphene nanostructures of controlled shape and size. Nat. Commun., 3(1), 844.

41. Taniguchi, T., Kurihara, S., Tateishi, H., Hatakeyama, K., Koinuma, M., Yokoi, H., Hara, M., Ishikawa, H., Matsumoto, Y. (2015). pH-driven, reversible epoxy ring opening/closing in graphene oxide. Carbon, 84, 560-566.

42. Umar, K. O'Neill, A., Lotya, A., Lotya, M., De, S., Coleman, J. (2010). High-concentration solvent exfoliation of graphene. Small, 6(7), 864-871.

43. Lima, Aruoff. L., Müssnich, L. A. M., Manhabosco, T. M., Chacham, H., Batista, R. J. C., Oliverira, A. B. (2015). Soliton instability and fold formation in laterally compressed graphene. Nanotechnology, 26(4), 45707-45714.

44. Pan, C. T., Hinks, J. A., Ramasse, Q. M. Greaves, G., Banger, U. Donnelly, S. E., Haigh, S. J. (2014). In-situ observation and atomic resolution imaging of the ion irradiation induced amorphisation of graphene. Sci. rep, 4, 6334.

45. Boukhvalov, D. W. (2010). Tunable molecular doping of corrugated graphene. Surface science., 604(23-24), 2190-2193.

46. Baimova, J. A. Korznikova, E. A., Dmitirev, S. V., Liu, B., Zhou, K. (2016). Wrinkles and wrinklons in graphene and graphene nanoribbons under strain. Current Nanoscience, 12(2), 184-191.

47. Deng, S., Berry, V. (2014). Wrinkled, rippled and crumpled graphene: an overview of formation mechanism, electronic properties, and applications. (2016) Mater. Today., 19(4), 197-212.

48. Malard, L. M., Pimenta, M. A., Dresselhaus, G., Dresselhaus, M. S. (2009). Raman spectroscopy in graphene. Phys. Rep., 473(5), 51-87.

49. Ferrari, A. C., Basko, D. M. (2013). Raman spectroscopy as a versatile tool for studying the properties of graphene. Nat. Nanotechnol., 8(4), 235-246.

50. Moon, I. K., Lee, j., Ruoff, R. S., Lee, H. (2010). Reduced graphene oxide by chemical graphitization. Nat. Comms., 1, 73.

51. Mak, K. F., Shan, J., Heinz, T.F. (y). Seeing many-body effects in single and few-layer graphene: Observation of two-dimensional saddle-point excitons. Phys. Rev. Lett. 106, 046401.

52. Wakabayashi, K., Fujita, M., Ajiki, H., Sigrist, M. (1999). Electronic and magnetic properties of nanographite ribbons. Phys. Rev. B., 59(12), 8271-8282.

53. Yang, Y. Zhang, L., Osawa, M., Cai, W. (2013). Surface-enhanced infrared spectroscopic study of a CO-covered Pt electrode in room-temperature ionic liquid. J. Phys. Chem. Lett., 4(10), 1582-1586.

54. Yoshimoto, S., Ono, Y., Kuwahara, Y., Nishiyama, K., Taniguchi, I. (2016). Structural changes of 4,4'-(dithiol butylene)dipyridine SAM on a Au(111) electrode with applied potential and solution pH and influence of alkyl chain length of pyridine-terminated thiolate SAMs on cytochrome c electrochemistry. J. Phys. Chem. C, 120(29), 15803-15813.
55. Patching, S. G. (2014). Surface plasmon resonance spectroscopy for characterisation of membrane protein-ligan interactions and its potential for drug discovery. Biochimica et Biophysica Acta., 1838(1), 43-55.
56. Bjerke, A., Griffiths, P. (1999). Surface-enhanced infrared absorption of CO on platinized platinum. Anal. Chem., 71, 1967-1974.
57. Hu, Hai., Yang, X., Zhai, F., Hu, D., Liu, R., Liu, K., Sun, Z., Dai, Q. (2016). Far-field nanoscale infrared spectroscopy of vibrational fingerprints of molecules with graphene plasmons. Nat. Commun., 7, 12334.
58. Hartstein, A., Kirtley, J. R., Tsang, J. C. (1980). Enhancement of the infrared absorption from molecular monolayers with thin metal overlayers. Phys. Rev. Lett., 45(3), 201-204.
59. G. T. Merklin., Griffith, P. R. (1997). Influence of chemical interactions of the surface enhanced infrared absorption spectrometry of nitrophenols on copper and silver films., Langmuir, 13, 6159-6163.
60. Osawa, M., Ikeda, M. (1991). Surface-enhanced infrared absorption of p-nitrobenzoic acid deposited on silver island films: contribution of electromagnetic and chemical mechanisms., J. Phys. Chem., 95, 9914-9919.
61. Osawa, M. (1997). Bull. Chem. Soc. Jpn., 70(1), 2861-2880.
62. Metiu, H. (1984). Surface enhanced spectroscopy, Prog. Surf. Sci. 17, 153-320.
63. Moskovits, M. (1985). Surface-enhanced spectroscopy., Rev. Mod. Phys., 57, 783-826.
64. Wakaun, A., Surface-enhanced electromagnetic processes, in Solid State Physics, H. Ehrenreich, D. Turnbull (Eds.) (Academic, New York, 1984) 38, pp. 223–294.

65. Gerstan, J. I., Nitzan, A. (1985). Photophysics and photochemistry near surfaces and small particles. Surf. Sci., 158, 165-189.

66. Benz, F., Schmidt, M. K., Dreismann, A., Chikkaraddy, R., Zhang, Y., Demetriadou, A., Carnegie, C., Ohadi, H., Nijs, B., Esteban, R., Aizpurua, J., Baumberg, J. J. (2016). Single-molecule optomechanics in “picocavities”. Science, 11(354), 6313, 726-729.

67. Kamata, T., Kato, A., Umemura, J., Takenaka, T. (1987). Intensity enhancement of infrared attenuated total reflection spectra of stearic acid Langmuir-Blodgett Monolayers with evaporated silver island films. Langmuir, 3, 1150-1154.

68. Kellner, R., Mizaikoff, B., Jakusch, M., Wanzenbock, H. D., Weissenbacher, N. (1997). Surface-enhanced Vibrational spectroscopy: A new tool in chemical IR sensing?. Appl. Spectrosc., 51(4), 495-503.

69. Zhong, Y., Malagari, S. D., Hamilton, T., Wasserman, D. (2015). Review of mid-infrared plasmonic materials. J. Nanophoton. 9(1), 093791.

70. Lee, P. C. Meisel, D. (1982). Adsorption and surface-enhanced Raman of dyes on silver and gold sols. 86(17), 3391-3395.

71. Lyon, L. A., Pena, D. J., Natan, M. J. (1999). Surface plasmon resonance of Au colloid-modifed Au films: partcile size dependence. J. Phys. Chem., 103(28), 5826-5831.

72. Lee, K. S., El-Sayed, M. A. (2006). Gold and silver nanoparticles in sensing and imaging: sensitivity of plasmon response to size, shape, and metal composition. J. Phys. Chem. B., 110(39), 19220-19225.

73. Mustafa, D. E., et al. (2010). Surface plasmon coupling effect of gold nanoparticles with different shape and size on conventional surface plasmon resonance signal. Plasmonics, 5(3), 221-231.

74. Mock, J. J., Barbic, M., Smith, D. R., Schultz, D. A., Schultz, S. (2002a). Shape effects in plasmon resonance of individual colloidal silver nanoparticles. J. Chem. Phys., 116(15), 6755-6759.

75. Matsui, J., et al. (2005). SPR sensor chip for detection of small molecules using molecularly imprinted polymer with embedded gold nanoparticles. Anal. Chem., 77(13), 4282-4285.

76. Driskell, J. D. Lipert, R. J., Porter, M. D. (2006). Labelled gold nanoparticles immobilized at smooth metallic substrates: Systematic investigation of surface plasmon resonance and surface-enhanced Raman scattering. J. Phys. Chem. B., 110(35), 17444-17451.

77. Kumar, A., low, T., Fung, K. H., Avouris, P., Fang, N. X. (2015). Tunable light-matter interaction and the role of hyperbolicity in graphene-hBN system. Nano lett., 15(5), 3172-3180.

78. Hwang, E. H., Sensarma, R., Sarma, S. D. (2010)., Plasmon-phonon coupling in graphene. Phys. Rev. B., 82(1), 195406.

79. Persson, B. N. J., Ryberg, R. (1981). Vibrational interaction between molecules adsorbed on a metal surface: The dipole-dipole interaction. Phys. Rev. B., 24, 6954-

80. Radovic, L. R., Bockrath, B. (2005). On the chemical nature of graphene edge: origin of stability and potential for magnetism in carbon materials. J. Am. Chem. Soc. 127(16), 5917-5927.

81. Peralta-Inga, Z., Murray, J. S., Grice, M. E., Boyd, S., O'Connor, C. J., Politizer, P. (2001). Computational characterization of surfaces of model graphene systems. J. Mol. Struct(THEOCHEM), 549(1), 147-158.

82. Taubner, T., Hillenbrand, R., Keilmann, F. (2004). Nanoscale polymer recognition by spectral signature in scattering infrared near-field microscopy. Appl. Phys. Lett., 85(21), 5064-5066.

83. Losurdo, M., Giangregorio, M. M., Capezzuto, P., Bruno, G. (2011). Graphene CVD growth on copper and nickel: role of hydrogen in kinetics and structure. Phys. Chem. Chem. Phys., 13(46), 20836-20843.

84. Langreth, D. (1985). Energy transfer at surfaces: Asymmetric line shapes and the electron-hole-pair mechanism. Phys. Rev. Lett., 54(2), 126-129.

85. Berashevich, J. Chakraborty, T. (2010). Doping of graphene by adsorption of polar molecules at the oxidized zigzag edges. Phys. Rev. B., 81, 205431.

86. Dimiev, A. M., Alemany, L. B., Tour, J. M. (2013). Graphene oxide. Origin of acidity, its instability in water, and a new dynamic structural model. ACS Nano, 7(1), 576-578

87. Szabo, T., Berkesi, O., Dekany, I. (2005). DRIFT study of deuterium-exchanged graphite oxide. Carbon, 43(15), 3186-3189.

88. Szabo, T., Berkesi, O., Forgo, P. (2006). Evolution of surface functional groups in a series of progressively oxidized graphite oxides. Chem. Mater., 18(11), 2740-2749

89. Seredych, M., Bandosz, T. J. (2010). Combined role of water and surface chemistry in reactive adsorption of ammonia on graphite oxides. Langmuir, 26(8), 5491-5498.

90. Ambrosi, A., Chua, C. K., Bonanni, A. & Pumera, M. (2012). Lithium aluminium hydride as reducing agent for chemically reduced graphene oxides. Chem. Mater., 24(12), 2292-229

91. Beusesm B., Steglich, W. (1978). Simple method for the esterification of carboxylic acids. Angew. Chem. Int. Ed., 17(7), 522-524.

92. Zhang, Z. Yates, J. T. (2012). Band bending in semiconductors: chemical and physical consequences at surfaces and interfaces. Chem. Rev. 112(10), 5520-5551.

93. Rodrigo, D., Limaj, O., Janner, D., Etezadi, D., Abako, F., Pruneri, V., Altug, H. (2015). Mid-infrared plasmonic biosensing with graphene. Appl. Physics., 349(6244)

94. Life Technologies. (2014). BODIPY Dye Series. Retrieved from http://www.lifetechnologies.com/nz/en/home/references/molecular-probes-the-handbook/fluorophores-and-their-amine-reactive-derivatives/bodipy-dye-series.html

95. Rong, Y., Yu, J., Zhang, X., Sun, W., Ye, F., Wu, I., Zhang, Y., Hayden, S., Zhang, Y., Wu, C., Chiu, D. (2014). Yellow fluorescent semiconducting polymer dots with high brightness, small size, and narrow emission for biological applications. ACS Macro letters., 3(10), 1051-1054.

96. Economopoulos, S.P., Tagmatarchis, N. (2015). Multichromophores onto graphene: Supramolecular non-covalent approaches for efficient light harvesting. J. Phys. Chem., 119, 8046-8053.

97. Quhe, R., Ma, J., Zeng, Z., Tang, K., Zheng, J., Wang, Y., … Lu, J. (2013). Tunable band gap in few-layer graphene by surface adsorption. Sci. Rep., 3, 1794-1802.

98. Long, B., Manning, M., Burke, M., Szafranek, B.N., Visimberga, G., Thompson, D., … Quinn, A.J. (2012). Non-covalent functionalization of graphene using self-assembly of alkane-amines. Adv. Func. Mater., 22(4), 717-725.

99. Ramuz, M. P. Vosgueritchian, M., Wei, P. Wang, C., Gao, Y., Wu, Y., Chen, Y. C., Bao, Z. (2012). Evaluation of solution-processable carbon-based electrodes for all-carbon solar cells. ACS Nano, 6(11), 10384-10395.

100. Jablan, M., Solijacic, M., Bulijan, H. Unconventional plasmon-phonon coupling in graphene. (2011) Phys. Rev. B., 83(1), 161409(R).

101. Jablan, M., Buligan, H., Solijacic, M. (2009). Plasmonics in graphene at infrared frequencies., Phys. Rev. B., 245435.

102. Boens, N., Verbelen, B., Dehaen, W. (2015). Post functionalization of the BODIPY core: Synthesis and spectroscopy. Eur. J. Org. Chem., 30(1), 6577-6595.

103. Cerda, E., Mahadevan, L., Pasini, J. M. (2003). The elements of draping. Proc. Natl. Acad. Sci. 101, 1806-1810.

104. Pereira, V. M., Castro Neto, A. H., Liang, H. Y., Mahadevan, L. (2010). Geometry, mechanics and electronics of singular structures and wrinkles in graphene. Phys. Rev. Lett., 105, 156603.

105. Boehm, H. P., Hofmann, U. (1962). Surface properties of extremely thin graphite lamellae. Proc. 5th Conf. on Carbon (Oxford: Pergamon)., p 73.

106. Clar, E. (1972). The aromatic Sextet. John Wiley & Sons., London.

107. Yu, P., Lowe, S. E., Simon, G. P., Zhong, Y. L. (2015). Electrochemical exfoliation of graphite and production of functional graphene. Curr. Opin. Colloiud Interface Sci., 20(5), 329-338.

108. Kravets, V. G., Grigotenko, A. N., Nair, R. R., Blake, P., Anissimove, S., Novoselov, K. S., Geim, A. K. (2010). Phys. Rev. B., 81, 155413.

109. Van Hove, L. The occurrence of singularities in the elastic frequency distribution of a crystal. (1953). Phys. Rev. 89., 1189-1193.

110. P. B. Johnson and R. W. Christy. Optical constants of the Noble metals. Phys. Rev. B, 1972, 6, 4370-4379.

111. Osawa, M. Ataka, K., Yoshii, K., Nishikawa, Y. (1993). Surface-Enhanced infrared spectroscopy: The origin of the absorption enhancement and band selection rule in the infrared spectra of molecules adsorbed on fine metal particles. Appl. Spectrosc. 47, 1497-1502.

112. Jain, P. K., Eustis, S., El-Sayed, M. A. (2006). Plasmon coupling in nanorod assemblies: optical absorption, discrete dipole approximation simulation, and exaction-coupling model. J. Phys. Chem. B., 110(37), 18243-18253.

113. Lovera, A., Gallinet, B., Nordlander, P., Martin, O. F. (2013). Mechanisms of Fano resonances in coupled plasmonic systems. ACS Nano., 7(5), 4527-4536.

114. Chae, D.H., Utikal, T., Weisenburger, S., Giessen, H., Klitzing, K. V., Lippitz, M., Smet, J. (2011). Excitonic Fano resonance in free-standing graphene. Nano Lett, 11(3), 1379-1382.

115. Kelley, A. M. A molecular spectroscopic description of optical spectra of J-aggregated dyes on gold nanoparticles. Nano Lett, 7(10), 3235-3240.

116. Su, K. H., Wei, Q. H., Zhang, X. (2003). Interparticle coupling effects on plasmon resonances of nanogold particles. Nano letters., 3(8), 1087-1090.

117. Dahmen, C., Schmidt, B., Plessen, G. V. (2007). Radiation damping in Metal nanoparticle pairs. Nano letters., 7(2), 318-322.

118. Kottmann, J. P., Martin, O. J. F. (2001). Retardation-induced plasmon resonances in coupled nanoparticles. Optics letters., 26(14), 1096-1098.

119. Schatz, G. C., Hao, E. (2004). Electromagnetic fields around silver nanoparticles and dimers., The journal of chemical physics, 120(1), 357-366.

120. Muskens, O. L., Giannini, V., Sanchez-Gil, J. A., Rivas, J. G. (2007). Optical scattering resonances of single and coupled dimer plasmonic nanoantennas. Optics express., 15(26), 17736-17746.

121. Gunnarsson, L., Rindzevicius, T., Prikulis, J., Kasemo, B., Kall, M. (2005). Confined plasmons in nanofabricated single silver particle pairs: Experimental observations of strong interparticle interactions. J. Phys. Chem. B., 109(3), 1079-1087.
122. Zhang, W., Yu, T., Liao, L., Cao, Z. (2013). Ring formation from a dry sessile colloidal droplet. AIP advances 3, 102109
123. Weon, B. M., Je, J. H. (2013). Self-pinning by colloids confined at a contact line. Phys. Rev. Lett., 110, 028303.
124. Wullets, K. A., Van Duyne, R. P. (2007). Localized surface plasmon resonance spectroscopy and sensing. Annu. Rev. Phys. Chem, 58, 267-297.
125. Ru, E. C. L., Etchegoin, P. B. (2009). Principles of surface-enhanced raman spectroscopy and related plasmonic effects. Wellington, New Zealand: Elsevier.
126. Pavlik, I., Klikorka, J. (1965). Infrared spectrum of the ferricinium cation. Collect. Czech. Chem. Commun., 30, 664-674.
127. Popenoe, D. D., Deinhammer, R. S., Porter, M. D. (1992). Infrared spectroelectrochemical characterization of ferrocene-terminated alkanethiolate monolayers at gold. Langmuir, 8, 2521-2530.